Study of Vector-Meson Photoproduction decaying to Multitrack-Final States using CLAS-g12 Data

Zulkaida Akbar, Andrew Hurley, Kyle Romines, Christopher Zeoli, Volker Crede
Florida State University

October 24, 2017

Abstract

The study of baryon resonances provides a deeper understanding of the strong interaction because the dynamics and relevant degrees of freedom hidden within them are reflected by the properties of the excited states of baryons. Higher-lying excited states at and above 1.7 GeV/c^2 are generally predicted to have strong couplings to final states involving a heavier meson, e. g. one of the vector mesons, ρ, ω, ϕ, as compared to a lighter pseudoscalar meson, e. g. π and η. Decays to the $\pi\pi N$ final states via $\pi\Delta$ also become more important through the population of intermediate resonances. We observe that nature invests in mass rather than momentum. The excited states of the nucleon are usually found as broadly overlapping resonances which may decay into a multitude of final states involving mesons and baryons. Polarization observables make it possible to isolate single-resonance contributions from other interference terms. The CLAS-g12 experiment, as part of the N^* spectroscopy program at Jefferson Laboratory, accumulated photoproduction data using circularly-polarized tagged photons incident on an unpolarized liquid hydrogen target in the photon energy range 1.1 to 5.4 GeV. This document summarizes the FSU analyses of reactions and observables which involve two charged pions (and kaons), either in the fully exclusive reaction $\gamma p \to p\,\pi^+\pi^-$ ($\gamma p \to p\,\phi \to p\,K^+K^-$) or in the semi-exclusive reaction with a missing neutral pion, $\gamma p \to p\,\omega$ ($p\eta$) $\to p\,\pi^+\pi^-$ (π^0) and $\gamma p \to K^0\,\Sigma^+ \to p\,\pi^+\pi^-$ (π^0).

The group at FSU has extracted the beam-helicity asymmetry, $I^{\odot}$, for the two-π reaction $\gamma p \to p\pi^+\pi^-$ and has studied the cross sections for the reactions $\gamma p \to p\,\omega$ ($p\,\eta,\ K^0\,\Sigma^+$) $\to p\,\pi^+\pi^-$ (π^0) as well as $\gamma p \to p\,\phi \to p\,K^+K^-$ and determined the spin-density matrix elements for the ω, ϕ [1]. These g12-analyses complement our comprehensive FSU program on vector-meson photoproduction which also includes results from CLAS-g8b and CLAS-g9 (FROST). The ω and the ϕ meson are observed and studied directly from the data and the information on the (broad) ρ can be extracted from the double-pion reaction in a partial-wave analysis. We also observed a small $\phi \to \pi^+\pi^-$ (π^0) contribution in our g12 data but did not further investigate this decay.

With the high statistics CLAS-g12 data sample and a measured differential cross section procured, a Dalitz Plot (DP) analysis of the $\omega \to 3\pi$ decay dynamics in close cooperation with the Joint Physics Analysis Center (JPAC) at JLab has been conducted. In addition to fitting Dalitz Plot Expansion parameters (e.g. α, β, γ, and δ), a first-time, real data fit to an Isobar and Unitarity based decay model, JPAC decay amplitude, has been made. As a consequence of unitarity, this amplitude also accounts for both elastic (i.e. π-π) and inelastic (e.g. K-$\bar{K}$) rescattering effects. The novel separation and parameterization of these latter contributions are unique features of this model which set it apart from alike models.

[1] At this point, the work on $\gamma p \to p\,\phi$ is still ongoing and will be added to this note later.

Contents

1 Introduction

Effective theories and models have been developed to better understand the properties of baryon resonances. Various constituent quark models (CQMs) are currently the best approach to make predictions for the properties of the baryon ground states and excited states. However, the predictions for the hadron spectrum made by these models do not match accurately the states measured by experiment, especially at high energies. These models for example predict many more resonances than have been observed, leading to the so-called "missing resonance" problem. The latest results in baryon spectroscopy suggest that three-body final states are very important in order to establish higher-mass resonances. Moreover, the photoproduction of vector mesons, such as ω, ρ, and ϕ has remained underexplored in recent years but will also give us very useful insight into high-mass resonances. It has been generally accepted that a nucleon resonance needs to be observed in many different decay modes to be considered convincingly established. The two-pion final states are the dominant contributors to the total photo-absorption cross section above $W \approx 1.9$ GeV ($E_\gamma \approx 1.46$ GeV). In this analysis, we extracted the beam-helicity asymmetry, $I^{\odot}$, for the reaction $\gamma p \to p\,\pi^+\pi^-$, the cross sections for the reactions $\gamma p \to p\,\omega\;\; (p\,\eta,\, K^0\,\Sigma^+) \to p\,\pi^+\pi^-\,(\pi^0)$, $\gamma p \to p\,\phi \to p\,K^+K^-$, and the spin-density matrix elements for the ω and ϕ[2] mesons.

From an experimental and an analysis point-of-view, the reaction $\gamma p \to p\,\pi^+\pi^-$ as well as $\gamma p \to p\,\pi^+\pi^-\,(\pi^0)$ have the same charged particles in the final state and therefore, it was straight forward to unify the analysis of these two hadronic final states in terms of extracting the observables. The subsequent interpretation of the results will certainly proceed in different ways.

2 The g12 Experiment at Jefferson Lab

The experimental Hall B at Jefferson Lab provided a unique set of experimental devices for the g12 experiment. The CEBAF Large Acceptance Spectrometer (CLAS) [1], which was housed in Hall B, was a nearly-4π spectrometer optimized for hadron spectroscopy. The bremsstrahlung tagging technique, which was used by the broad-range photon tagging facility [2] at Hall B, could tag photon energies over a range from 20 % to 95 % of the incident electron energy and was capable of operating with CEBAF beam energies up to 5.5 GeV. The g12 experiment utilized a circularly-polarized photon beam in combination with an unpolarized liquid hydrogen target. The energy range covered in the experiment was about 1.1 to 5.4 GeV.

The CLAS-g12 group is the first run grup which went through a formal run group review. The document *The g12 Analysis Procedures, Statistics, and Systematics* was produced. The goal of the review and the document was to identify, review and approve common analysis procedures relevant to most of the g12 analyses. This will allow the collaboration to streamline subsequent reviews of individual g12 physics analyses. The following procedures are common for most analyses and have been approved by the g12 procedure review committee in the g12 analysis procedures manuscript:

- Calibration and *cooking* of the data sets.
- Momentum and beam-energy corrections as described in the general g12 analysis note.
- Fiducial cuts (as described in Section 5.3 of the analysis note): Three different scenarios were studied and cuts derived in terms of *nominal, tight, loose.* We chose *nominal* for our analyses.

[2] At this point, the work on $\gamma p \to p\,\phi$ is still ongoing and will be added to this note later.

Other common g12 procedures include:

- Inclusive *good run list* as described in Table 7 of the g12 note.
- Target density and its uncertainty.
- Photon flux calculation and its uncertainty.
- Degree of circular beam polarization and its uncertainty.
- Monte Carlo GPP and GSIM parameters.
- Drift chamber efficiency map.
- Knockout list of EC and TOF paddles.
- Lepton identification (ID) approved as "di-lepton ID."

The following analysis procedures however are subject to individual reviews and are thus discussed in this document:

- Particle ID and event selection.
- Kinematic fitting.
- Trigger simulation (and efficiency studies).
- Accounting for multiple (accidental) photons.

This analysis note is organized as follows. In Section 3, we discuss the experimental conditions of the g12 data set, the identification of the photon and final-state particles, kinematic fitting, and additional cuts, which were used to tune the data set. Moreover, some details on the beam polarization relevant for the $I^{\odot}$ analysis are introduced. Section 4 describes the extraction of the observables for the reactions $\gamma p \to p\pi^+\pi^-$, $\gamma p \to p\,\omega$, $\gamma p \to p\,\eta$, $\gamma p \to K^0\,\Sigma^+$, and $\gamma p \to p\,\phi$. The results and conclusions of the analyses are discussed in Section 6.

3 Event Selection

3.1 The CLAS-g12 Data Set

This section summarizes the experimental conditions of the g12 data set. The data for this experiment were taken between April 1st and June 9th, 2008. The data set was further divided into ten different groups of runs according to different trigger configurations.

Table 1 shows the different g12 trigger configurations. We used only Period 2 and some runs from Period 1 (starting from run 56520) for our analyses at FSU. For these events, the trigger required either (at least) three charged tracks with no restriction on the photon energy or (at least) two tracks if the energy was above 3.6 GeV. Since our primary motivation was to extract the ω (and $\pi^+\pi^-$) cross sections with high quality, we decided not to mix trigger configurations and thus, avoided the prescaled data and those using an Electromagnetic Calorimeter (EC)-based photon or lepton trigger (Period 3 - 8). Period 1 suffered from lower statistics and using it would not have

Period	Runs	Trigger Configuration
1	56572 and earlier	not prescaled, trigger change at 4.4 GeV
2	56573 - 56594, 56608 - 56646	not prescaled, trigger change at 3.6 GeV
3	56601 - 56604, 56648 - 56660	prescaled
4	56665 - 56667	prescaled
5	56605, 56607, 56647	prescaled
6	56668 - 56670	prescaled
7	56897 and later	prescaled
8	57094 and later	prescaled
9	56585, 56619, 56637	single-sector, not prescaled
10	56663 and later	single-sector, not prescaled

Table 1: *The different trigger configurations used in g12 (from the g12 wiki []).*

significantly improved the statistical uncertainty of our results. Moreover, this period switched from a three-track requirement to a two-track requirement at a different energy.

The information included in the raw data consisted of QDC (Charge to Digital Convertor) and TDC (Time to Digital Converter) channel IDs and values. In a first step, the data had to undergo reconstruction, or be *cooked.* This process converted the data into physical quantities like particle IDs, positions, angles, energies, and momenta. The data calibration was carried out independently for each detector component of CLAS. After the detectors had been calibrated and the particle tracks had been reconstructed, the data were made available for physics analysis. Each event has its information organized in CLAS data banks CLAS data banks[3]. These data banks contain not only the properties of the particles involved in a reaction but also information about detector hits. Here we list the most relevant data banks that we used in our g12 analyses:

1. **PART** – This bank contains most of the details about the detected particles, such as the particle IDs, 4-vectors, vertex of each particle, and other information from various detectors.

2. **TAGR** – In this bank, information about all incident photons is stored. It comprises the energy of the photon(s), the time of the photon(s) after it was reconstructed in the Tagger, the time of the photon(s) after the RF correction, status of the photon(s) (used to identify which ones were not reconstructed properly), and the E- and T-counter ID information of the corresponding scattered electron.

3. **TBER** – Time-based tracking error bank containing fit parameters and the covariance matrix.

4. **TBID** – This bank contains information on time-based particle ID (including β ($= \frac{v}{c}$) values).

5. **TGBI** – Trigger bank; it also stores polarization information, e.g. helicity bit.

[3]http://clasweb.jlab.org/bos/browsebos.php?bank=gpid&build=64bit/STABL

3.2 Reaction Channel and General Event Selection

The final states of interest in this analysis are $\gamma p \to p\,\pi^+\pi^-$ and $\gamma p \to p\,\pi^+\pi^-\,(\pi^0)$. These three-track channels were broken up into different topologies as shown in Table 2. A topology is defined according to the detected particles in the final state: the two-particle final states (Topologies 1 - 3) and the three-particle final states (Topologies 4 - 6). A particle which was not detected in a given topology could be identified through the missing-mass technique. For this method, the Lorentz vectors of the incoming beam and the target were used. The four-momentum of a missing particle in the reaction was then determined from the measured three-momenta and the particle energies. The missing four-momentum was given by:

$$x^\mu \,=\, k^\mu \,+\, P^\mu \,-\, \sum_{i=1}^{2,3} p_i^\mu\,, \tag{1}$$

where k^μ and P^μ are the initial photon and target-proton four-momenta and p_i^μ are the four-momenta of the two or three detected final-state particles. The missing mass m_X was defined as:

$$m_X^2 \,=\, x^\mu x_\mu\,. \tag{2}$$

The missing-mass distribution was used for a data quality check after all corrections and cuts had been applied. The four-momentum vector x^μ in Equation 1 was used to complete the set of four-vectors for Topology 5 (Table 2). The other final states with a missing particle could not be analyzed owing to the trigger configuration in Period 2 which required three tracks.

Events were pre-selected based on the particles' identification number (PID), which was determined during the cooking process. Events that did not meet this requirement (Table 2) were ignored and subsequently omitted from the analysis. The calculation of the detected particles' masses, which was necessary to determine the PIDs of, used two independently-measured quantities, the momentum (p) and the velocity as a fraction of the speed of light (β). The magnitude of

Reaction	Topology	Reconstructed Particles				Missing Particle of Interest
		Total	p	$\pi^+\,(K^+)$	$\pi^-\,(K^-)$	
$\gamma p \to p\,\pi^+\,(\pi^-)$	1	2	1	1	0	m_{π^-}
$\gamma p \to p\,\pi^-\,(\pi^+)$	2	2	1	0	1	m_{π^+}
$\gamma p \to (p)\,\pi^+\pi^-$	3	2	0	1	1	m_p
$\gamma p \to p\,\pi^+\pi^-$	4	3	1	1	1	0
$\gamma p \to p\,\pi^+\pi^-\,(\pi^0)$	5	3	1	1	1	m_{π^0}
$\gamma p \to p\,K^+K^-$	6	3	1	0 (1)	0 (1)	0

Table 2: *Classification of the reactions, $\gamma p \to p\,\pi^+\pi^-$, $\gamma p \to p\,K^+K^-$, and $\gamma p \to p\,\pi^+\pi^-\,(\pi^0)$, using different topologies. Reconstructed particles were identified by their PID information from the TBID bank. Note that we did not analyze Topology 1 - 3 owing to the trigger configuration in Period 2 which required three tracks.*

a particle's momentum was determined with an error of $< 1\,\%$ using information from the CLAS drift chambers (DC) [1]. The quantity β of a detected final-state particle was determined with an error of up to $5\,\%$ [1] using a combination of the Start Counter (SC), the Time of Flight (TOF) spectrometer, and the particle's trajectory through CLAS. The detected particle's mass can then be calculated by:

$$m^2_{\text{particle } X} \,=\, \frac{p^2\,(1\,-\,\beta^2)}{\beta^2}\,. \tag{3}$$

After the particle's mass had been calculated, it was compared to the masses of known particles (hadrons and leptons). If this calculated mass matched that of a known particle (within resolution), the PID associated with that mass was assigned to the final-state particle. This value could then be used to select certain final-states for analysis. In this analysis, the physical properties of the final-state particles (e.g. their 4-vectors, vertex information, etc.) were extracted from the PART data banks. Photon and final-state particle selection was further improved by applying cuts and corrections (see Section 3.3). We also used kinematic fitting (see Section 3.5) to fine-tune the initial- and final-state momenta by imposing energy- and momentum conservation. Finally, to separate signal events from the remaining background, we used an event-based Q-factor method which is discussed in more details in Section 3.12.

In a short summary, listed below are the cuts and (in the right order) corrections that were applied to the g12 data in these FSU analyses.

General g12 Corrections

- Tagger-sag corrections (done in the cooking process).
- ELoss corrections using the standard CLAS package [3].
- Beam-energy corrections based on the CLAS-approved run-group approach [4].
- Momentum corrections based on the CLAS-approved run-group approach [4].

Florida State U. Cuts

- Vertex cuts: $-110.0 \,<\, z \,<\, -70.0$ cm and $x^2 \,+\, y^2 \,<\, 4$ cm (removed).
- Photon selection & accidentals (PART[]. NGRF = 1 & PART[].TAGRID equal for all tracks)
- Particle selection: $\Delta\beta \,=\, |\beta_{\text{c}} \,-\, \beta_{\text{m}}| \,\leq\, 3\sigma$ (removed)
- Confidence-level cut of CL > 0.001 for $\gamma p \to p\,\omega \to p\,\pi^+\pi^-\,(\pi^0)$
- Fiducial cuts: *nominal* scenario [4].

The order of these applied cuts and corrections was quite flexible with the exception of a few cases. Momentum corrections were applied after the energy-loss corrections. The following sections describe the applied cuts and corrections in more detail.

3.3 Photon and Particle Identification

3.3.1 Initial-Photon Selection (Cuts on Timing and Accidental Photons)

The electrons, which were used to produce the beam of polarized photons via bremsstrahlung radiation, were delivered from the accelerator into Hall B in the form of 2 ns bunches. Since each bunch contained many electrons, there were several potential photon candidates per recorded event that could have triggered the reaction inside the target. Random electron hits could also occur from various background sources (e.g. cosmic rays). These did not create bremsstrahlung photons but the hits were registered in the tagger scintillators. It was important to determine the correct photon in each event (out of about five candidates on average) because the corresponding photon energy was key to understanding the initial state of the event. The analysis steps taken in the photon selection were as follows:

1. The Start Counter time per track at the interaction point, t_{track}, was given by:

$$t_{\text{track}} = t_{\text{ST}} - \frac{d}{c\,\beta_{\text{calc}}}\,, \tag{4}$$

   where t_{ST} was the time when the particle was detected by the Start Counter, d was the length of the track from the interaction point to the Start Counter [4], and $c\,\beta_{\text{calc}}$ was the calculated velocity of the particle. These (track) times can be averaged to give an event time, t_{event}.

   The time at which a candidate photon arrived at the interaction point, t_γ, was given by:

$$t_\gamma = t_{\text{center}} + \frac{d'}{c}\,, \tag{5}$$

   where t_{center} was the time at which the photon arrived at the center of the target and d' was the distance between the center of the target and the event vertex along the beam-axis. We did not consider the x- and y-coordinates of the event vertex because they were comparable to the vertex resolution. In this analysis, the t_γ values were obtained from TAGR[].TPHO.

   Both, t_γ as well as t_{event}, describe the time of the γp interaction – based on initial- and final-state particles, respectively. To find the correct initial photon, we can look at the corresponding time differences. The *coincidence time*, Δt_{TGPB}, was thus defined per photon as the difference between the Tagger time and the Start Counter time at the interaction point, $t_{\text{event}} - t_\gamma$. Since each event had several candidate photons, several Δt_{TGPB} values were available, which could be obtained from the TGPB bank. Figure 1 (left) shows an example distribution of the coincidence time, Δt_{TGPB}. The figure clearly shows the 2 ns bunching of the photons that arrived at the target. For each event, the candidate photon that had the smallest coincidence time was determined and its energy and timing information, t_γ, were written to the event's TAGR bank. The total number of photon candidates per event was also available. *The* photon selection itself was performed by the CLAS offline software in the cooking process. However, we applied a timing cut of $\Delta t_{\text{TGPB}} < 1$ ns in this analysis.

2. Occasionally, events could have more than one candidate photon with $|\Delta t_{\text{TGPB}}| < 1$ ns. In such cases, the photon selection could not be made based on their time information. The

[4] The values of t_{ST} and d could be obtained from the GPID[].ST_TIME and GPID[].ST_LEN, respectively.

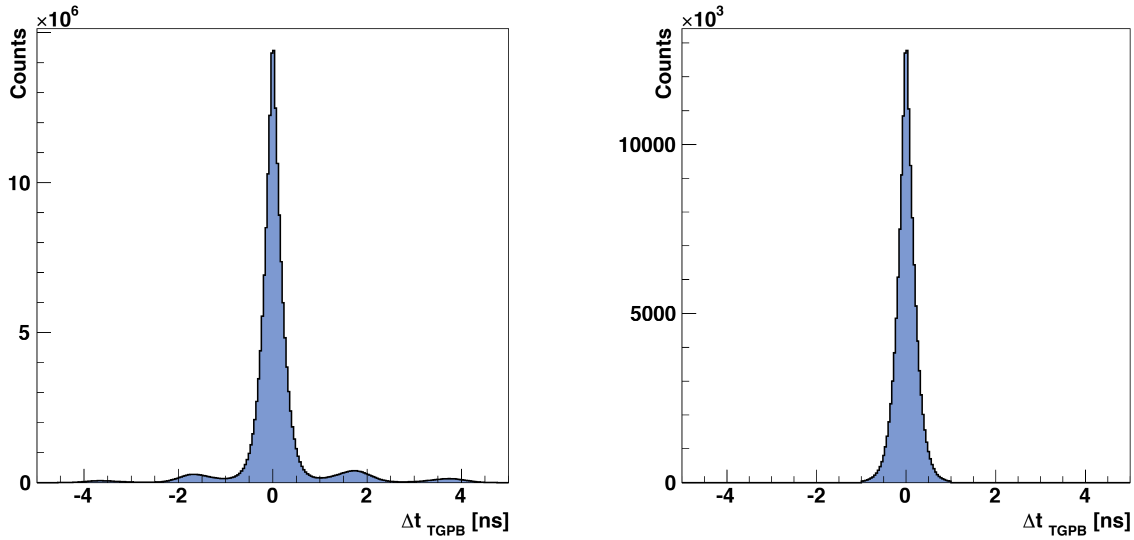

Figure 1: *Left: Example of a coincidence-time distribution, Δt_{TGPB}, for the inclusive $p\,\pi^+\pi^-$ final-state topology. The 2 ns bunching of the photon beam is clearly visible in the histogram. Right: Distribution of $\Delta t_{\mathrm{TGPB}} = t_{\mathrm{event}} - t_\gamma$ for the selected photon (one entry per event) after PID cuts. The event vertex time, t_{event}, was based on Equation 4. We only considered events which had exactly one candidate photon in the same RF bucket per track; each identified track had to be associated with the same photon.*

fraction of these events was about 13 % in the g12 experiment. To prevent any ambiguity, only events with exactly one photon candidate in the same RF bucket for all selected tracks (TAGR[].NGRF = 1) were considered in this analysis. In addition, we also ensured that the selected photon was the same for all reconstructed tracks (TAGR[].TAGRID equal for all tracks). Figure 1 (right) shows an example of the coincidence-time distribution for the selected initial photon (one entry per event) after PID cuts.

3.3.2 Proton and Pion Selection

The photon energy for each event was selected according to the procedure outlined in Section 3.3.1. In the next step, the identification of the final-state particles, proton, π^+, and π^-, was needed. As mentioned in Section 3.2, we initially used particle ID information from the PART bank and selected those events which belonged to the topologies of our interest (Table 2). For a more refined selection of the particles, we used the information on the measured and calculated β values of each particle. The TBID bank contained the CLAS-measured momentum of a particle; a theoretical value, β_{c}, for that particle could then be calculated from this measured momentum and an assumed mass. The β_c values for all possible particle types were compared to the CLAS-measured empirical $\beta_{\mathrm{m}} = \frac{v}{c}$ value. Particle identification then proceeded by choosing the calculated β_{c} closest to the measured β_{m}. Figure 2 shows the differences, $\Delta\beta = \beta_{\mathrm{c}} - \beta_{\mathrm{m}}$ for the different final-state particles based on the full g12 statistics that we used in our FSU analyses, Period 1 & 2 (see Table 1).

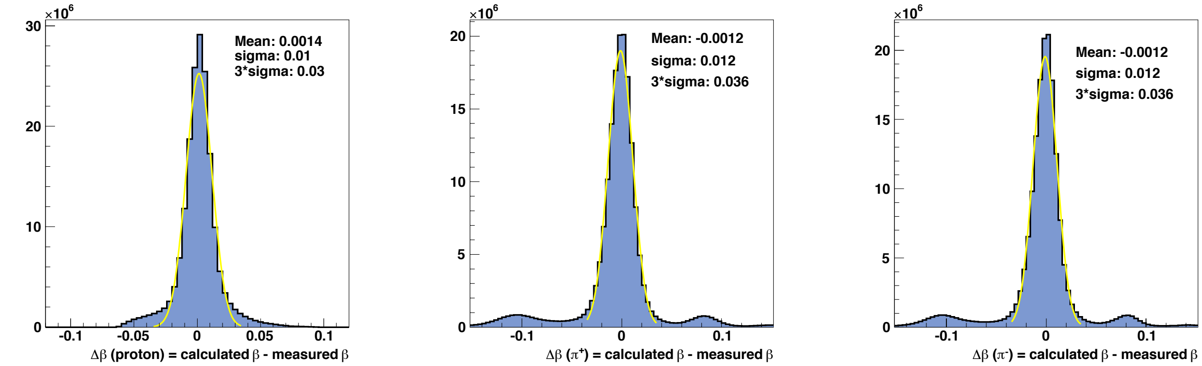

Figure 2: *Distributions of $\Delta\beta = \beta_c - \beta_m$ for protons (left) as well as for the π^+ (middle) and for the π^- (right) from the g12 experiment (full statistics used in our FSU analyses, Period 1 & 2 (see Table 1)). The quantity β_c was calculated based on the particle's PDG mass [5]. Events in the center peak were selected after applying a $|\beta_c - \beta_m| \leq 3\sigma$ cut. See text for more details.*

Assuming a mass m for the particle (taken from PDG [5]), $\Delta\beta$ was given by:

$$\Delta\beta = \beta_c - \beta_m = \sqrt{\frac{p^2}{m^2 + p^2}} - \beta_m \,. \tag{6}$$

The prominent peaks around $\Delta\beta = 0$ shown in Figure 2 correspond to the particles of interest. It can be seen in the figures that the $\Delta\beta$ distributions for the pions are slightly broader than for the protons and long tails including a prominent enhancement on either side of the central peak are visible. When the PART bank was created during the track reconstruction, electrons were not separated from pions. The additional features in the $\Delta\beta$ distributions for the pions represent these electrons which need to be filtered out. To identify the protons and pions, loose cuts on $|\beta_c - \beta_m|$ were applied. The cut values were determined by fitting the main peak around $\Delta\beta = 0$ with a Gaussian and discarding all events outside a 3σ window, where σ was the Gaussian width. Thus, any event with a value of $|\Delta\beta|$ greater than 0.03 for the proton and 0.036 for the pions was filtered out of the g12 data sets. Figure 3 shows the measured momentum, p, versus the measured β_m for protons and pions before (left) and after (right) applying the $|\beta_c - \beta_m| < 3\sigma$ cut. The bands for the pions and protons (lower band) are clearly visible.

3.4 Vertex Cut

In the g12 experiment, the liquid hydrogen target was not located at the center of CLAS but moved 90 cm upstream to increase the angular resolution for heavier-meson photoproduction in the forward direction. The target itself was 40 cm long and 2 cm in diameter. For this reason, the z-vertex cut we applied was $-110 < z < -70$ cm; the full z-vertex distribution is shown in Figure 4. The vertex cut in the x-y plane was chosen such that selected events originated no more than 2 cm from the z axis (beam line).

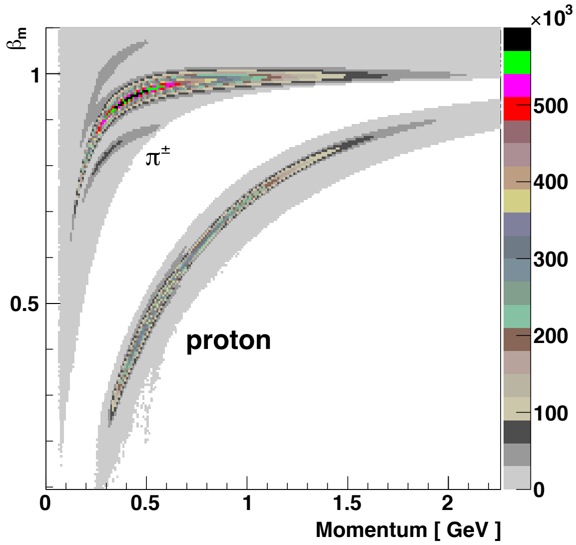

Figure 3: *Left: The measured β_{m} versus the measured momentum taken from PART on a logarithmic color scale. Note a thin horizontal line at one for electrons, and the broad stripes for pions (top) followed by protons (bottom). Right: The measured β_{m} versus the measured momentum after applying the 3σ cut based on the difference $\Delta\beta = \beta_{\mathrm{c}} - \beta_{\mathrm{m}}$. Clean pion and proton bands are visible. These figures were made using the full statistics used in our FSU analyses, Period 1 & 2 (see Table 1)*

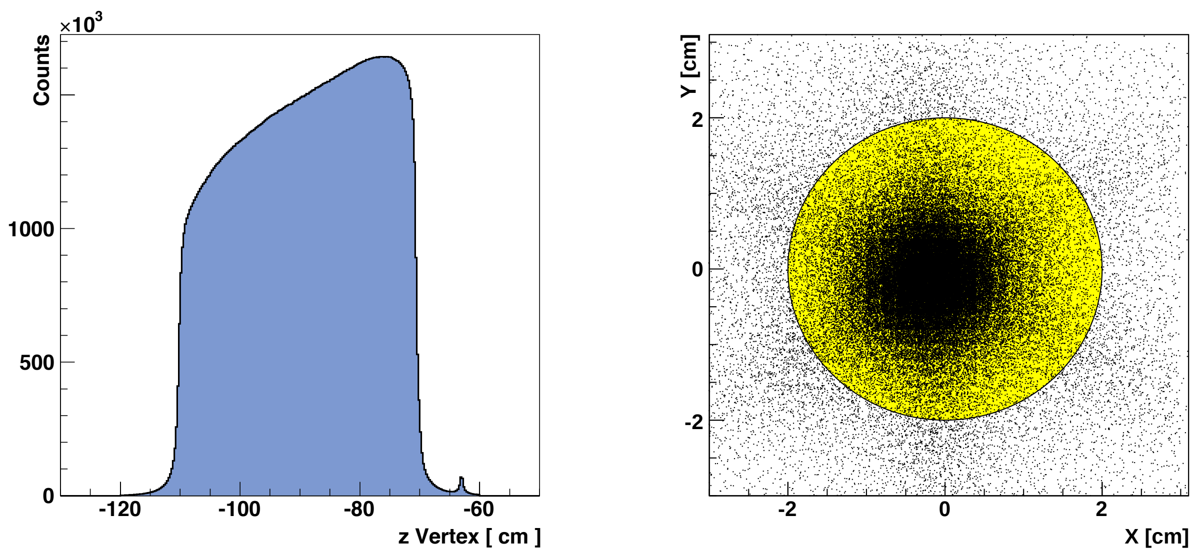

Figure 4: *Left: The z-vertex distribution (axis along the beam line) of all reconstructed particles we used in our FSU analyses. The shape of the liquid hydrogen target is clearly visible. The small enhancement at about $z = -63$ cm originates from the exit window of the vaccuum chamber. Right: The x- vs. y-vertex distribution from g12 based on our full statistics (Period 1 & 2). The circle indicates our cut of $x^2 + y^2 < 2$ cm^2.*

3.5 Introduction to Kinematic Fitting

The 4-vectors of the final-state particles were determined in the *cooking* or reconstruction phase. Kinematic fitting [6] slightly modified these *raw* 4-vectors by imposing energy-momentum conservation on the event as a physical constraint. In a brief summary, all measured components of the Lorentz 4-vectors (the magnitude of the momentum as well as the two angles used in the drift-chamber reconstruction – p, λ, ϕ, respectively) in addition to the initial photon energy were modified within their given errors until the event satisfied energy-momentum conservation exactly. The determination of the correct error (or covariance) matrix was important in this fitting procedure. The kinematically-fitted event had then several quantities which could be used to inspect the quality of the kinematic fitting: a pull value for each measured quantity and an overall χ^2 value. The latter could be converted to a confidence-level (CL) value to judge the goodness-of-fit. The pull distributions were used to evaluate the initial error estimation and to study systematics. It turned out that kinematic fitting provided an effective tool to verify kinematic corrections, e. g. momentum corrections.

3.5.1 Confidence Level

To check the *goodness-of-fit* or the agreement between the fit hypothesis and the data, the fit χ^2 value was used. The corresponding CL value was defined as:

$$CL = \int_{\chi^2}^{\infty} f(z;n)\, dz\,, \tag{7}$$

where $f(z;n)$ was the χ^2 probability density function with n degrees of freedom. It denoted the probability distribution for certain external constraints, e. g. energy-momentum conservation or also a missing-particle constraint. In the ideal case where all events satisfied the fit hypothesis and the measured quantities were all independent and had only statistical uncertainties, the confidence-level distribution would be flat from $(0, 1]$. However, the real data had a confidence-level distribution which showed a peak near zero (Fig. 5, left side). This peak contained events which did not satisfy the imposed constraints. These events could be hadronic background events, poorly-reconstructed events with significant systematic uncertainties, or events with misidentified particles. A cut on small CL values eliminated the majority of these background events while only a relatively small amount of good data was lost.

3.5.2 Pulls

A *pull value* is a measure of how much and in what direction the kinematic fitter has to alter a measured parameter – or to *pull* at it – in order to make the event fulfill the imposed constraint. All three fit parameters for every detected final-state particle had pull distributions. The pull value for the i^{th} fit parameter was given by:

$$z_i = \frac{\epsilon_i}{\sigma(\epsilon_i)}\,, \tag{8}$$

where $\epsilon_i = \eta_i - y_i$ was the difference between the fitted value, η_i, and the measured value, y_i. The quantity σ represents the standard deviation of the parameter ϵ_i. Therefore, the i^{th} pull can be written as:

$$z_i = \frac{\eta_i - y_i}{\sqrt{\sigma^2(\eta_i) - \sigma^2(y_i)}}\,. \tag{9}$$

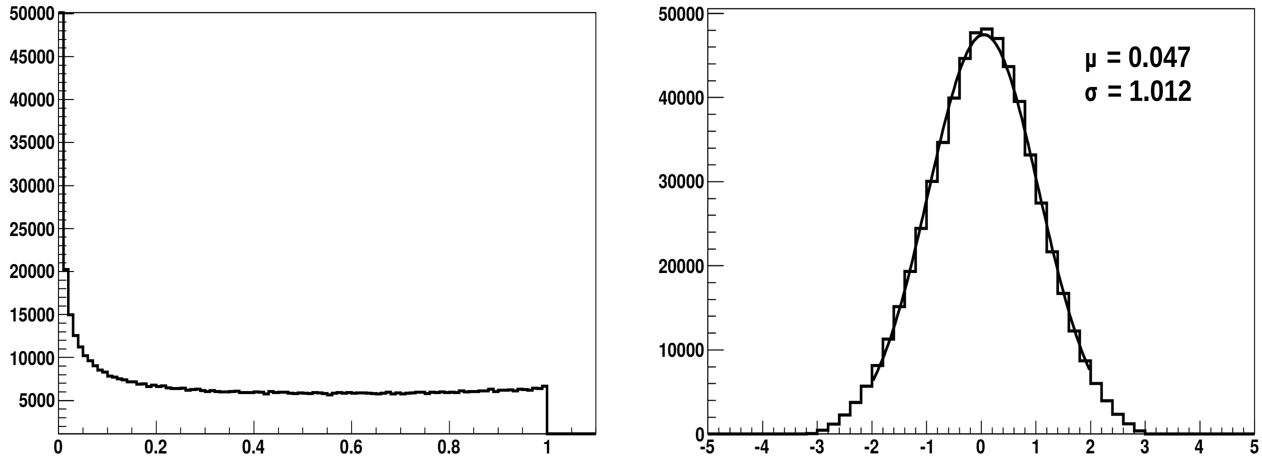

Figure 5: *Example of results from kinematic fitting. Energy and momentum conservation was imposed on Topology 4 in* $\gamma p \to p\,\pi^+\pi^-$. *Left: A confidence-level distribution. It peaks toward zero but flattens out toward one. Right: Pull distribution of the incoming photon energy. Ideally, such a distribution is Gaussian in shape, centered at the origin (*$\mu = 0$*) with a sigma of one (*$\sigma = 1$*).*

The reaction $\gamma p \to p\,\pi^+\pi^-$ (using Topology 4, see Table 2) had three detected final-state particles: proton, π^+, and π^-. Since the reconstruction of each particle was based on three parameters, this topology had ten pull distributions including a pull for the initial photon energy. In the ideal case that the error matrix of these parameters was correctly determined and all remaining systematic errors were negligible, the pull distributions would be Gaussian in shape with a width of one ($\sigma = 1$) and centered at zero ($\mu = 0$); such an example is shown in Figure 5 (right side). A systematic problem with the data in the quantity η_i would be observed as an overall shift away from zero. Similarly, if the errors of η_i were consistently (overestimated) underestimated, then the corresponding pull distribution would be too (narrow) broad, and the slope of the CL distribution toward $CL = 1$ would be (positive) negative. The errors of the measured parameters can be corrected from the pull distributions in an iterative procedure.

In our analysis, kinematic fitting served as an effective tool to double-check the final-state corrections approved in Ref. [4]. We used Topology 4 (all final-state particles detected) for this. The final mean and σ values of Gaussian fits to our g12 pull distributions (after all corrections) are shown in Table 3.

3.6 Kinematic Corrections

The following subsections briefly summarize some of the standard CLAS corrections. We only give a brief description here (in the order of application) without showing the actual effect on the data. The latter was discussed in Ref. [4] and has been approved by the collaboration.

3.6.1 Tagger-Sag Correction

The energy of the incoming photons was determined by the Hall-B tagging system. It was observed in previous experiments that a physical sagging of the holding structure supporting the E-counter scintillator bars could be attributed to gravitational forces [7]. The consequence of this time-

	proton			π^+			π^-			γ
	mom.	λ	ϕ	mom.	λ	ϕ	mom.	λ	ϕ	E

CLAS-g12: $\gamma p \to p\pi^+\pi^-$

$\bar{x}$	0.090	−0.044	−0.001	0.060	−0.001	−0.016	−0.014	−0.016	−0.048	−0.062
σ	1.159	0.970	1.136	1.048	1.009	1.089	1.057	1.013	1.118	1.136

CLAS-g12: $\gamma p \to p\pi^+\pi^-\ (\pi^0)$

$\bar{x}$	0.140	0.001	−0.211	−0.150	−0.023	−0.192	−0.194	−0.029	−0.164	0.190
σ	1.167	1.182	1.173	1.193	1.178	1.161	1.194	1.179	1.143	1.209

Table 3: *Final mean ($\bar{x}$) and σ values of Gaussian fits to our g12 pull distributions after applying all corrections. Note that the values for $p\,\pi^+\pi^-\ (\pi^0)$ are based on distributions which cannot be perfect Gaussians owing to the missing-particle hypothesis.*

dependent sagging was a misalignment of the scintillator bars which led to a small shift of the scattered electron's energy [8]. In the CLAS-g12 experiment, the tagger sag was taken into account and corrected in the offline reconstruction code. No further photon energy correction was applied.

3.6.2 Enery-Loss (ELoss) Correction

As charged particles traveled from the production vertex to the active components of the CLAS spectrometer, they lost energy through inelastic scattering, atomic excitation or ionization when interacting with the target, target walls, support structures, beam pipe, Start Counter, and the air gap between the Start Counter and the Region 1 Drift Chambers. Therefore, the momentum reconstructed from the drift chambers was smaller than the momentum of the particle at the production vertex. To account and correct for this, the 4-vectors of the final-state particles were modified event-by-event using the "ELoss" package, which was developed for charged particles moving through CLAS [3]. This ELoss package determined the lost momentum of each particle in the materials it had interacted with. In this procedure, the particle's 4-momentum – as measured by the Region 1 Drift Chambers – was used to track the particle back to the reaction vertex in the target cell. The energy loss was then calculated based on the distance and the materials it traversed. The corresponding 4-vector was corrected by multiplying an ELoss correction factor to the magnitude of the momentum:

$$\begin{aligned} P_{(\,p\,,\,\mathrm{ELoss}\,)} &= \eta_p \cdot P_{(\,p\,,\,\mathrm{CLAS}\,)} \\ P_{(\,\pi^+\,,\,\mathrm{ELoss}\,)} &= \eta_{\pi^+} \cdot P_{(\,\pi^+\,,\,\mathrm{CLAS}\,)} \\ P_{(\,\pi^-\,,\,\mathrm{ELoss}\,)} &= \eta_{\pi^-} \cdot P_{(\,\pi^-\,,\,\mathrm{CLAS}\,)}\,, \end{aligned} \tag{10}$$

where $P_{(\,x\,,\,\mathrm{ELoss}\,)}$ is the momentum of the particle x after applying the energy-loss correction, $P_{(\,x\,,\,\mathrm{CLAS}\,)}$ is the raw momentum measured in CLAS and x is either the proton, π^+, or π^-. The parameters η_p, η_{π^+}, and η_{π^-} are the ELoss correction factors which modified the momentum by a few MeV, on average.

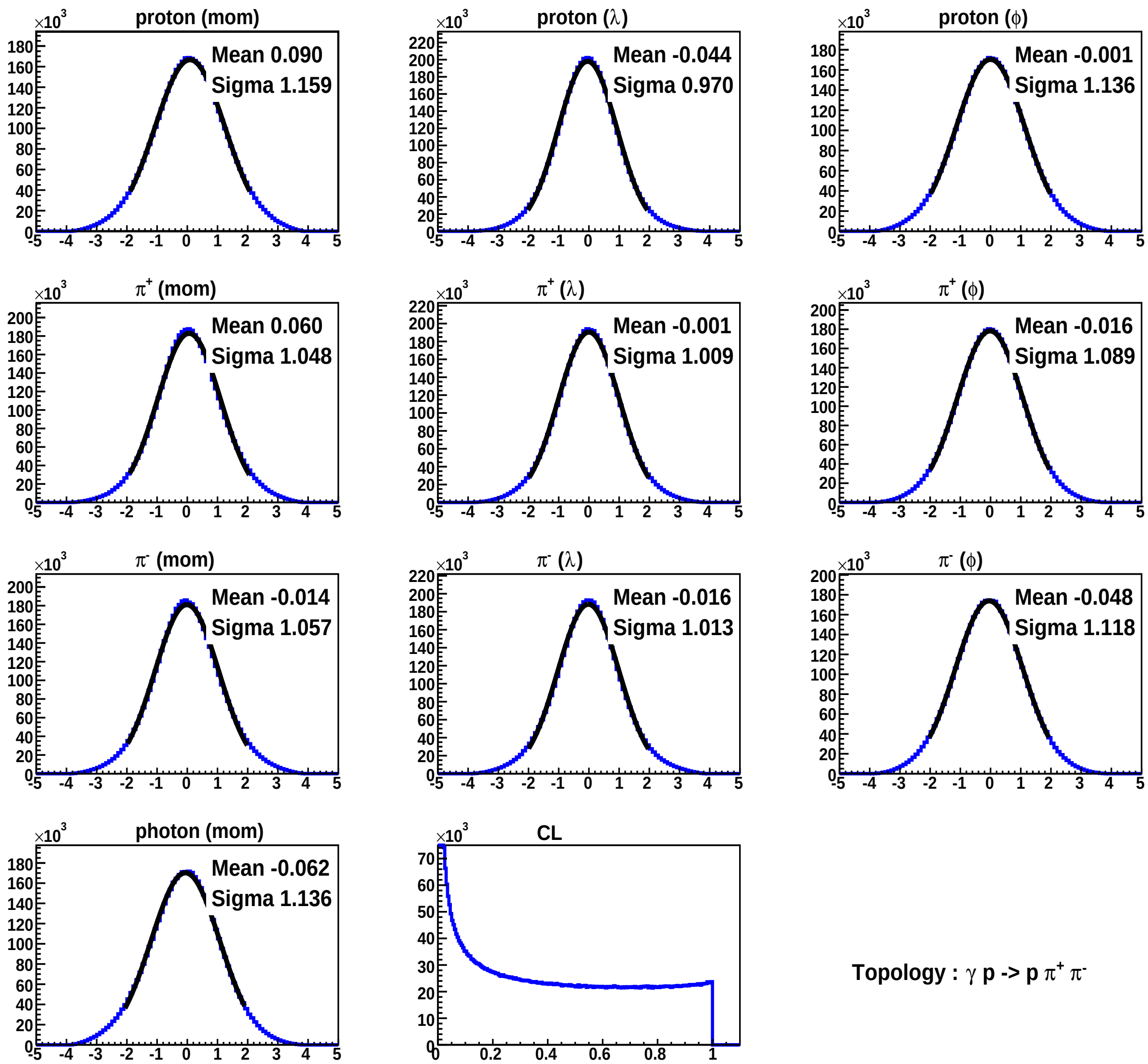

Figure 6: *The g12 pull and confidence-level distributions for the exclusive reaction* $\gamma p \to p\pi^+\pi^-$ *(full statistics of Period 1 & 2). A summary of the mean and* σ *values of the fits can also be found in Table 3.*

3.6.3 Momentum Corrections

The CLAS-g12 experimental setup was not absolutely perfect. For this reason, corrections of a few MeV had to be determined and applied to the final-state particles' momenta to account for unknown variations in the CLAS magnetic field (Torus Magnet) as well as inefficiencies and misalignments of the drift chambers. As a matter of fact, the momenta of the tracks as measured by the drift chambers exhibit a systematic shift within each sector as a function of the azimuthal angle ϕ of one of the tracks [4]. In our FSU analyses, we have followed the CLAS-approved procedure outlined in Ref. [4].

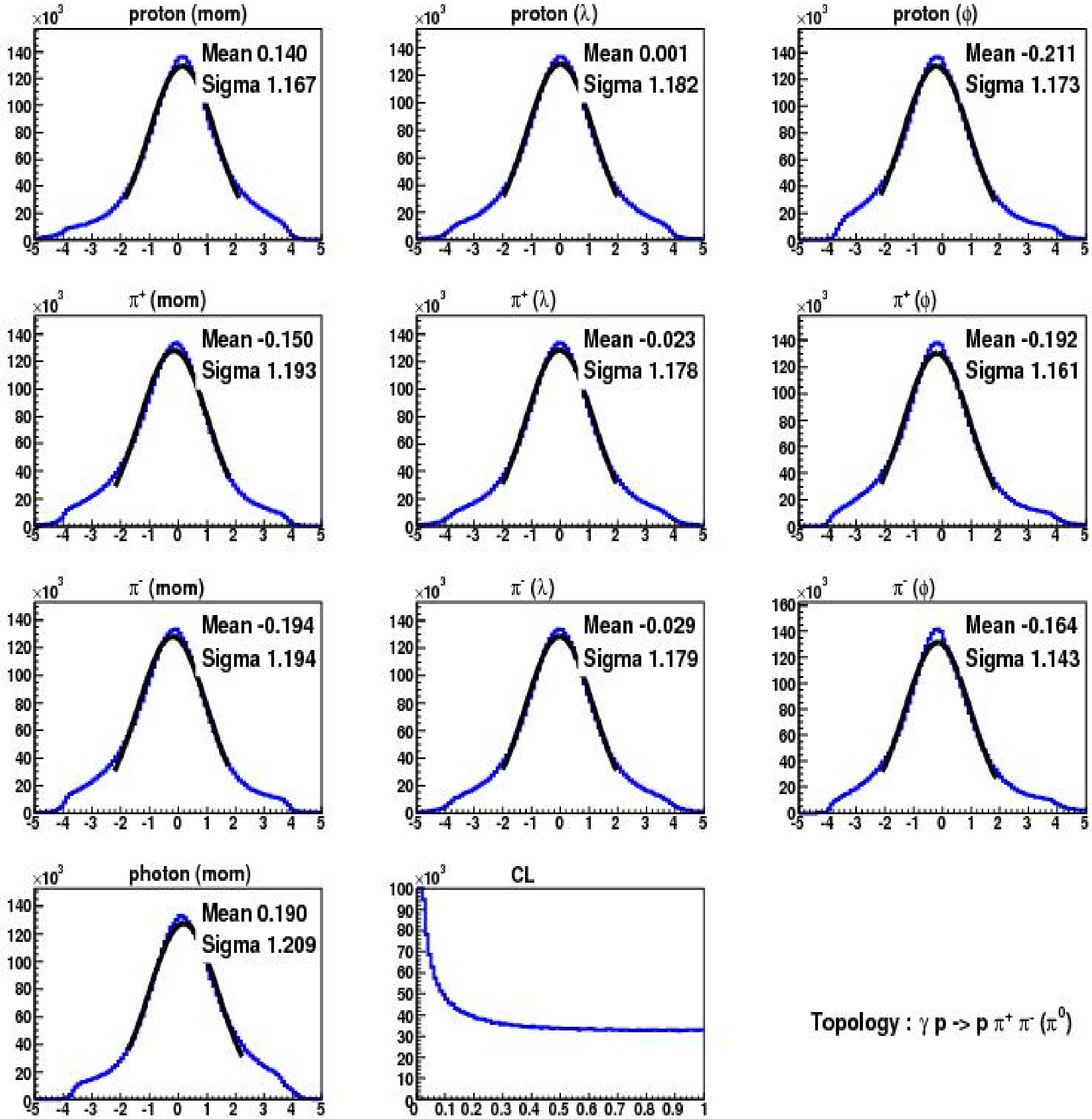

Figure 7: *The g12 pull and confidence-level distributions for the reaction* $\gamma p \to p\pi^+\pi^-\,(\pi^0)$ *(full statistics of Period 1 & 2). Note that the pull distributions are not Gaussian over the full range owing to the missing-particle hypothesis. The confidence-level distribution looks nicely flat, though. A summary of the mean and* σ *values of these fits can also be found in Table 3.* *Bad resolution.*

3.6.4 Bad or Malfunctioning Time-of-Flight Paddles

Some TOF paddles of the CLAS spectrometer were dead or malfunctioning during the g12 experiment. The timing resolution of each paddle was investigated on a run-by-run basis to determine the stability throughout the experiment. Reference [4] contains the results of an extensive study on bad TOF paddles in CLAS-g12. The list of identified bad paddles recommended to knock out is taken directly from Table 19 of Ref. [4] and is also given in Table 4 for convenience.

Sector Number	Bad TOF Paddles in CLAS-g12
1	6, 25, 26, 35, 40, 41, 50, 56
2	2, 8, 18, 25, 27, 34, 35, 41, 44, 50, 54, 56
3	1, 11, 18, 32, 35, 40, 41, 56
4	8, 19, 41, 48
5	48
6	1, 5, 24, 33, 56

Table 4: *The list of bad time-of-flight paddles recommended to knock out [4].*

3.7 Monte Carlo Simulations

To extract the differential cross sections for the reactions (1) $\gamma p \to p\,\omega$, (2) $\gamma p \to p\,\eta$, and (3) $\gamma p \to K^0\,\Sigma^+$, we needed to apply detector-acceptance corrections, where the latter account for the probability that an event of certain kinematics would be detected and recorded (also called efficiency corrections). The performance of the detector was simulated in GEANT3-based Monte-Carlo studies. We followed the steps outlined in Ref. [4] for generating events, digitization and smearing, as well as reconstruction.

The generated raw events were processed by GSIM to simulate the detector acceptance for each propagated track from the event vertex through the GEANT3-modeled CLAS detector. The CLAS smearing package known as GPP then processed the output to reflect the resolution of the detector. Finally, the A1C package was used to perform the *cooking*. We generated a total of 175 million $\gamma p \to p\,\omega \to p\,\pi^+\pi^-\pi^0$ phase-space events for the whole range of incident-photon energies, i.e. $1.1 < E_\gamma < 5.4$ GeV. We have also generated XXX million $\gamma p \to p\,\eta \to p\,\pi^+\pi^-\pi^0$ and XXX million $\gamma p \to K^0\,\Sigma^+ \to p\,\pi^+\pi^-\pi^0$ Monte Carlo events. To guarantee phase-space (generated) events which are flat in $\cos\theta_{\rm c.m.}^{\rm meson}$, we chose a t-slope of *zero*.

In this section, we show the quality of the simulated events by comparing various data distributions with Monte Carlo events:

1. In the CLAS-g12 experiment, the 40-cm-long liquid-hydrogen target was pulled upstream by 90 cm from the center of the CLAS detector. Figure 8 compares the z-vertex distribution for data and Monte Carlo events after applying our cut of $-110 < z$ vertex < -70 cm: $\gamma p \to p\,\omega$ (left) and $\gamma p \to K_S\,\Sigma^+$ (right). This figure shows that the vertex distribution is very well modeled.

2. Figure 9 shows the distributions of θ (polar angle) and ϕ (azimuthal angle) for the proton and for the π^-. The data and Monte Carlo distributions match well for the azimuthal angles of the proton and the π^- as well as for the polar angle of the pion. However, the MC polar angle of the proton (θ_p) does not agree very well with the data. This is reasonable because our Monte Carlo events do not contain any reaction dynamics (simple generation of phase space events), but the distribution covers the same polar-angle range.

3. We also checked all the signal distributions (peaks for ω, η, and K_S) to see if our Monte Carlo mass resolution matches the real detector resolution. Figure 11 shows invariant-mass distributions for both data (black line) and Monte Carlo (red line) events. Since the mass resolution is slightly energy dependent, we compare data and Monte Carlo for $E_\gamma < 3$ GeV (left) and $E_\gamma > 3$ GeV (right). It is observed in this figure that the MC resolution is in reasonable agreement with the actual detector resolution. Need clarification for Σ^+, though.

Reaction	Resolution (width σ of Gaussian)			
	Low Energy		High Energy	
	Data	MC	Data	MC
$\gamma p \to p\,\omega$	7.68	7.98	12.0	12.0
$\gamma p \to p\,\eta$	6.5	6.9	7.2	7.1
$\gamma p \to K_S\,\Sigma^+$	5.4	4.4	5.4	4.8

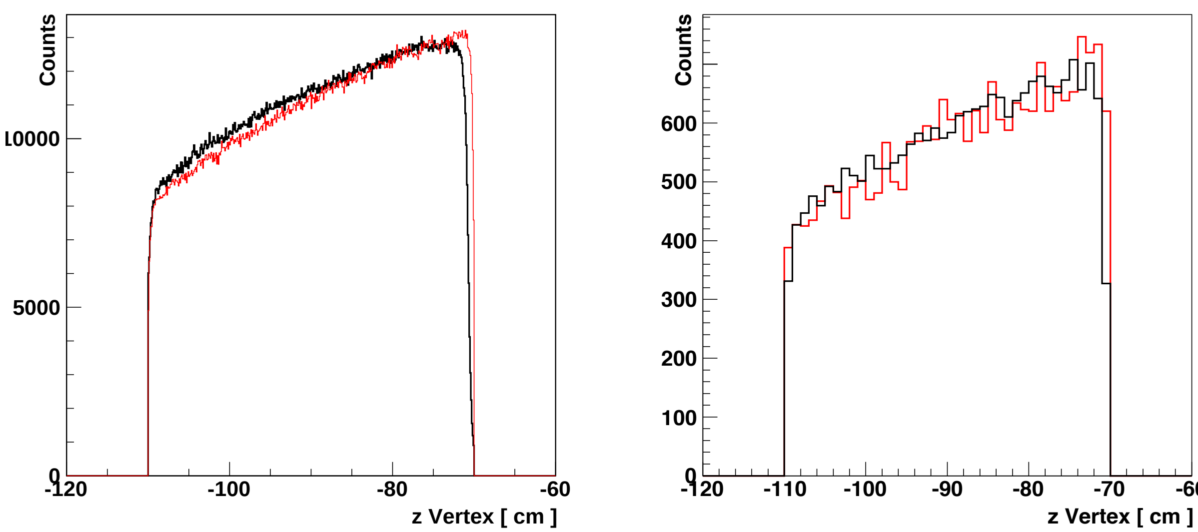

Figure 8: *Left: The z-vertex distribution of $\gamma p \to p\,\omega$ events. The black line denotes the data, the read line denotes the Monte Carlo distribution; good agreement is observed. These figures were made using the full data statistics of 4.4 million events and an equal amount of Monte Carlo events after applying our z-vertex cut of $-110 < z < -70$ cm. Right: The z-vertex distribution of $\gamma p \to K_S\,\Sigma^+$ events.*

	proton			π^+			π^-			γ
	mom.	λ	ϕ	mom.	λ	ϕ	mom.	λ	ϕ	E
Monte Carlo: $\gamma p \to p\pi^+\pi^-$										
$\bar{x}$	0.023	0.003	0.042	0.053	−0.002	0.041	0.053	0.004	0.040	−0.056
σ	1.117	1.045	1.010	1.017	1.028	0.997	1.018	1.048	0.994	1.102
Monte Carlo: $\gamma p \to p\pi^+\pi^-\,(\pi^0)$										
$\bar{x}$	0.040	0.018	0.024	0.027	0.000	0.024	0.022	0.004	0.030	−0.052
σ	1.078	1.054	1.081	1.045	1.056	1.015	1.055	1.056	1.004	1.086

Table 5: *Final mean ($\bar{x}$) and σ values of Gaussian fits to our g12 pull distributions after applying all corrections. Note that the values for $p\,\pi^+\pi^-\,(\pi^0)$ are based on distributions which cannot be perfect Gaussians owing to the missing-particle hypothesis.*

4. Figure 12 shows the distribution of the $\cos\theta^{\pi^-}_{\rm c.m.}$ versus z-vertex for $\gamma p \to p\,\omega$ data and Monte Carlo events; the distributions are almost identical. In the very backward region of the target, an angle range of only about $-0.6 < cos\,\theta^{\pi^-}_{c.m.} < 0.8$ is covered, whereas $-0.8 < cos\,\theta^{\pi^-}_{c.m.} < 0.8$ is covered in the very forward region.

   Figure 13 shows the distribution of x- vs. y-vertex with our cut superimposed. The very good agreement provides confidence in our detector simulations.

5. The quality of the kinematic fitting for the Monte Carlo events is shown in the pull and confidence-level (CL) distributions for the reaction $\gamma p \to p\pi^+\pi^-$ (Fig. 14) and for the reaction $\gamma p \to p\,\omega \to p\pi^+\pi^-\pi^0$ (Fig. 15). A summary of the mean and σ values is given in Table 5. Recall that each of these distributions should have zero mean and width of one. The agreement of the extracted values with these ideal values is very good. The CL distributions are flat toward *one*. To further check the quality of the confidence level in all kinematic regions, we considered the normalized slope of the distribution:

$$\bar{a} \,=\, \frac{a}{a/2\,+\,b}\,, \tag{11}$$

   where a is the slope and b is the intercept obtained by fitting the confidence-level distribution to a linear function. Figure 10 shows examples of confidence-level distributions and their respective normalized slopes. If the errors are overestimated (underestimated), then the confidence-level distribution will have a positive (negative) slope. In line with the procedure outlined in Ref. [12], we would consider the covariance matrix to be aceptable if all kinematic regions yielded normalized slopes in the range $[-0.5, 0.5]$. Figure 16 shows the normalized slopes extracted in $(p,\,\cos\theta)$ bins for the proton and the π^-. Notice that all kinematic regions (excluding edge bins with low statistics) have $|\bar{a}| < 0.5$. Thus, we conclude that the covariance matrix is acceptable.

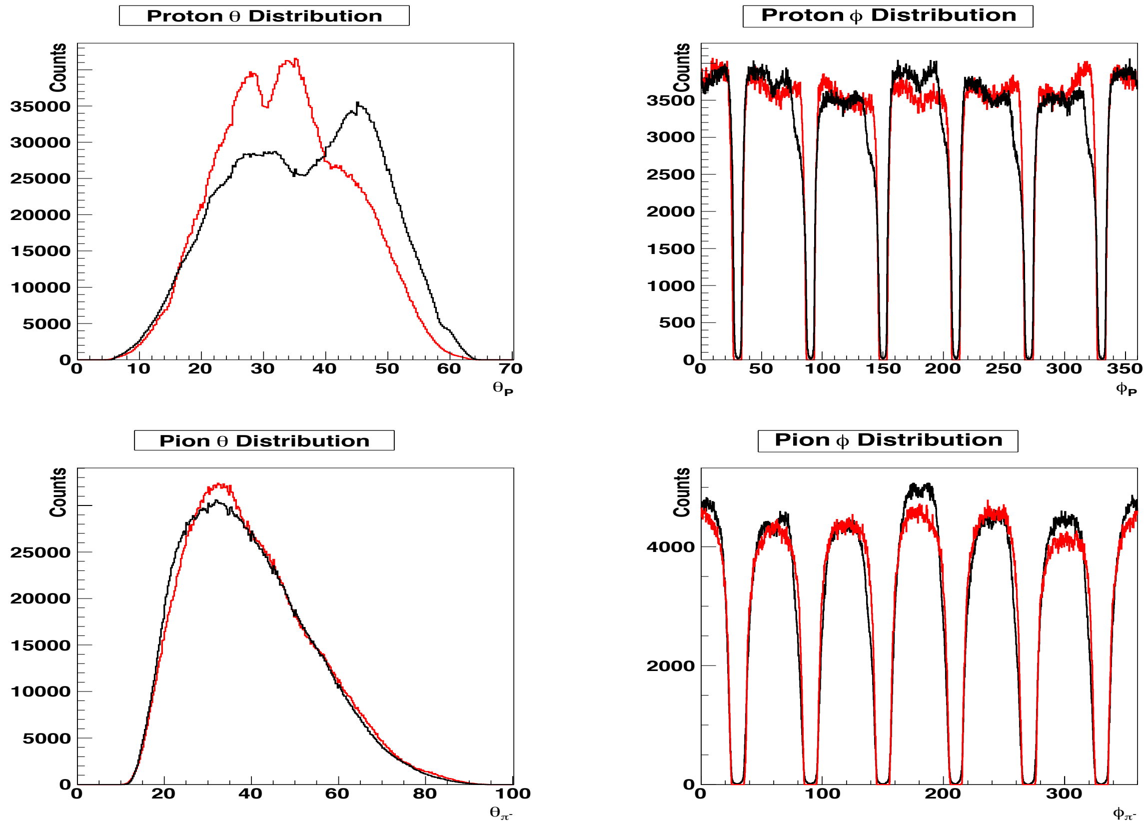

Figure 9: *The polar (θ) and azimuthal (ϕ) angle distributions of the proton (top row) and of the π^- (bottom row) in the reaction $\gamma p \to p\,\omega$ for data (black line) and Monte Carlo events (red line). These figures were made using the full data statistics of 4.4 million events and the same number of Monte carlo events. The θ_{π^-}, ϕ_{π^-} and ϕ_p distributions are in very good agreement.*

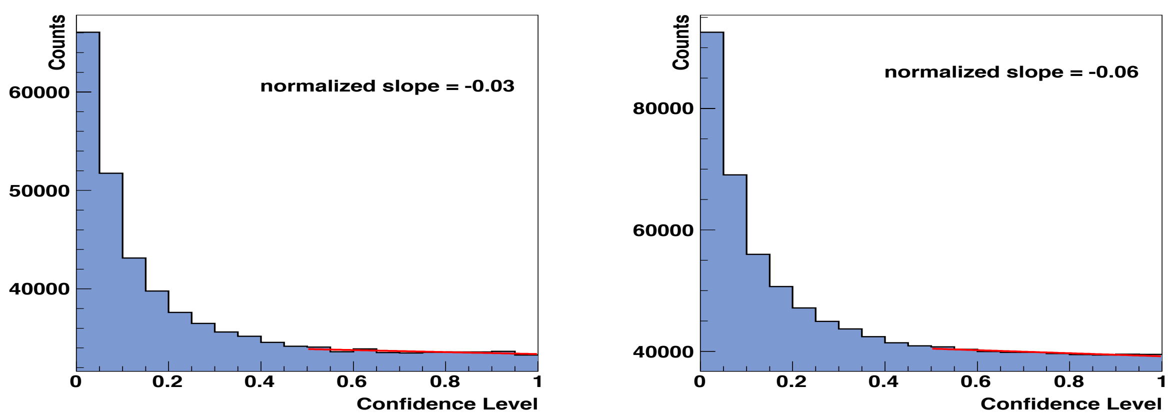

Figure 10: Examples of normalized slopes from confidence-level distributions for the proton (left) and for the π^- (right): Normalized slopes have been extracted by fitting the distributions in the range (0.5, 1) to a linear function.

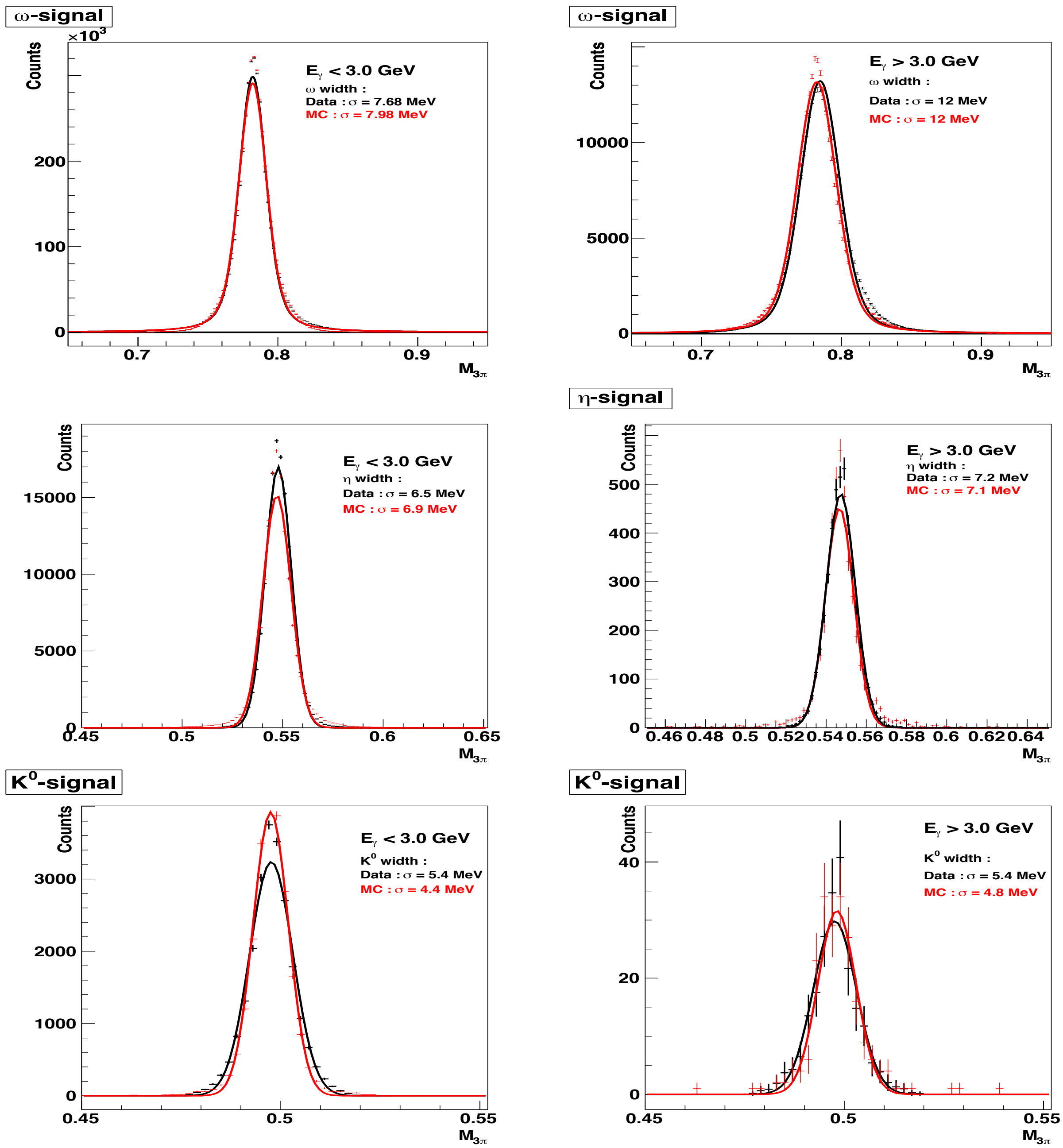

Figure 11: *Invariant mass (signal) distributions for data (black line) and Monte Carlo (red line). The left distributions are for $E_\gamma < 3.0$ GeV, the right distibutions are for $E_\gamma > 3.0$ GeV. Top row: The $M_{\pi^+\pi^-\pi^0}$ distribution showing the ω meson. Middle row: The $M_{\pi^+\pi^-\pi^0}$ distribution showing the η meson. Bottom row: The $M_{\pi^+\pi^-}$ distribution showing the K_S signal. The overall agreement between the data and Monte Carlo distributions indicates that the GEANT simulations model the resolution of the actual detector reasonably well.*

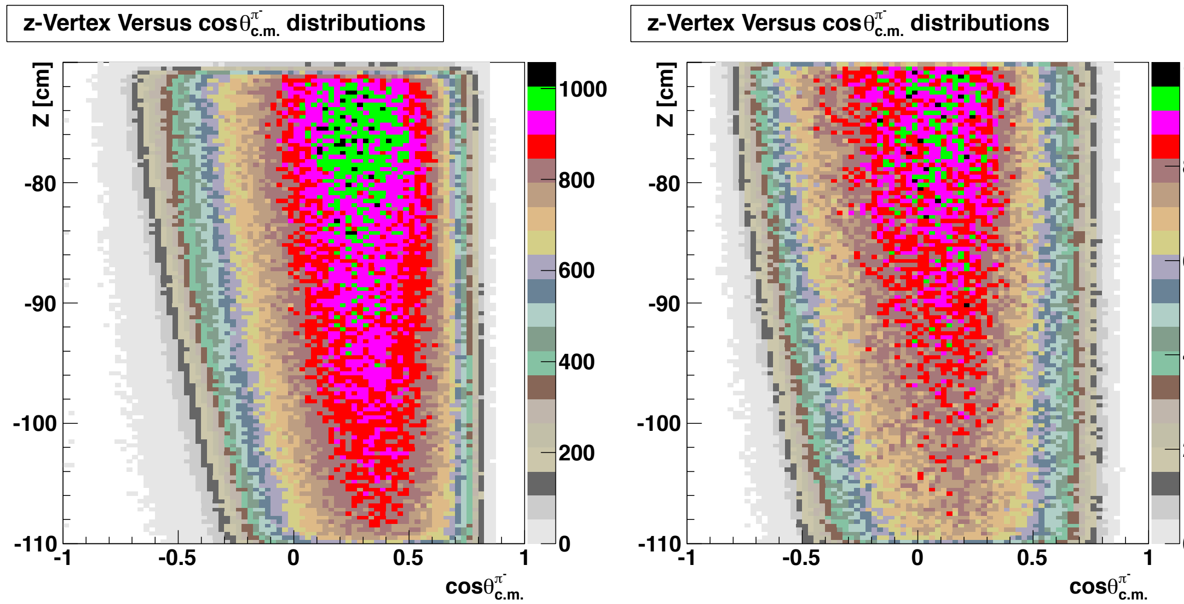

Figure 12: *The z-vertex vs.* $\cos\theta^{\pi^-}_{c.m.}$ *distributions using a logarithmic color scale for data (left) and Monte Carlo events (right); the distributions are very similar. In the very backward region of the target, an angle range of only about* $-0.6 < \cos\theta^{\pi^-}_{c.m.} < 0.8$ *is covered, whereas* $-0.8 < \cos\theta^{\pi^-}_{c.m.} < 0.8$ *is covered in the very forward region.*

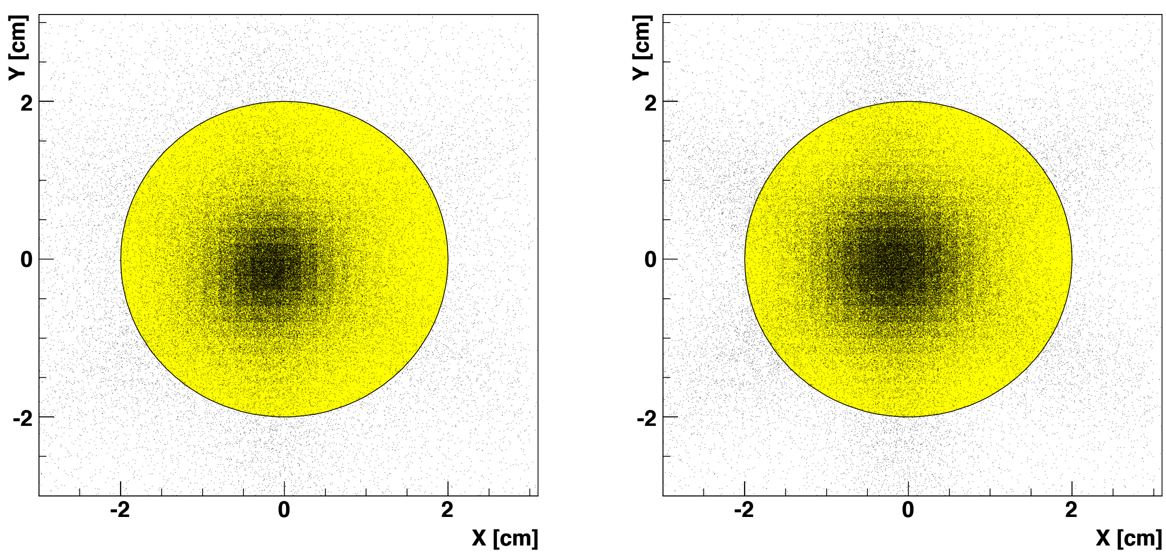

Figure 13: *Left: The x- vs. y-vertex (event) distribution of* $\gamma p \to p\,\pi^+\pi^-\pi^0$ *events from g12 based on our full statistics (Period 1 and 2). Right: The x- vs. y-vertex (event) distribution of* $\gamma p \to p\,\omega \to p\,\pi^+\pi^-\pi^0$ *Monte Carlo events based on all 175 million generated events. The circle on both figures indicates our cut of* $x^2 + y^2 < 2$ *cm*^{2}*. These distributions are in very good agreement.*

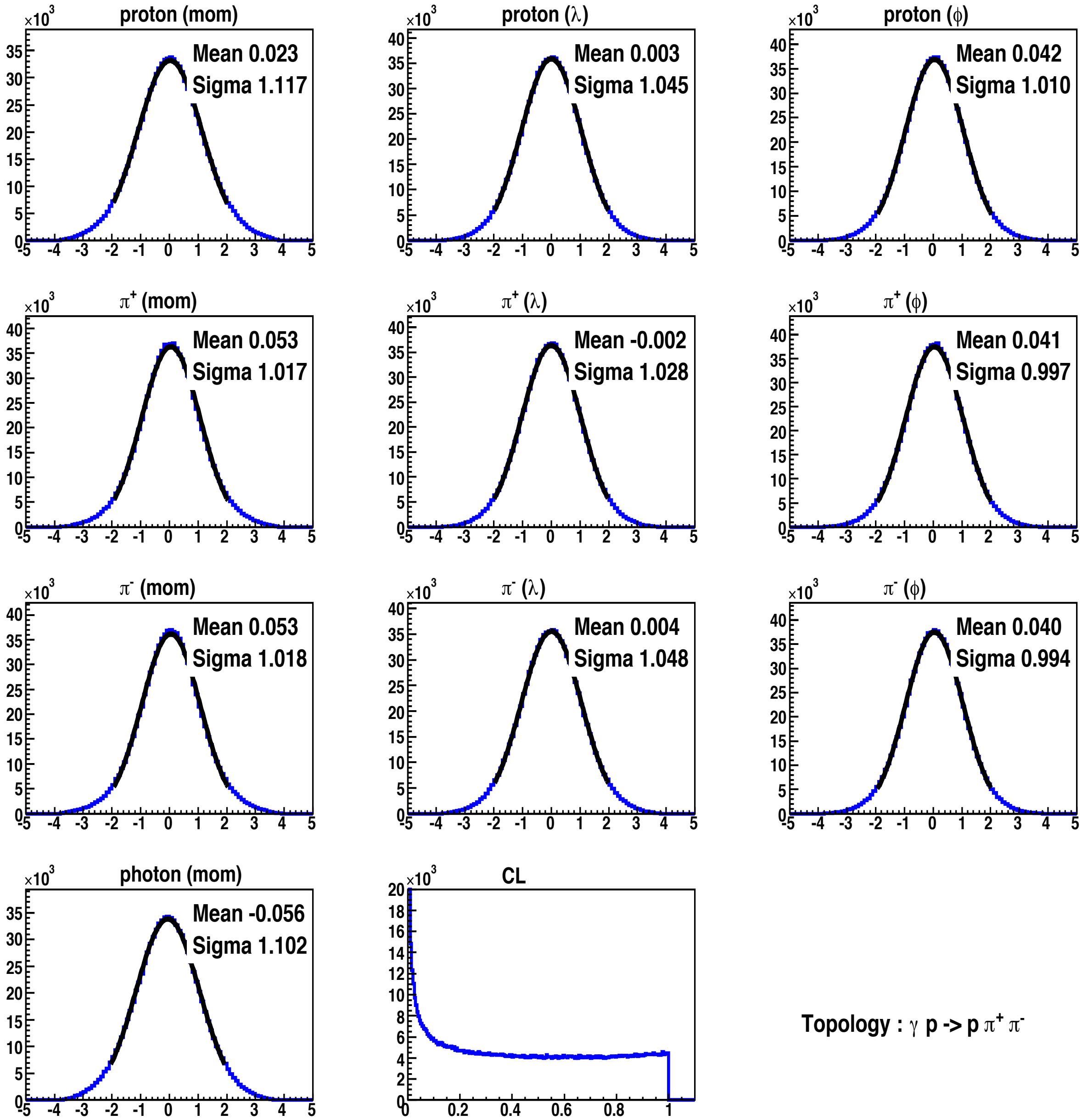

Figure 14: *Monte Carlo (reaction: $\gamma p \to p\,\omega \to p\,\pi^+\pi^-$) pull and confidence-level distributions for the four-constraint fit to $p\,\pi^+\pi^-$ (check for energy and monetum conservation, no mass constraint) along with the mean and σ values of the fits. A summary of the mean and σ values of these fits (for data and Monte Carlo) can also be found in Table 5.*

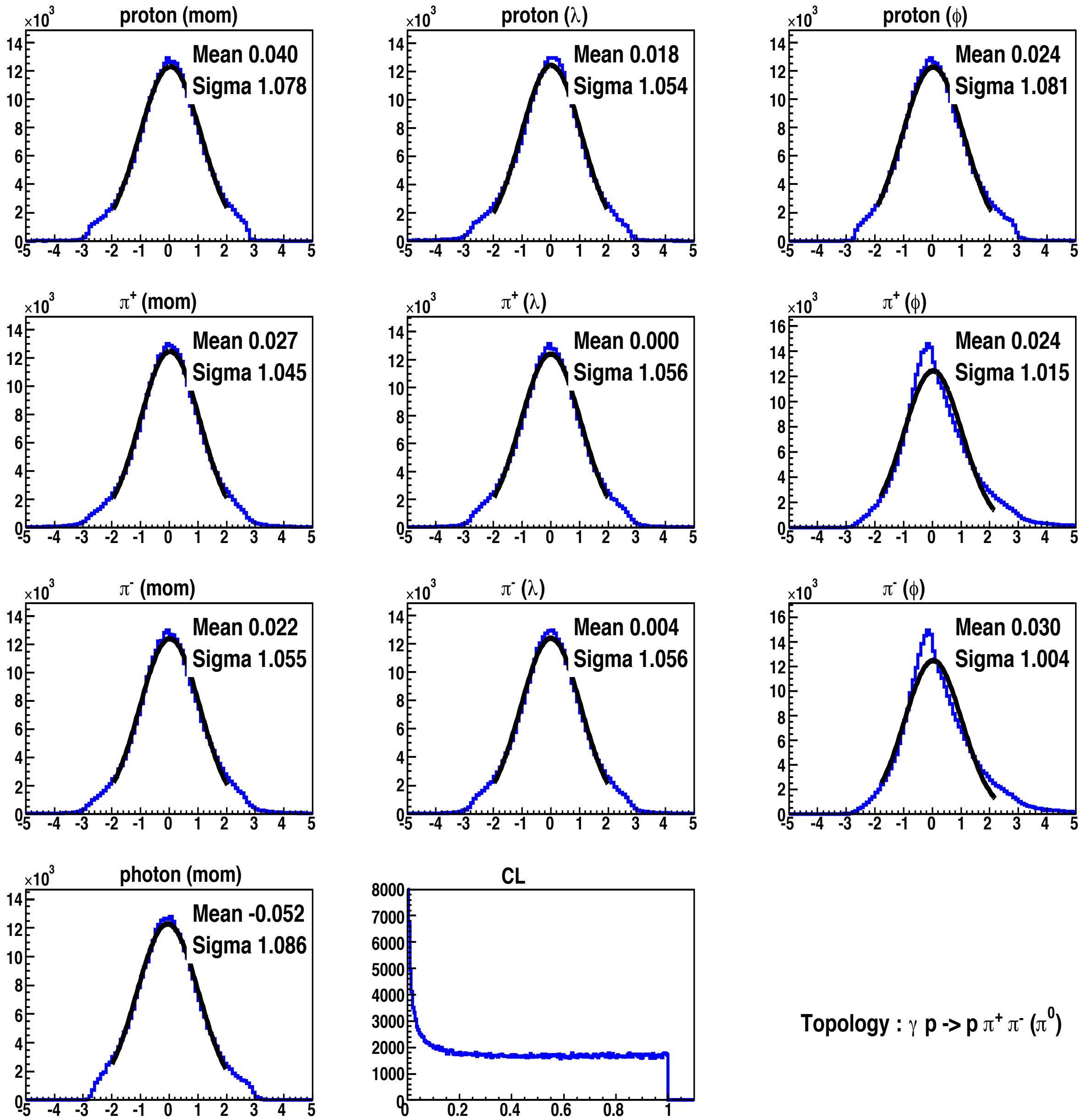

Figure 15: *Monte Carlo (reaction: $\gamma p \to p\,\omega \to p\,\pi^+\pi^-\pi^0$) pull and confidence-level distributions for the one-constraint fit to $p\,\pi^+\pi^-$ (π^0) (no ω-mass constraint) along with the mean and σ values of the fits. Note that the pull distributions are not Gaussian over the full range owing to the missing-particle hypothesis. A summary of the mean and values of these fits (for data and Monte Carlo) can also be found in Table 5.*

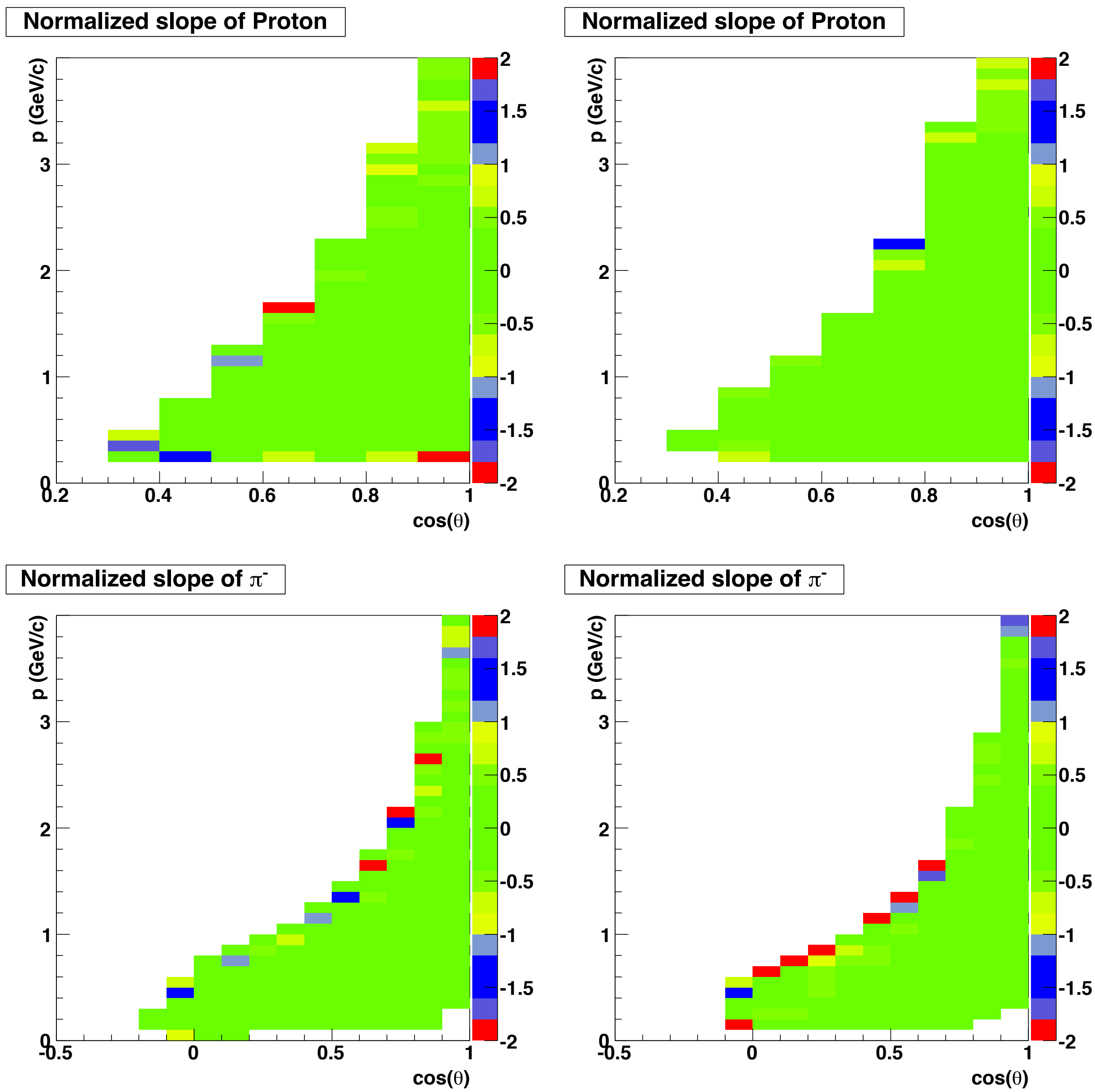

Figure 16: *Confidence Level Checks. Normalized confidence-level slopes presented in* $\cos\theta$ *versus p [GeV/c] distributions for the proton (top row) and for the* π^- *(bottom row). The results for the g12-data are shown on the left and for Monte Carlo on the right. Notice that - excluding edge bins with low statistics - all kinematic regions have* $|\bar{a}| < 0.5$.

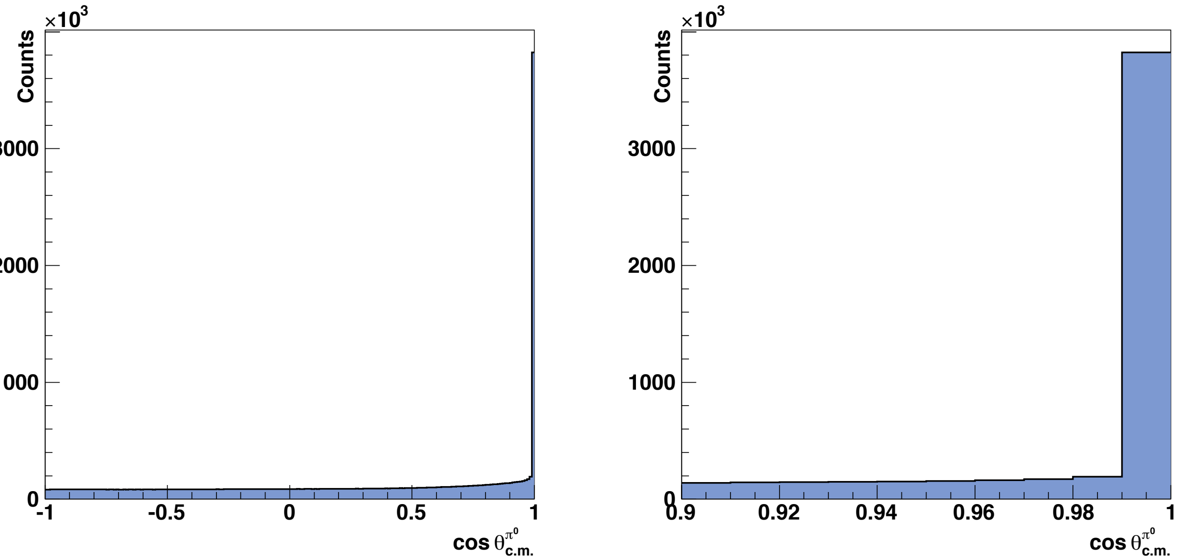

Figure 17: *Left: The* $\cos\theta^{\pi^0}_{\mathrm{c.m.}}$ *distribution of all 18 million* $\gamma p \to p\,\pi^+\pi^-\,(\pi^0)$ *events which pass a* $p > 0.001$ *CL cut. This figure shows an excess of events in the very forward region. Right: The same figure except zoomed in on the forward region.*

3.8 Angular Distribution of the Undetected π^0

The $\cos\theta^{\pi^0}_{\mathrm{c.m.}}$ Distribution

The channel $\gamma p \to p\,\pi^+\pi^-$ has a significantly larger cross section than $\gamma p \to p\,\pi^+\pi^-\,(\pi^0)$. This fact, coupled with the relatively small difference in the missing masses of the two channels, makes $p\,\pi^+\pi^-$ leakage into the $p\,\pi^+\pi^-\,(\pi^0)$ sample a cause for concern. In this section, we consider the possibility of $p\,\pi^+\pi^-$ leakage resulting from selecting the wrong photon.

If the incorrect photon has a higher energy than the correct one, the extra energy will create a fake π^0 that will move along the beam direction. Consider a $\gamma p \to p\,\pi^+\pi^-$ event that was produced in the detector. Our analysis procedure will attempt to reconstruct a π^0 from the missing momentum, $\vec{p}_{\mathrm{miss}}$. Since the event produced was actually a $p\,\pi^+\pi^-$ event, the missing transverse momentum measured should be approximately zero, regardless of whether the correct photon has been found. Thus, the momentum vector of the reconstructed π^0 must point (approximately) along the beam direction: $\vec{p}_{\mathrm{miss}} \approx \pm|\vec{p}_{\mathrm{miss}}|\,\hat{z}$.

Therefore, we expect any leakage from the $\gamma p \to p\,\pi^+\pi^-$ channel, due to an incorrect photon selection, to result in an excess of events in the very forward direction with $\cos\theta^{\pi^0}_{\mathrm{c.m.}} \approx +1$. Figure 17 clearly shows a pronounced excess of events in the very forward direction. Therefore, we cut out all events with $\cos\theta^{\pi^0}_{\mathrm{c.m.}} > 0.99$.

3.9 Fiducial Volume Cuts

Fiducial volume cuts have been applied according to the *nominal* scenario outlined in Section 5.3 of the analysis note [4]. These volumes are regions of the detector that are not well modeled and need to be removed from the analysis. For example, the magnetic field varies rapidly close to the torus coils making these regions difficult to model. Thus, any particle whose trajectory is near a torus coil is removed from our analysis. This cut is most dramatic in the forward region, where the coils occupy a larger amount of the solid angle. There is also a hard cut in the forward direction at $\cos\theta = 0.985$ and a sector-dependent cut in the backwards direction.

3.10 Event Statistics after Applying all Cuts and Corrections

The process of developing and applying energy, momentum and other necessary corrections during the course of this analysis served the purpose of correcting for the effects of the experimental setup, therefore resulting in a data set that was as nature intended it. Additionally, determining and enforcing cuts used in the analysis served not only to remove the remaining instrumental effects of the experimental setup but also to remove the contributions from physics events not of interest to the analysis (the hadronic or electromagnetic background). Through the application of the proper vertex position, photon and particle identification variables, this background could be reduced considerably.

Table 6 shows how many events survived after applying various cuts. The number quoted within parentheses shows the percentage of surviving events.

<table>
<tr><th>Cuts</th><th colspan="4"># of Events (% of Events)</th></tr>
<tr><td>No of initial events after all corrections</td><td colspan="4"></td></tr>
<tr><td>Three tracks (p, π^+, π^-)</td><td colspan="4"></td></tr>
<tr><td rowspan="2">Vertex & $\Delta\beta$ cuts + Topology (CL) Cut</td><td>Topology 4</td><td colspan="3">Topology 5</td></tr>
<tr><td></td><td colspan="3"></td></tr>
<tr><td rowspan="2">Final # of events</td><td>$\gamma p \to p\,\pi^+\pi^-$</td><td>$\gamma p \to p\,\omega$</td><td>$\gamma p \to p\,\eta$</td><td>$\gamma p \to K^0\,\Sigma$</td></tr>
<tr><td></td><td></td><td></td><td>22890</td></tr>
</table>

Table 6: *The table shows the remaining statistics after various cuts.*

3.11 Beam and Target Polarization

3.11.1 Circularly-Polarized Photon Beam - Degree of Polarization

Circularly-polarized photons were produced via bremsstrahlung of longitudinally-polarized electrons from an amorphous radiator. The degree of circular polarization of these bremsstrahlung photons, $\delta_{\odot}$, could be calculated from the longitudinal polarization of the electron beam, δ_{e^-}, multiplied by a numerical factor. Using $x = E_\gamma / E_{\mathrm{e}^-}$, the degree of polarization was given by the Maximon-Olson formula [9]:

$$\delta_{\odot}(x) \,=\, \delta_e \cdot \frac{4x - x^2}{4 - 4x + 3x^2} \,. \tag{12}$$

Figure 18 shows that the degree of circular polarization is roughly proportional to the photon beam energy. In this figure, the photon energy, E_γ, is given as a fraction of the electron-beam energy, E_{e^-} (left) and for the actual g12 incident-photon energy range (right). In the g12 experiment, the electron beam (CEBAF) energy was 5.715 GeV for all the runs that we used in this analysis.

The polarization of the electron beam was measured regularly using the Møller polarimeter, which makes use of the helicity-dependent nature of Møller scattering []. Table 7 summarizes the Møller measurements of the electron-beam polarization, δ_{e^-}. Note that only the second run range (56476 - 56643) was used here. During the g12 experiment, Hall B did not have priority and as a result, the polarization of the beam was delivered as a byproduct (based on the requirements of the other halls). Although the polarization fluctuated, the majority of the g12 runs had a beam polarization close to 70 % with a total uncertainty estimated to be 5 %.

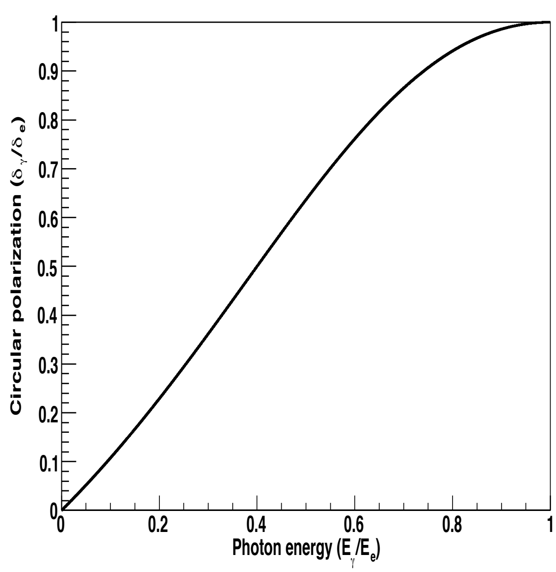

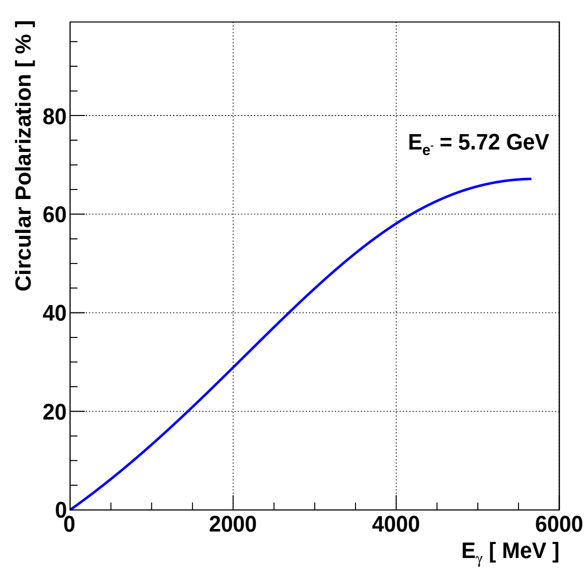

Figure 18: *Left: Degree of circular polarization in units of* $[\delta_\gamma/\delta_{\mathrm{e}^-}]$ *as a function of the fraction of the electron-photon energy. Right: Degree of circular-photon polarization as a function of incident-photon energy for the g12 CEBAF-energy of 5.715 GeV; the electron-beam polarization was 67.17 %.*

The degree of circular polarization was not a continuous function of the center-of-mass energy. Therefore, we used the following equation to determine the polarization for center-of-mass bins:

$$\bar{\delta}_{\odot} = \frac{1}{N^{+} + N^{-}} \sum_{i \in \Delta\tau} \delta_{\odot}(W), \tag{13}$$

where $N^{\pm}$ was the total number of $\gamma p \to p\,\pi^{+}\pi^{-}$ events (used for the observable $I^{\odot}$) for the two helicity states and W was the center-of-mass energy; $\delta_{\odot}(W)$ was calculated from Equation 12. Average values were derived for each center-of-mass bin and are shown in Table 8. Figure **??** shows the degree of circular polarization and their averages for the g12 electron beam energy of 5.715 GeV.

3.11.2 Circularly-Polarized Photon Beam - Orientation of the Helicity States

The direction of the beam polarization depended on the condition of the half-wave plate (HWP) which was either IN or OUT. In CLAS-g12, the longitudinal polarization of the electron beam was flipped pseudo-randomly with 30 sequences of helicity $(+\,,-)$ or $(-\,,+)$ signal per second. Occasionally, the HWP was inserted in the circularly-polarized laser beam of the electron gun to reverse helicities and thus, the beam polarization phase was changed by 180°. The HWP was inserted and removed at semi-regular intervals throughout the experimental run to ensure that no polarity-dependent bias was manifested in the measured asymmetries.

For most of the g12 runs, we had direct reporting of the electron-beam helicity and the information could be retrieved from the "level1-trigger latch word" of the TGBI bank. Bit 16 in this word described the photon helicity state corresponding to the sign of the electron-beam polarization as shown in Table 9.

Run Range	Electron-Beam Polarization δ_{e^-} (Møller Readout)
56355 - 56475	$(81.221 \pm 1.48)\,\%$
56476 - 56643	$(67.166 \pm 1.21)\,\%$
56644 - 56732	$(59.294 \pm 1.47)\,\%$
56733 - 56743	$(62.071 \pm 1.46)\,\%$
56744 - 56849	$(62.780 \pm 1.25)\,\%$
56850 - 56929	$(46.490 \pm 1.47)\,\%$
56930 - 57028	$(45.450 \pm 1.45)\,\%$
57029 - 57177	$(68.741 \pm 1.38)\,\%$
57178 - 57249	$(70.504 \pm 1.46)\,\%$
57250 - 57282	$(75.691 \pm 1.46)\,\%$
57283 - 57316	$(68.535 \pm 1.44)\,\%$

Table 7: *Møller measurements of the electron-beam polarization. Only the run range 56476 - 56643 (highlighted in blue) was used in our analysis (see also Table 1).*

Center-of-Mass Energy [GeV]	Average Degree of Circular Polarization, $\bar{\delta}_{\odot}$ $E_{e^-} = 5.715$ GeV
1.25	
1.30	
1.35	
1.40	
1.45	
1.50	
1.55	
1.60	
1.65	
1.70	
1.75	
1.80	
1.85	
1.90	
1.95	
2.00	
2.05	
2.10	
2.15	
2.20	
2.25	
2.30	
2.35	
2.40	
2.45	
2.50	
2.55	
2.60	
2.65	
2.70	

Table 8: *The average degree of circular (incident photon) polarization for g12 W bins.*

TGBI latch1	Beam Helicity	
Bit 16	$\lambda/2$ (OUT)	$\lambda/2$ (IN)
1	$+$	$-$
0	$-$	$+$

Table 9: *Helicity signal from the TGBI bank for the two half-wave-plate positions. In the table, the sign + (−) denotes the beam polarization was parallel (anti-parallel) to the beam direction. Check if still correct.*

Alternatively, the g12-run group provided the following method:

```
int GetHelicity(clasHEVT_t *HEVT)
{
   int helicity = 0;
   int readout = HEVT->hevt[0].trgprs;
   if(readout > 0) helicity = 1;
   if(readout < 0) helicity = -1;
   return helicity;
}
```

When the HWP was OUT, a bit 16 value of "one" denoted that the beam polarization was parallel to the beam direction and a value of "zero" that the beam polarization was antiparallel to the beam. When the HWP was IN, the directions of the beam polarization were switched. In g12, the HWP setting had to be taken into account by the user performing the analysis. Table 10 shows the HWP settings in the g12 data sets. The information shown in this table was experimentally confirmed by studying the beam asymmetries $I^{\odot}$ in the two-pion channel (see Appendix **??**).

Period	Run Range	HWP Condition
1	55521 - 55536	IN
2	55537 - 55555	OUT
3	55556 - 55595	IN
4	55604 - 55625	IN
5	55630 - 55678	IN
6	56164 - 56193	OUT
7	56196 - 56233	OUT

Table 10: *The HWP condition in the g12 data sets. Update.*

3.11.3 Beam-Charge Asymmetry in Data Sets with Circularly-Polarized Photons

The electron-beam polarization was toggled between the h^+ and the h^- helicity state at a rate of about 30 Hz. At this large rate, the photon-beam flux for both helicity states should be the same, on average. However, small beam-charge asymmetries of the electron beam could cause instrumental asymmetries in the observed *hadronic* asymmetries and had to be taken into account. The beam-charge asymmetry could be calculated from the luminosities of helicity-plus and helicity-minus events:

$$\Gamma^{\pm} \,=\, \alpha^{\pm}\,\Gamma \,=\, \frac{1}{2}\,(1\,\pm\,\bar{a}_c)\,\Gamma\,, \tag{14}$$

where Γ was the total luminosity. The parameter $\alpha^{\pm}$ was used to find the helicity-plus and helicity-minus luminosities, $\Gamma^{\pm}$, from the total luminosity. This parameter depended on the mean value of the electron-beam charge asymmetry, $\bar{a}_c$. The beam-charge asymmetry was typically less than 0.2 % [10]. Since the beam-charge asymmetries were very small, they could be considered negligible.

3.12 Signal-Background Separation: Q-Factor Method

The remaining step in preparing a clean event sample of the reaction in question is the removal of background underneath the signal peak. Figure 19 shows examples of missing-mass distributions for the exclusive $p\,\pi^+\pi^-$ final state where the proton (left) and the π^+ (right) were artificially removed from the data sample and then the missing mass calculated. The figure shows almost background-free distributions and thus, no further background-subtraction method was applied.

The (event-based) Q-factor method used for the background separation in the $p\,\pi^+\pi^-\,\pi^0$ final states ($\gamma p \to p\,\omega \to p\,\pi^+\pi^-\pi^0$, $\gamma p \to p\,\eta \to p\,\pi^+\pi^-\pi^0$, and $\gamma p \to K^0\,\Sigma^+ \to p\,\pi^+\pi^-\pi^0$) is described in the following sections.

Figure 19: *Examples of (background-free) missing-mass distributions for the exclusive $\gamma p \to p\,\pi^+\pi^-$ reaction. Left: Though detected, the proton was removed from the event sample and the missing-mass calculated. Right: The π^+ was removed and the missing-mass calculated.*

3.12.1 General Description

In this event-based method, the set of coordinates that described the multi-dimensional phase space of the reaction were categorized into two types: *reference* and *non-reference* coordinates. The signal and background shapes had to be known *a priori* in the reference coordinate but this knowledge was not required in the non-reference coordinates. Mass was typically chosen as the reference coordinate. For each event, we then set out to find the N_c nearest neighbors in the phase space of the non-reference coordinates. This was similar to binning the data using a dynamical bin width in the non-reference coordinates and making sure that we had N_c events per fit.

The mass distribution of the N_c events (including the candidate event) in the reference coordinate was then fitted with a total function defined as:

$$f(x) \,=\, N \cdot [f_s \,\cdot\, S(x) \,+\, (1 \,-\, f_s) \,\cdot\, B(x)]\,, \tag{15}$$

where $S(x)$ denoted the signal and $B(x)$ the background probability density function. N was a normalization constant and f_s was the signal fraction with a value between 0 and 1. The RooFit package of the CERN ROOT software [11] was used for the fit procedure. Since N_c was usually a small number (of the order of a few hundred events), an unbinned maximum likelihood method was used for the fitting. The Q factor itself was given by:

$$Q \,=\, \frac{s(x)}{s(x) \,+\, b(x)}\,, \tag{16}$$

where x was the value of the reference coordinate for the candidate event, $s(x) = f_s \cdot S(x)$ and $b(x) = (1 - f_s) \cdot B(x)$. The Q factor could then be used as an event weight to determine the signal contribution to any physical distribution.

3.12.2 The Q-Factor Method for the Reaction $\gamma p \to p\,\omega \to p\,\pi^+\pi^-\pi^0$

The kinematic variables that described the reaction $\gamma p \to p\,\omega$ were chosen to be the incident photon energy, E_γ, and the center-of-mass angle of the outgoing ω, $\cos\theta^{\omega}_{\rm c.\,m.}$. Since we reconstructed the ω from its decay into $\pi^+\pi^-\,(\pi^0)$, we also considered the relevant kinematic variables which described the five-dimensional phase space of the 3π system. The ω decay was thus entirely defined by five independent kinematic variables (including the invariant $\pi^+\pi^-\pi^0$ mass we used as *reference* variable). In total, we chose six *non-reference* variables:

- The incident photon energy E_γ (or alternatively, the total center-of-mass energy W),
- The two angles of the ω meson in the helicity frame, $\cos\theta_{\rm HEL}$ and $\phi_{\rm HEL}$,
- The center-of-mass azimuthal and polar angles of the ω, and
- The decay parameter $\lambda \propto |\,\vec{p}_{\pi^+} \,\times\, \vec{p}_{\pi^-}\,|^2$ [12].

The six non-reference coordinates and their maximum ranges used in the Q-factor method are summarized in Table 11.

For the signal-background separation in the $\omega \to \pi^+\pi^-\pi^0$ analysis, we initially applied a small $CL > 0.001$ cut (from kinematic fitting) on the $\gamma p \to p\,\pi^+\pi^-\,(\pi^0)$ final state. This loose CL cut significantly reduced the background, in particular from $\gamma p \to p\,\pi^+\pi^-$ events. We then used the event-based technique to select ω events.

Γ_i	Non-Reference Coordinate	Maximum Range Δ_i
Γ_0	$\cos\Theta^{\omega}_{\mathrm{c.\,m.}}$	2
Γ_1 & Γ_2	$\cos\theta_{\mathrm{HEL}}$ and ϕ_{HEL}	2 & 2π [radians]
Γ_3	$\phi^{\omega}_{\mathrm{lab}}$	2π [radians]
Γ_4	λ	1
Γ_5	incident photon energy E_γ (or W)	20 MeV (10 MeV below $W = 2.1$ GeV)

Table 11: *The non-reference coordinates Γ_i and their ranges Δ_i.*

The data were divided into data subsets based on the photon energy (20-MeV wide bins). We chose the number of 1000 nearest-neighbor events for each candidate event in the phase space spanned by the non-reference coordinates. The $\pi^+\pi^-\pi^0$ invariant mass distribution of these 1000 events was then fitted over the mass range 650 - 900 MeV using the unbinned maximum-likelihood technique. Since the natural width of the ω meson is 8.49 MeV and thus, at the level of the detector resolution, we chose a Voigtian function for the signal pdf. The Voigtian function is a convolution of a Gaussian, which was used to describe the resolution, and a Breit-Wigner, which described the natural line shape of the resonance. The background shape was modeled with a second-order Chebychev polynomial for incident photon energies above 1400 MeV. Close to the reaction threshold of $E_\gamma \approx 1109$ MeV, the ω signal peak is located very close to the upper 3π phase space boundary. For this reason, we chose an Argus function instead of a Chebychev polynomial to describe the background shape.

Table 12 shows the parameters of the signal and background pdfs and the constraints imposed on them. The two pdfs were used to construct a total pdf (see Equation 15) and the Q factor of the candidate event was extracted using Equation 16.

Probability Density Function	Parameters	Initial Value	Fit Range
Voigtian	mean, μ	782.65 MeV [5]	fixed
	width, σ	8.0 MeV	0 - 30 MeV
	natural width, Γ	8.49 MeV [5]	fixed
Chebychev ($E_\gamma > 1.4$ GeV)	c_0	0.5	0.0 - 1.8
	c_1	0.1	-1.2 - 1.2
Argus ($E_\gamma < 1.4$ GeV)	endpoint, m_0	820 MeV	790.0 - 950.0 MeV
	slope, c	-1.0	-10.0 - 0.2

Table 12: *Parameters of the signal and background probability-density functions. A Voigtian was used to describe the ω signal and a second-order Chebychev polynomial (an Argus function for $E_\gamma < 1.4$ GeV) was used to describe the background over the $\pi^+\pi^-\pi^0$ mass range 650 - 900 MeV.*

Quality Checks

1. Once the fit parameters were determined in an individual likelihood fit, we performed a least-square "fit" of the same mass distribution from the 1000 events. Among other things, this allowed us to plot the distribution of reduced-χ^2 values as a goodness-of-fit measure. The left column of Figure 20 shows several such reduced-χ^2 distributions for a few randomly-selected example E_γ bins: (top to bottom row) $E_\gamma \in [1.64,\, 1.66]$ GeV, $E_\gamma \in [2.10,\, 2.12]$ GeV, $E_\gamma \in [4.00,\, 4.02]$ GeV, $E_\gamma \in [5.00,\, 5.02]$ GeV. These reduced-χ^2 distributions peak fairly close to the ideal value of *one*. Given the fairly small number of events in these distributions, we also concluded that the fitter picks up statistical fluctuations. This resulted in overconstrained fits and slightly smaller reduced-χ^2 values, about 07 - 0.8 on average.

2. Defined in terms of the pion momenta in the rest frame of the ω meson, the quantity $\lambda = |\,\vec{p}_{\pi^+} \times \vec{p}_{\pi^-}|^2 \,/\, \lambda_{\rm max}$ is proportional to the $\omega \to \pi^+\pi^-\pi^0$ decay amplitude as a consequence of isospin conservation [**?**] with $\lambda_{\rm max}$ defined as [**?**]

$$\lambda_{\rm max} \,=\, Q^2 \left(\frac{Q^2}{108} \,+\, \frac{mQ}{9} \,+\, \frac{m^2}{3} \right) \tag{17}$$

   for a totally symmetric decay, where $Q = T_1 + T_2 + T_3$ is the sum of the $\pi^{\pm,\,0}$ kinetic energies and m is the π mass. The parameter λ varies between 0 and 1 and shows a linearly-increasing distribution as expected for a vector meson.

   Figure 20 (center column) shows the λ distributions for the same energy bins as for the corresponding reduced-χ^2 distributions in the left column. The (red) signal was generated by weighting event-by-event the (black) full distribution with the Q values; the (blue) background distribution was generated by weighting the full distribution with $1 - Q$. The linear behavior of the ω signal events is clearly visible.

Finally, $\omega \to \pi^+\pi^-\pi^0$-mass distributions showing the full statistics in a given energy bin are presented in Figure 20 (right column) for the selected E_γ bins discussed above and in 20-MeV-wide bin for the entire CLAS-g12 energy range in Figures 21 - 24. Since we analyzed a total of 215 energy bins, we show the mass distribution for every sixth energy bin in these figures.

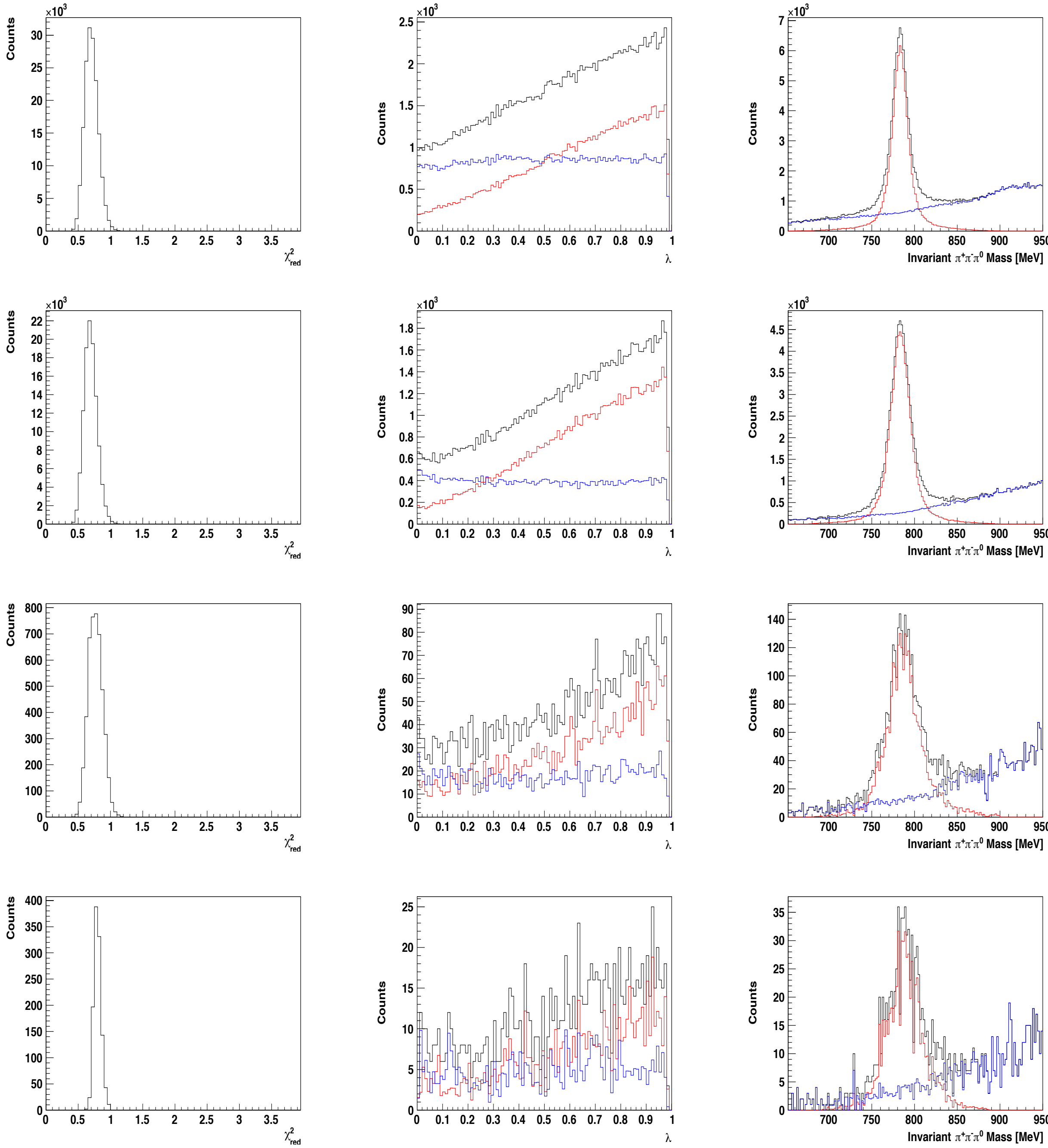

Figure 20: *Quality checks - shown are randomly selected E_γ bins across a wide range in the incident photon energy: (top to bottom row) $E_\gamma \in [1.64, 1.66]$ GeV, $E_\gamma \in [2.10, 2.12]$ GeV, $E_\gamma \in [4.00, 4.02]$ GeV, $E_\gamma \in [5.00, 5.02]$ GeV. (Left column) Examples of reduced-χ^2 distributions. (Center) Examples of λ distributions. (Right) The full mass distribution for the energy bin. The black line denotes the full distribution, the red line the signal, and the blue solid line the background distribution.*

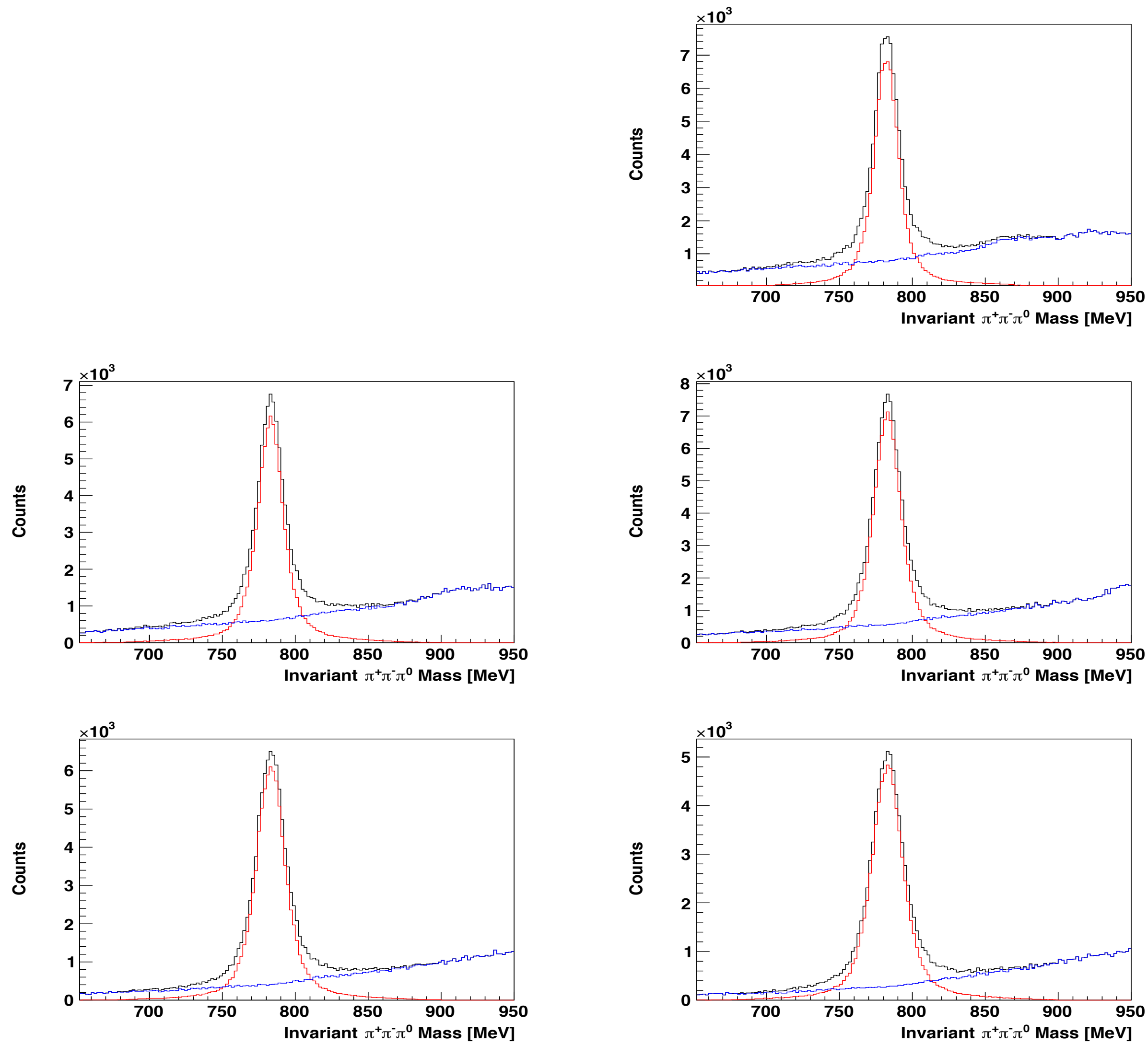

Figure 21: *Invariant $\pi^+\pi^-\pi^0$ mass distributions for the reaction $\gamma p \to p\,\omega$. Shown is every sixth 20-MeV-wide E_γ bin starting at $E_\gamma \in [1200, 1220]$ MeV (top left), $E_\gamma \in [1220, 1240]$ MeV (top right), etc.*

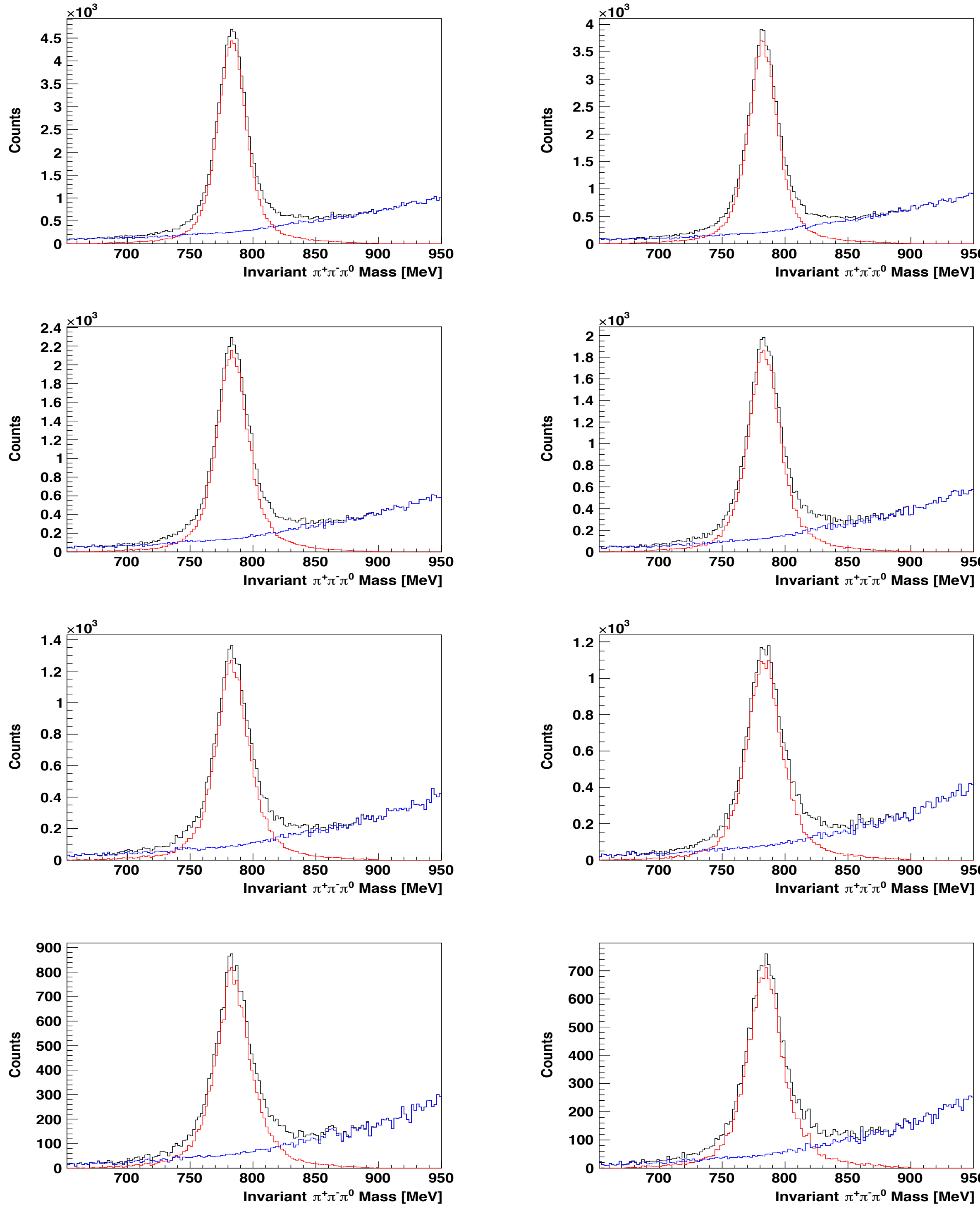

Figure 22: *Invariant $\pi^+\pi^-\pi^0$ mass distributions for the reaction $\gamma p \to p\,\omega$. Shown is every sixth 20-MeV-wide E_γ bin starting at $E_\gamma \in$ [2120, 2140] MeV (top left), $E_\gamma \in$ [2140, 2160] MeV (top right), etc.*

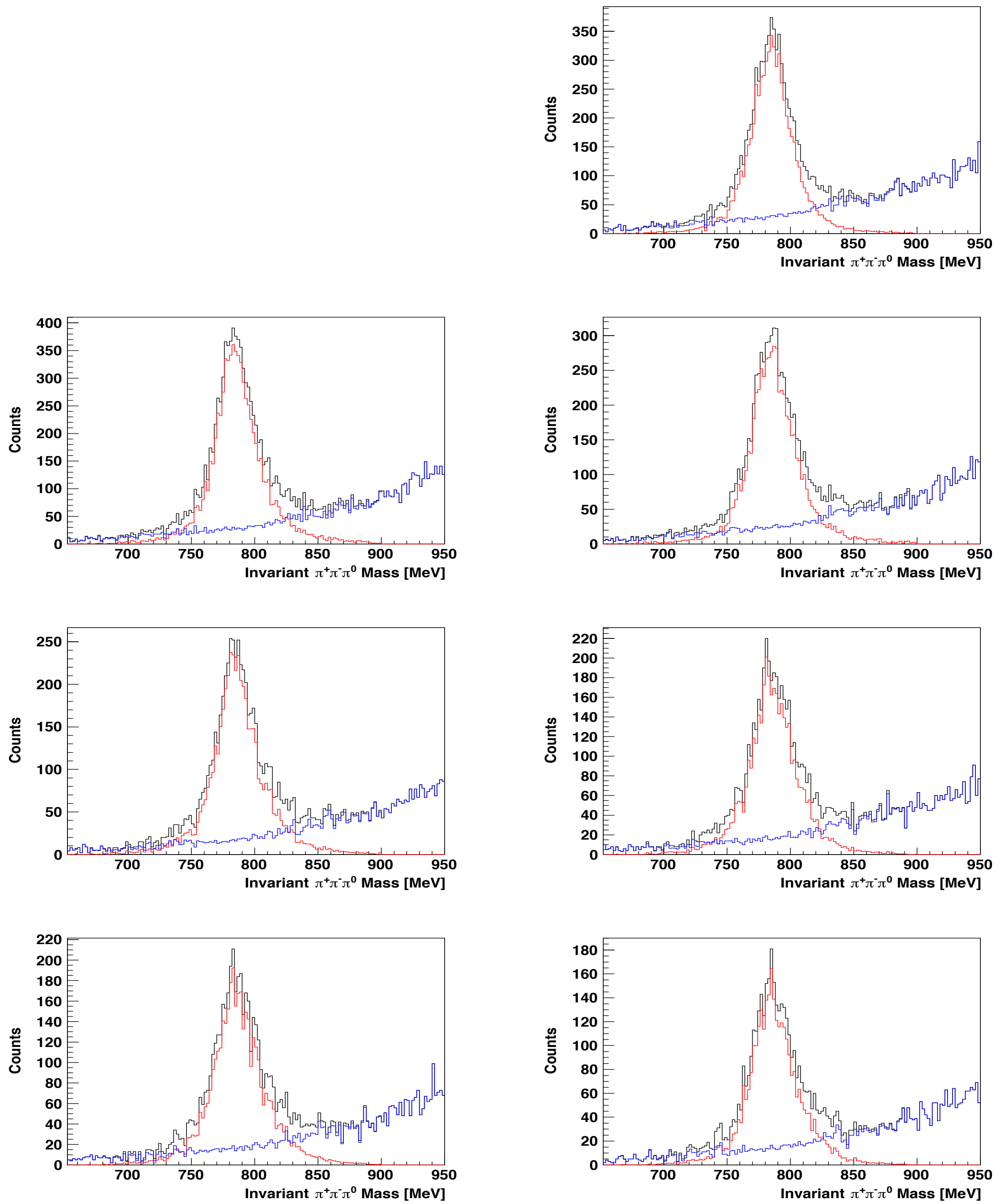

Figure 23: *Invariant $\pi^+\pi^-\pi^0$ mass distributions for the reaction $\gamma p \to p\,\omega$. Shown is every sixth 20-MeV-wide E_γ bin starting at $E_\gamma \in [3200, 3220]$ MeV (top right). The [3080, 3100] MeV bin is missing owing to tagger inefficiencies.*

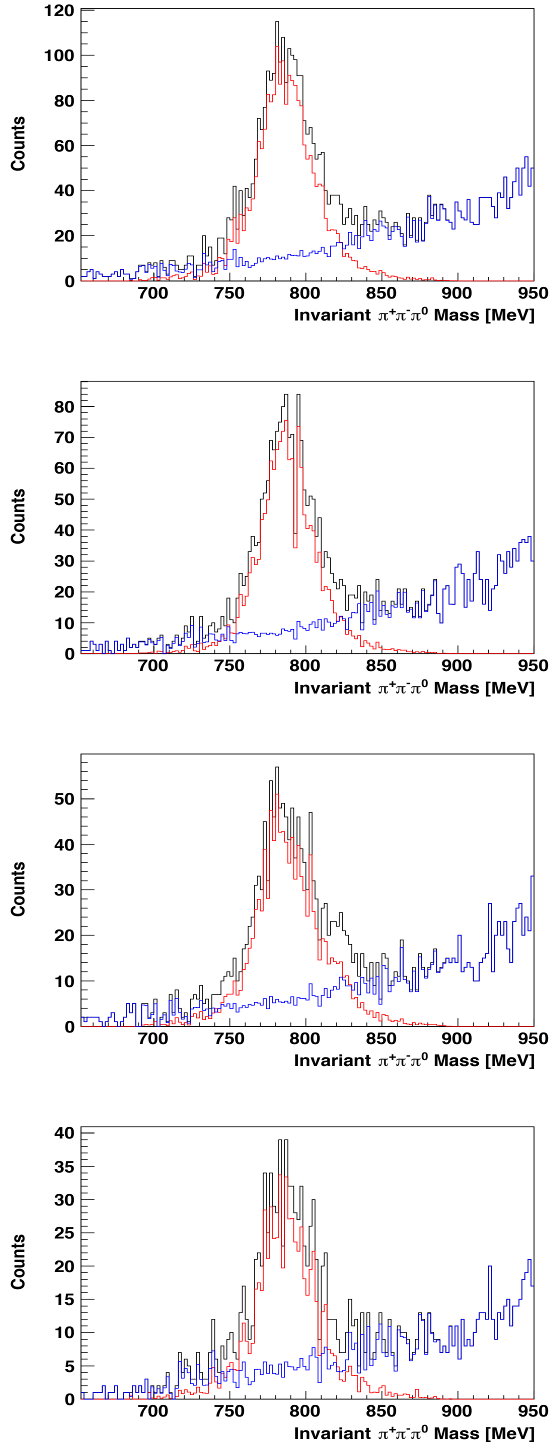

Figure 24: *Invariant $\pi^+\pi^-\pi^0$ mass distributions for the reaction $\gamma p \to p\,\omega$. Shown is every sixth 20-MeV-wide E_γ bin starting at $E_\gamma \in [4080, 4100]$ MeV (top left), $E_\gamma \in [4200, 4220]$ MeV (top right), etc.*

3.12.3 The Reaction $\gamma p \to p\,\eta \to p\,\pi^+\pi^-\pi^0$

The reconstruction of the η meson is based on its $\pi^+\pi^-\pi^0$ decay mode and therefore, the invariant $\pi^+\pi^-\pi^0$ mass was used as the reference coordinate. The non-reference coordinates are the same as those used for the ω meson and are summarized in Table 11. The quantity λ may not have a direct physical meaning in the η decay but in defining the phase space for the nearest-neighbors search, it still serves as an independent kinematic variable.

The η meson has a natural width of $\Gamma = 1.31 \pm 0.05$ keV [5]. For this reason, the observed width of the η signal is dominated by the experimental resolution and the lineshape should be describable by a Gaussian. However, we noticed that a simple Gaussian could not describe very well the very low- and high-mass tails of the signal peak, which caused some enhancements in the background description. A double-Gaussian in combination with a second-order Chebychev polynomial for the background solved this issue. Table 13 summarizes the parameters of the signal and background pdfs and the constraints imposed on them.

To compare with published CLAS results [], we have used the following binning scheme in W:

1. $W \in [1720,\ 2100]$ MeV in 10-MeV-wide W bins ($E_\gamma \in [1707,\ 1881]$ MeV),
2. $W \in [2100,\ 2360]$ MeV in 20-MeV-wide W bins ($E_\gamma \in [1881,\ 2499]$ MeV),
3. $W \in [2360,\ 3320]$ MeV in 40-MeV-wide W bins ($E_\gamma \in [2499,\ 5405]$ MeV).

Figures 25 - 28 show the invariant $\pi^+\pi^-\pi^0$ mass distributions for the $W \in [1720,\ 2070]$ MeV range, which corresponds to about $E_\gamma \in [1107,\ 1814]$ MeV. The black solid line denotes the full mass distribution, the red solid is the signal, and the blue solid line represents the background distribution. Note that $E_\gamma = 1100$ MeV is at the very low end of the tagging range. For this reason, the first truly available W bin is 1750 - 1760 MeV; the statistics is still low, though. Full statistics is then available in CLAS-g12 from $W = 1760$ MeV (Fig. 25, top row). The background exhibits an almost linear behavior but we chose a second-order polynomial and a slightly broader fit range of 455 - 650 MeV to avoid ambiguities between the background pdf and the second (broader) signal Gaussian. The broader fit range also required us to use 500 events (up from initially 300 events) in the search for nearest neighbors to accumulate sufficient signal statistics in the individual mass distributions. Finally, Fig. 29 shows the $\pi^+\pi^-\pi^0$ distributions for the $W \in [2360,\ 2680]$ MeV range.

Probability Density Function	Parameters	Initial Value	Fit Range
Gaussian I	Mean, μ	547.86 [5] MeV	fixed
	Width, σ	5.0 MeV	1.5 - 9.5 MeV
Gaussian II	Mean, μ	548.40 MeV	540.0 - 560.0 MeV
	Width, σ	10.0 MeV	6.0 - 28.0 MeV
Chebychev	c_0	0.8	0.0 - 1.6
	c_1	0.19	-0.6 - 1.5

Table 13: *Parameters of the signal and background probability-density functions. A double-Gaussian was used to describe the η signal and a second-order Chebychev polynomial was used to describe the background over the $\pi^+\pi^-\pi^0$ mass range 455-650 MeV.*

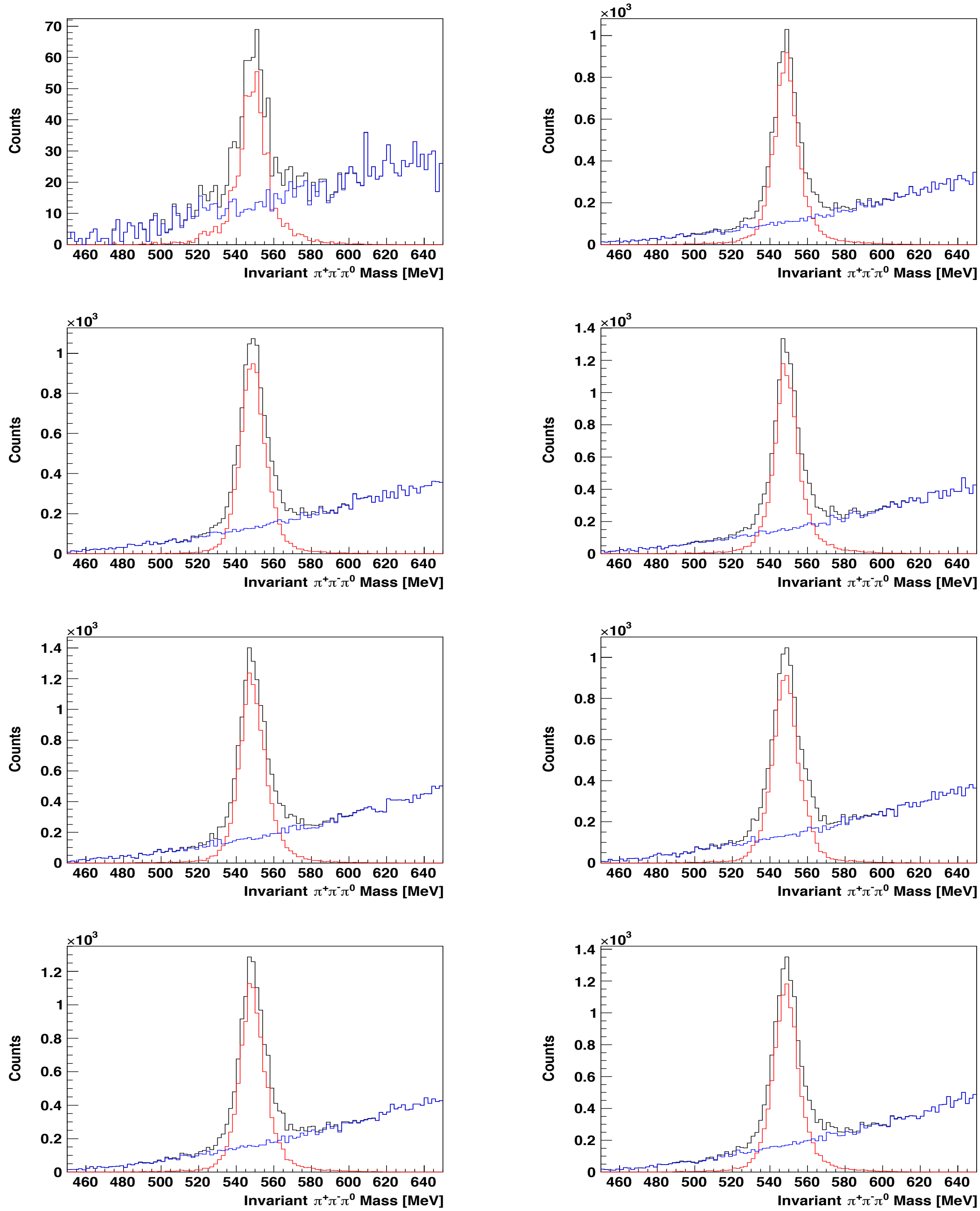

Figure 25: *Invariant $\pi^+\pi^-\pi^0$ distributions for the reaction $\gamma p \to p\eta$. Shown are 10-MeV-wide W bins starting at $W \in [1750, 1760]$ MeV (top left), $W \in [1760, 1770]$ MeV (top right), etc.*

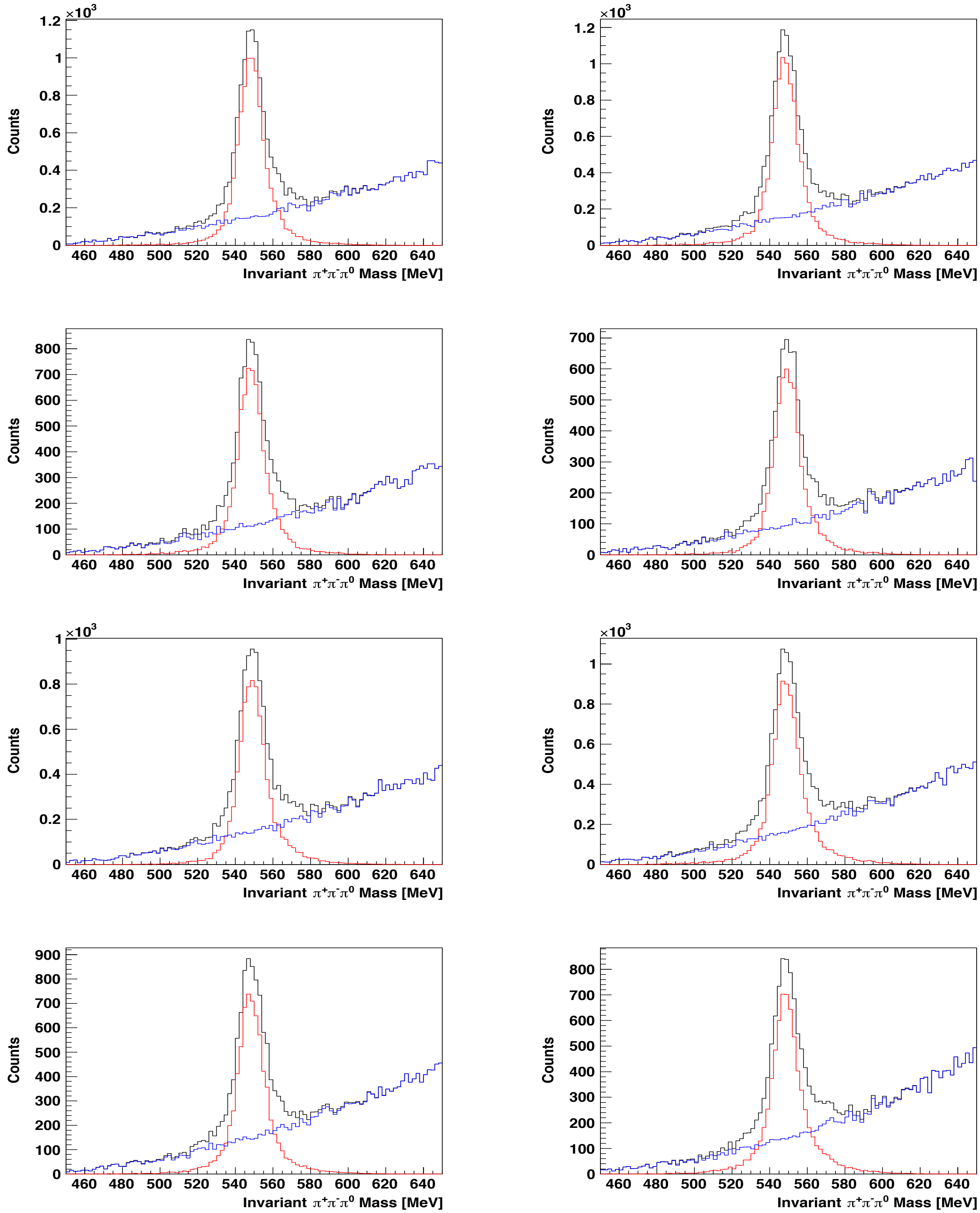

Figure 26: *Invariant* $\pi^+\pi^-\pi^0$ *distributions for the reaction* $\gamma p \to p\eta$*. Shown are 10-MeV-wide* W *bins starting at* $W \in [1830, 1840]$ *MeV (top left),* $W \in [1840, 1850]$ *MeV (top right), etc.*

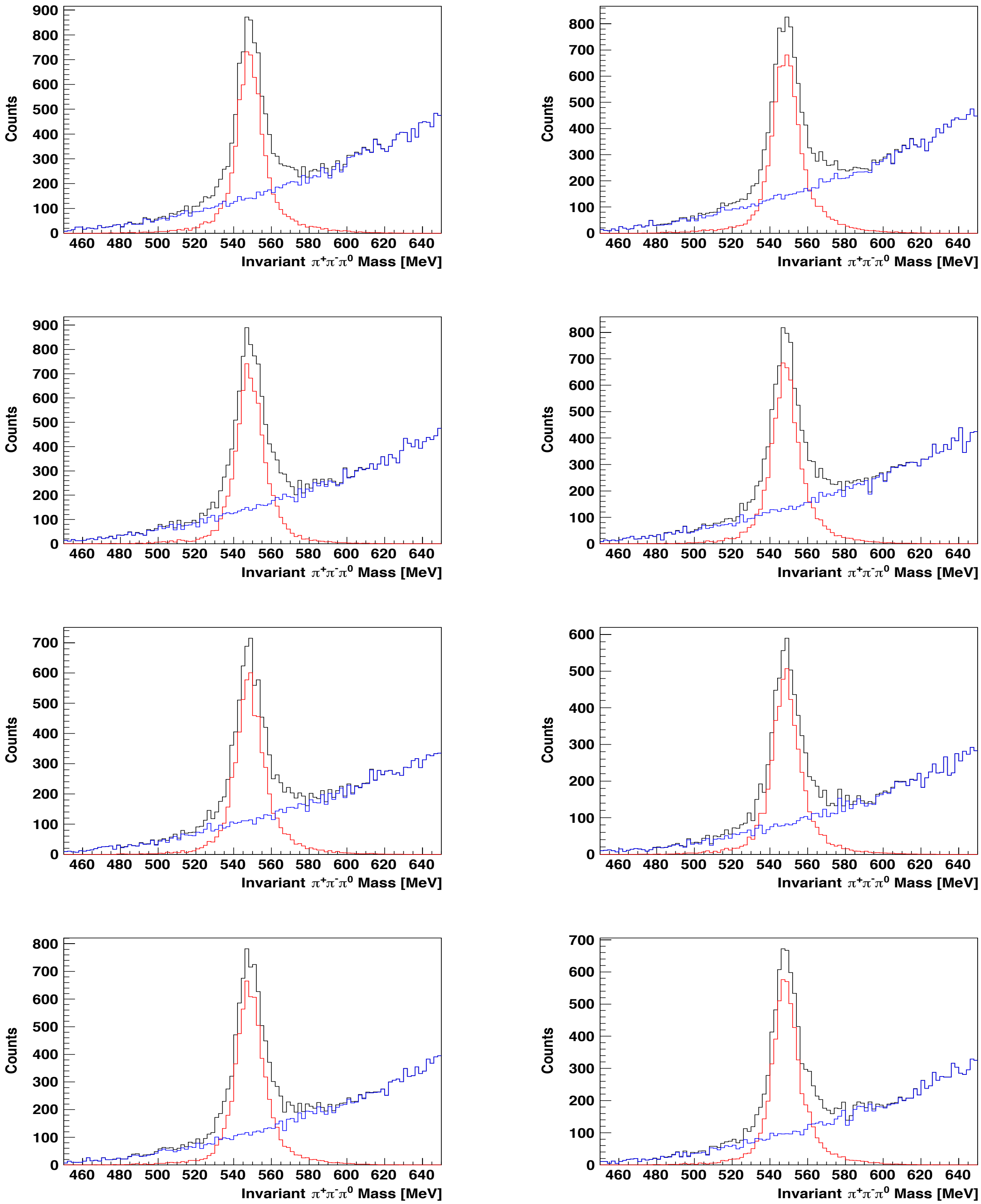

Figure 27: *Invariant* $\pi^+\pi^-\pi^0$ *distributions for the reaction* $\gamma p \to p\eta$*. Shown are 10-MeV-wide* W *bins starting at* $W \in [1910, 1920]$ *MeV (top left),* $W \in [1920, 1930]$ *MeV (top right), etc.*

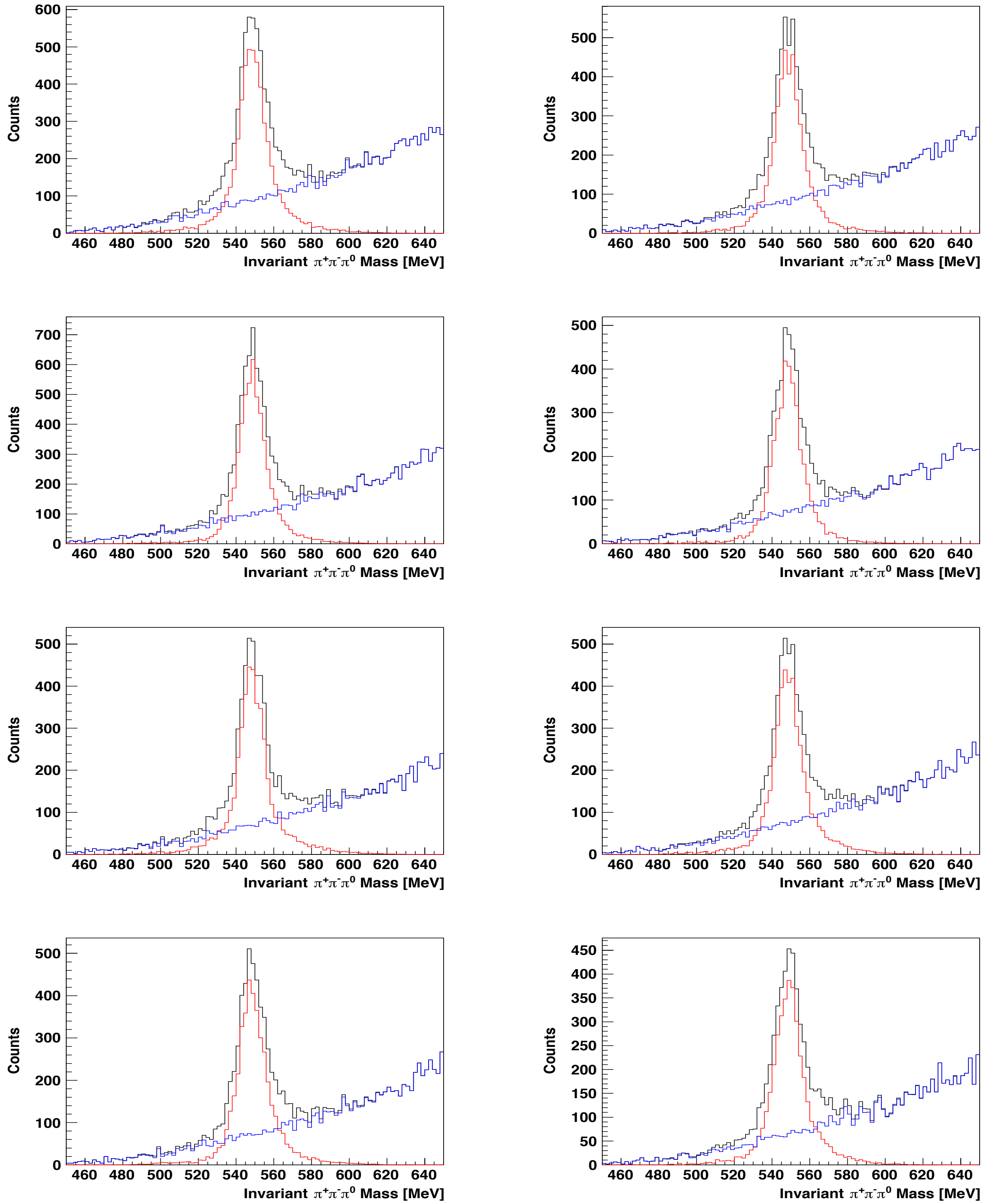

Figure 28: *Invariant $\pi^+\pi^-\pi^0$ distributions for the reaction $\gamma p \to p\eta$. Shown are 10-MeV-wide W bins starting at $W \in [1990, 2000]$ MeV (top left), $W \in [2000, 2010]$ MeV (top right), etc.*

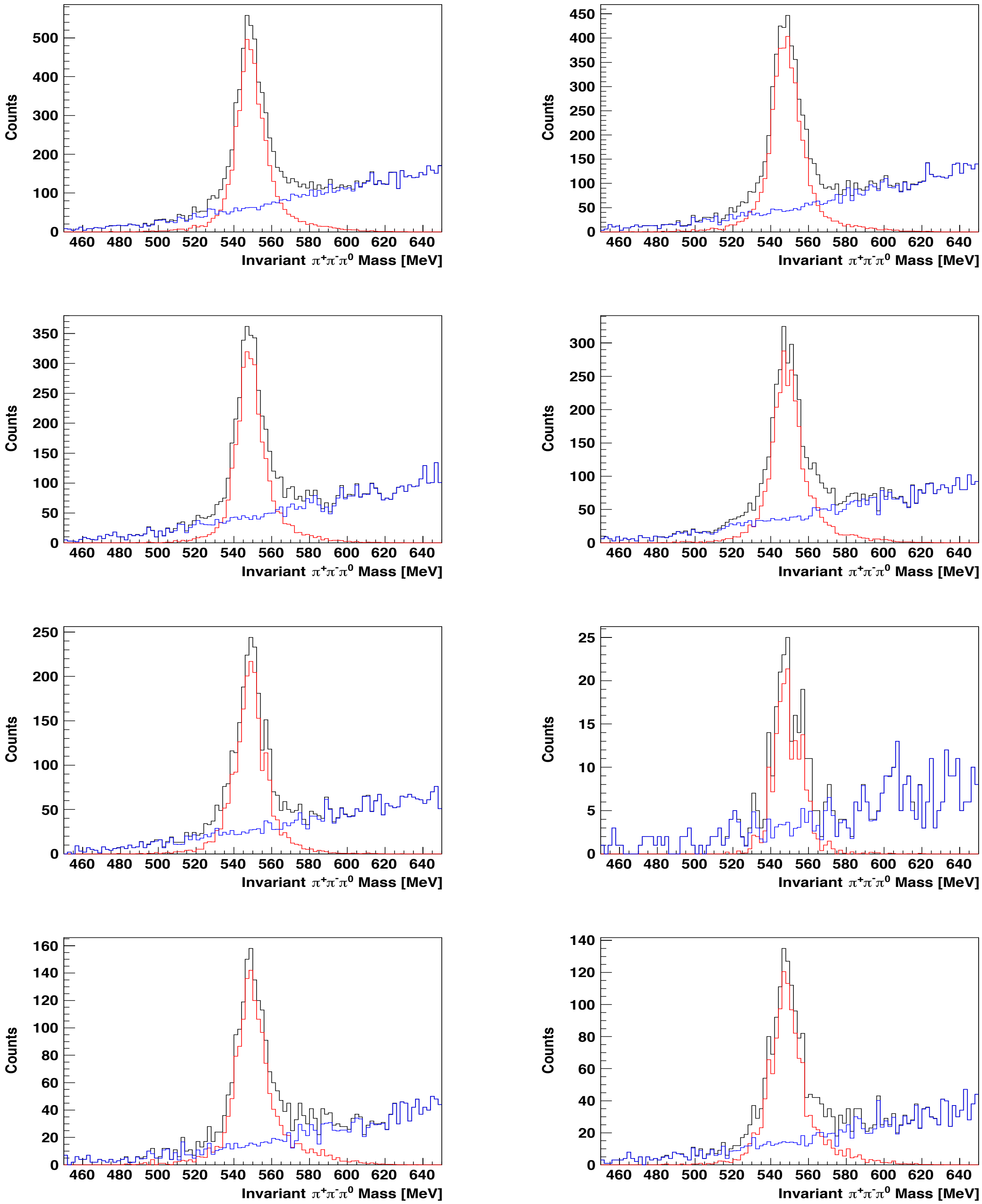

Figure 29: *Invariant* $\pi^+\pi^-\pi^0$ *distributions for the reaction* $\gamma p \to p\eta$*. Shown are 40-MeV-wide* W *bins starting at* $W \in [2360, 2400]$ *MeV (top left),* $W \in [2400, 2440]$ *MeV (top right), etc.*

3.12.4 The Reaction $\gamma p \to K_S^0\,\Sigma^+$

The reconstruction of the $K_S^0\,\Sigma^+$ final state differs from the ω and the η. While the latter two are based directly on the $\pi^+\pi^-\pi^0$ system, the strange K_S is reconstructed from the $\pi^+\pi^-$ system and the remaining π^0 originates from the baryon decay. Since the $K_S \to \pi^+\pi^-$ and the $\Sigma^+ \to p\pi^0$ are highly correlated (associated strangeness production), the reference quantity can either be the invariant $\pi^+\pi^-$ mass or the invariant $p\pi^0$ mass. We determined Q values independently applying both approaches, which serves as a cross check when comparing the cross sections. Table 14 shows the non-reference variables used for the background subtraction in this reaction.

Since the cross section for the reaction $\gamma p \to K^0\,\Sigma^+$ is relatively small, the observed statistics is low and the invariant $\pi^+\pi^-$ mass is dominated by background in the mass region of the K_S (see Fig. 30, top left). Therefore, we considered two mass cuts before we applied the Q-factor method:

1. Strangeness is conserved in electromagnetic and strong interactions. For this reason, the K_S meson is produced together with a Σ^+ baryon (in our analysis). The life time of the Σ^+ ($\tau = (0.8018 \pm 0.0026) \times 10^{-10}$ s) is fairly long since it can only decay weakly. We thus applied a narrow cut of 20 MeV around the Σ^+ mass of 1189.37 MeV [5]. The effect can be seen in Figure 30 (top row). The left side shows the *raw* $\pi^+\pi^-$ distribution of all g12 $\pi^+\pi^-\pi^0$ events in Period 2 (see Table 1), whereas the right side shows the same distribution after the Σ^+ cut. The background is significantly reduced and the K_S peak clearly visible; the $K_S\,\Sigma^+$ statistics is only marginally affected.

2. The dominant reaction contributing to the $p\,\pi^+\pi^-\pi^0$ final state is ω production. The bottom row of Figure 30 shows the invariant $\pi^+\pi^-\pi^0$ mass vs. the corresponding $\pi^+\pi^-$ mass (left side). The vertical band for the ω is clearly visible and moreover, it exhibits a maximum intensity in the vicinity of the K_S in the projection onto the $\pi^+\pi^-$ axis. Therefore, we applied a mass cut to remove contributions from ω production: $m_{\pi^+\pi^-\pi^0} < 752$ MeV and $m_{\pi^+\pi^-\pi^0} > 812$ MeV. The resulting (final) $\pi^+\pi^-$ mass distribution showing the K_S peak is given on the right side. A comparison of Figure 30 (top right) and Figure 30 (bottom right) indicates that only little $K_S\,\Sigma^+$ statistics is lost due to the ω cut.

The two-dimensional distribution also explains the two structures which can be observed in the projection onto the $\pi^+\pi^-$ axis (right side of Figure 30): (1) The peak around 400 MeV is the

Γ_i	Non-Reference Coordinate	Maximum Range Δ_i
Γ_0	incident photon energy E_γ	100 MeV
Γ_1 & Γ_2	$\cos\theta_{\pi^+}$ and ϕ_{π^+} in the $\pi^+\pi^-$ rest frame	2 & 2π
Γ_3	$\cos\Theta^{K_S}_{\rm c.m.}$ in the center-of-mass frame	2
Γ_4	$\phi^{K_S}_{\rm lab}$	2π
Γ_5	$\cos$ (opening angle $\angle\,(p,\,\pi^0)$)	2

Table 14: *The non-reference coordinates Γ_i and their ranges Δ_i.*

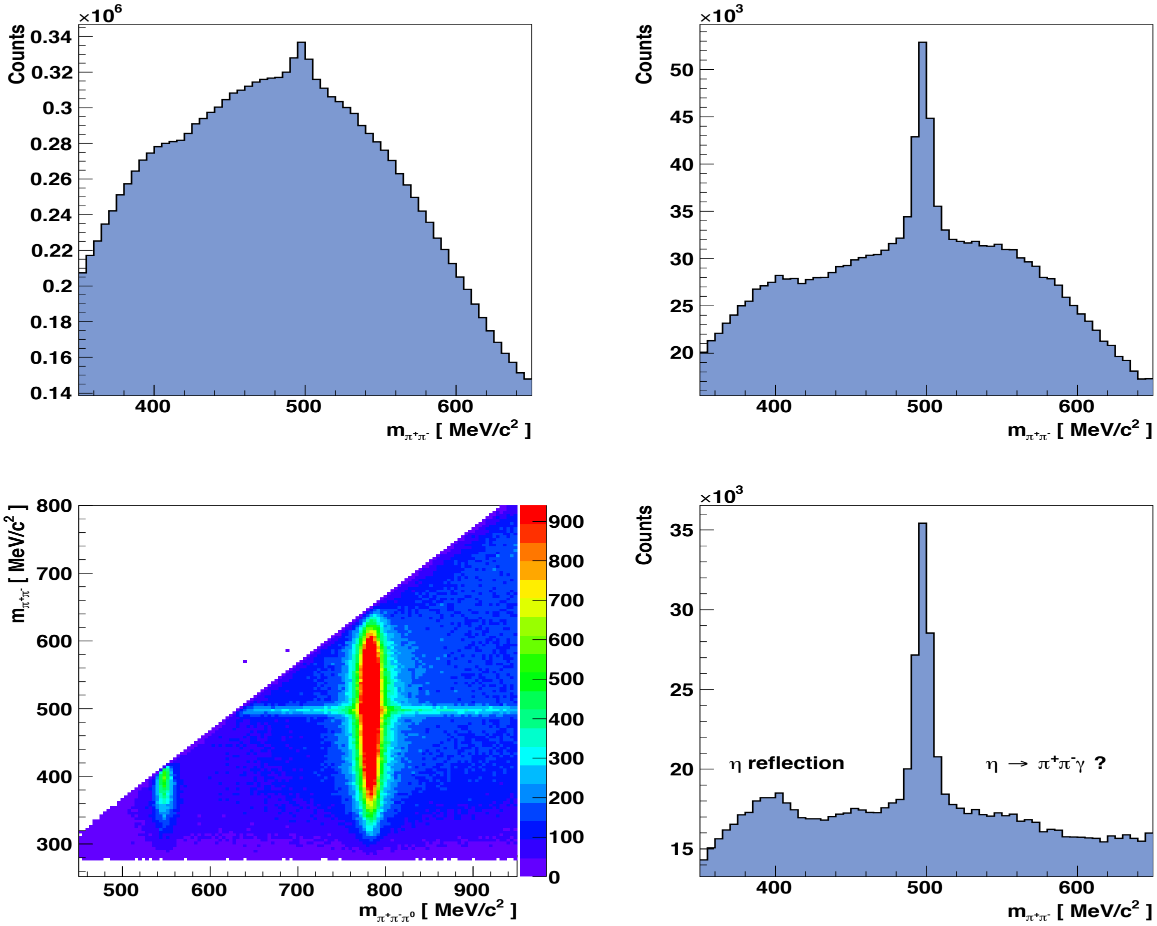

Figure 30: *Top row: Invariant $\pi^+\pi^-$ mass distribution of all g12 $\pi^+\pi^-\pi^0$ events in Period 2 (left) and the same invariant $\pi^+\pi^-$ mass distribution after the Σ^+ cut (right). Bottom row: Invariant $\pi^+\pi^-\pi^0$ mass vs. the corresponding $\pi^+\pi^-$ mass of all g12 $\pi^+\pi^-\pi^0$ events in Period 2 (left) and the same invariant $\pi^+\pi^-$ mass distribution shown in the top row after the ω and the Σ^+ cuts (right).*

reflection of the $\eta \to \pi^+\pi^-\pi^0$ which is cut off at the phase-space boundary, and (2) the enhancement around 550 MeV is most likely based on the η decaying into $\pi^+\pi^-\gamma$.

To subtract the background for the $K_S\,\Sigma^+$ final state, the selected g12-data were divided into data subsets of 100-MeV-wide incident-photon bins. We chose the number of 500 nearest-neighbor events for each signal candidate in the phase space spanned by the non-reference coordinates. The $\pi^+\pi^-$ invariant mass distribution of these 500 events was fitted over the mass range 473 - 523 MeV for the K_S and independently, the $p\pi^0$ mass distribution was fitted over the mass range 1149 - 1229 MeV for the Σ^+ using the unbinned maximum-likelihood technique. Since the K_S decays weakly into $\pi^+\pi^-$ with a mean life τ of about $(8.954 \pm 0.004) \times 10^{-11}$ s [5] (and has thus a narrow natural width), we chose a Gaussian function for the signal pdf and a second-order Chebychev polynomial for the background. Table 15 shows the parameters of the signal and background pdfs and the constraints imposed on them.

		Ref. Coordinate: $\pi^+\pi^-$ Mass		Ref. Coordinate: $p\pi^0$ Mass	
		Initial Value	Fit Range	Initial Value	Fit Range
Gaussian pdf	Mean, μ	497.61 MeV [5]	fixed	1189.37 MeV [5]	fixed
	Width, σ	4.5 MeV	2.0 - 8.0 MeV	4.5 MeV	0.0 - 9.0 MeV
Chebychev pdf	c_0	0.1	-1.5 - 1.5	0.1	-1.5 - 1.5
	c_1	0.1	-1.5 - 1.5	0.1	-1.5 - 1.5

Table 15: *Parameters of the signal & background probability-density functions. A Gaussian was used to describe the signal and a second-order Chebychev polynomial to describe the background.*

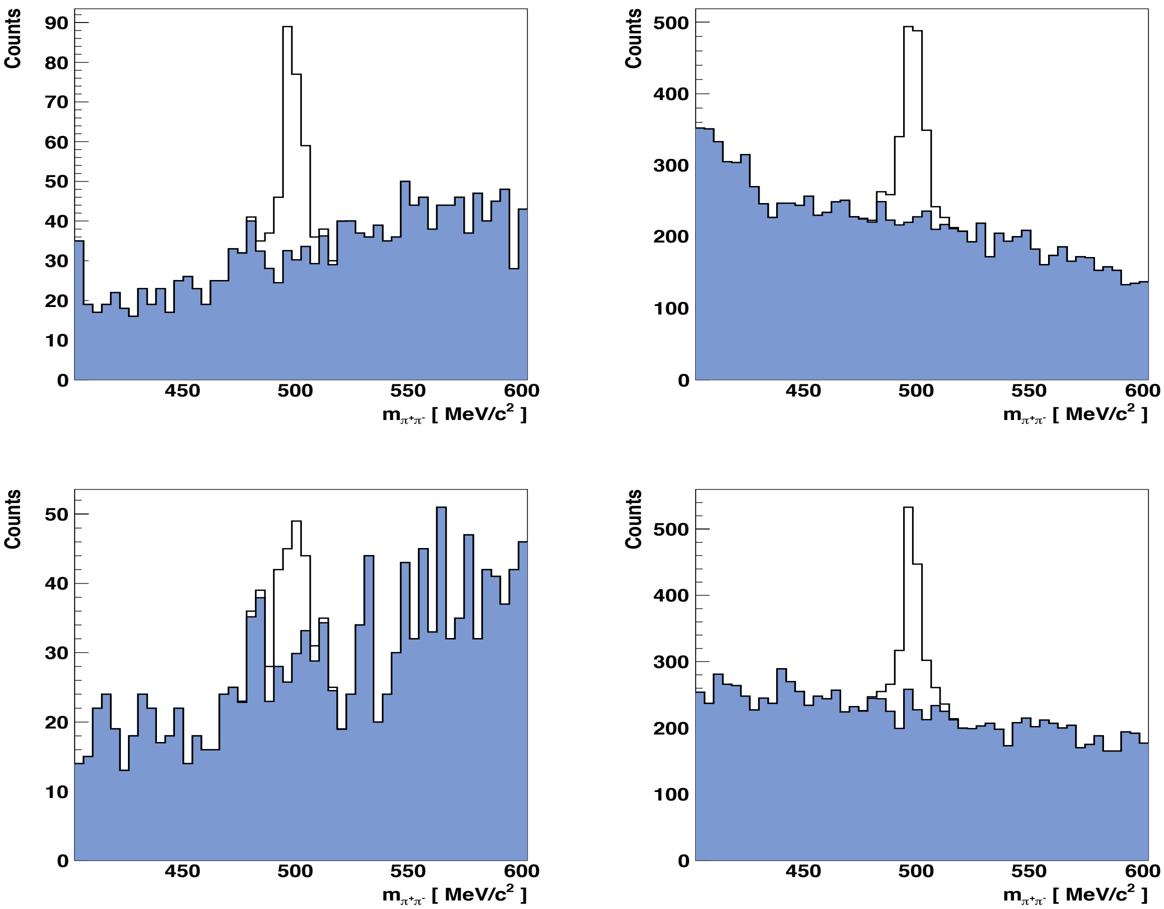

Figure 31: *Examples of* $\pi^+\pi^-$ *distributions for* $\gamma p \to K_S\,\Sigma^+$. *Top row:* $E_\gamma \in [1400,\, 1500]$ *MeV. Bottom row:* $E_\gamma \in [1600,\, 1700]$ *MeV. The left side is for* $-0.6 < \cos\theta^{K_S}_{\mathrm{c.m.}} < -0.4$*, the right side is for* $0.0 < \cos\theta^{K_S}_{\mathrm{c.m.}} < 0.2$ *(according to Table 16).*

Energy Bin	# of Events in E_γ Bin	$-0.6 < \cos\theta^{K_S}_{\text{c.m.}} < -0.4$	$0.0 < \cos\theta^{K_S}_{\text{c.m.}} < 0.2$
0	45918.5	992.7	7014.6
1	248.0	17.5	44.1
2	3253.5	121.2	411.1
3	4024.9	148.0	559.6
4	5624.9	172.1	866.0
5	5684.8	75.8	842.9
6	5483.8	73.7	795.9
7	3989.4	44.0	630.8
8	3304.3	61.3	603.1
9	2249.3	34.8	378.8
10	2305.7	35.2	428.2
11	2078.9	41.8	354.6
12	2022.2	37.5	342.6
13	1463.9	32.8	241.0
14	1086.5	18.9	145.5
15	925.2	14.5	111.3
16	604.4	18.1	86.1
17	828.9	25.5	91.7
18	431.0	9.5	47.9
19	309.0	10.7	33.4

Table 16: *Total number of $\gamma p \to K_S\,\Sigma^+$ events in 100-MeV-wide energy bins (full statistics of Period 2), where Bin 0 denotes the full energy range $1.1 < E_\gamma < 3.0$ GeV, and Bin 1 corresponds to $1.1 < E_\gamma < 1.2$ GeV, etc. The statistics is also given for two randomly-chosen angle bins.*

Figures 32 - 36 show the complete set of invariant $\pi^+\pi^-$ mass distributions (left) and the corresponding $p\pi^0$ mass distributions (right) for 100-MeV-wide incident-photon energy bins in the range $E_\gamma \in [\,1100,\, 3000\,]$ MeV (full statistics used in this analysis). Moreover, Table 16 shows the total number of events (as a sum over all Q values) for all 100-MeV-wide energy bins and for two selected angle bins. Finally, Fig. 31 presents example distributions of E_γ Bins 4 & 5 (shown in Table 16).

Note that a full set of Q values for all events is not necessarily unique. If the Q values are determined for the K_S, then the weighted $\pi^+\pi^-$ mass distribution will show a clear separation of K_S signal and background. However, the $p\pi^0$ mass distribution weighted with the same Q values will still exhibit some background under the Σ^+ signal. The same is true if the Q values are determined for the Σ^+, in which case some background under the K_S will be observed. For a counting experiment like a cross-section measurement, either approach can be used. For an analysis however which requires the full event information, a more sophisticated method would be needed, e.g. a simultaneous fit of both mass distributions.

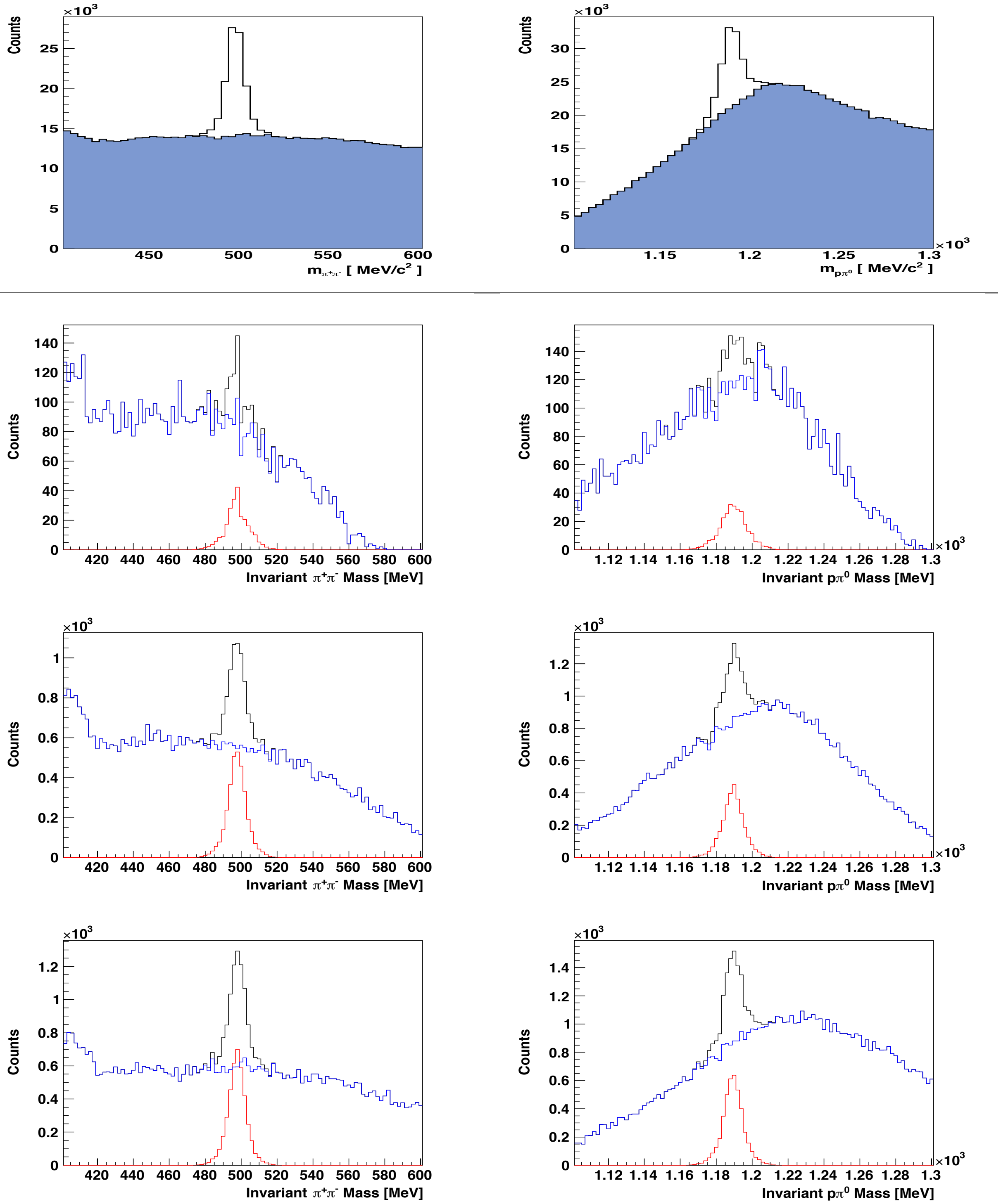

Figure 32: *Invariant $\pi^+\pi^-$ distributions (left column) and the corresponding $p\pi^0$ distributions (right column) for the reaction $\gamma p \to K_S\,\Sigma^+$. Shown are the full statistics (top row) and 100-MeV-wide energy bins starting at $E_\gamma \in [1.1,\,1.2]$ GeV (second row), $E_\gamma \in [1.2,\,1.3]$ GeV (third row), etc.*

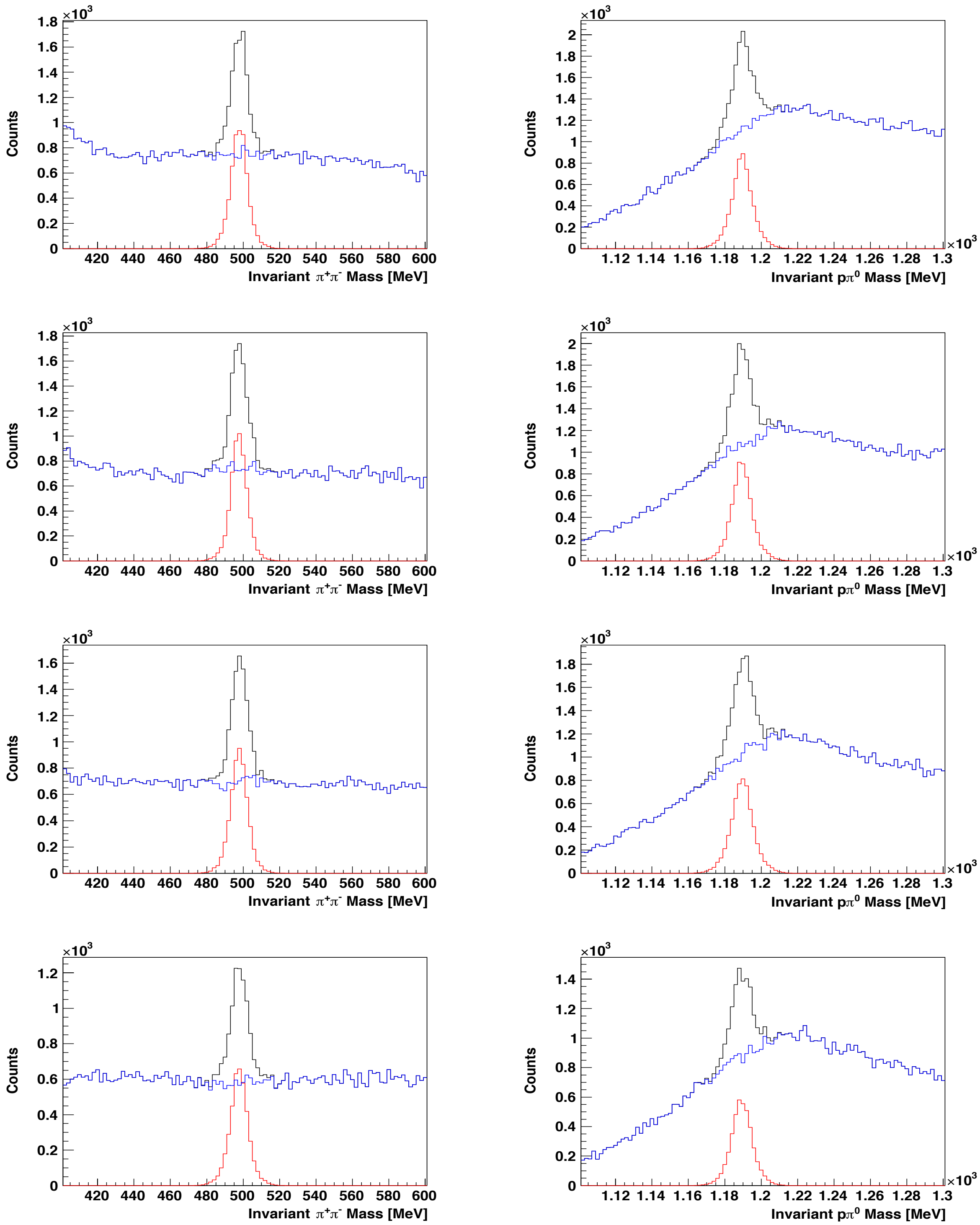

Figure 33: *Invariant* $\pi^+\pi^-$ *distributions (left column) and the corresponding* $p\pi^0$ *distributions (right column) for the reaction* $\gamma p \to K_S\,\Sigma^+$*. Shown are 100-MeV-wide energy bins starting at* $E_\gamma \in [1400,\, 1500]$ *MeV (top row),* $E_\gamma \in [1500,\, 1600]$ *MeV (second row), etc.*

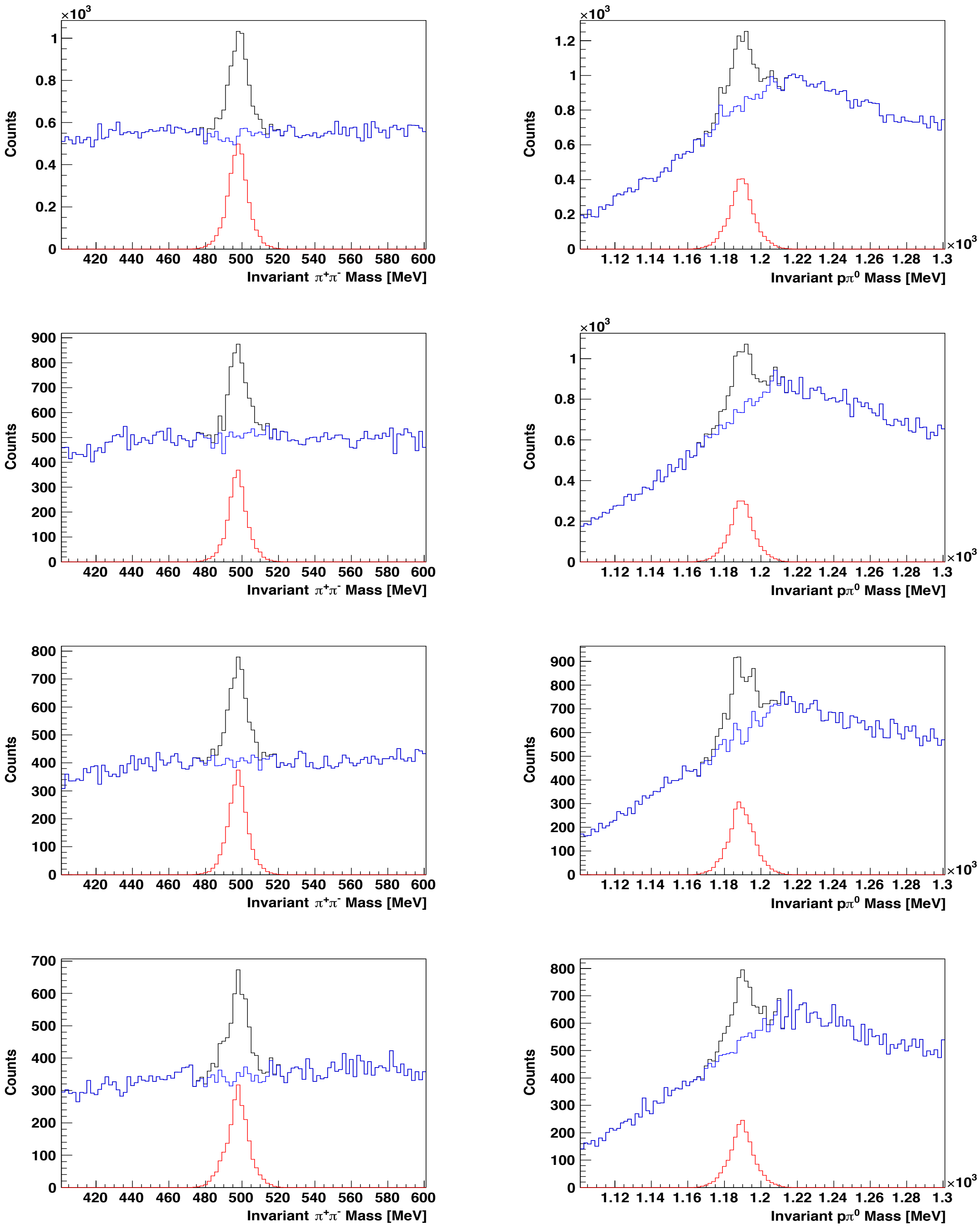

Figure 34: *Invariant $\pi^+\pi^-$ distributions (left column) and the corresponding $p\pi^0$ distributions (right column) for the reaction $\gamma p \to K_S\,\Sigma^+$. Shown are 100-MeV-wide energy bins starting at $E_\gamma \in [1800,\, 1900]$ MeV (top row), $E_\gamma \in [1900,\, 2000]$ MeV (second row), etc.*

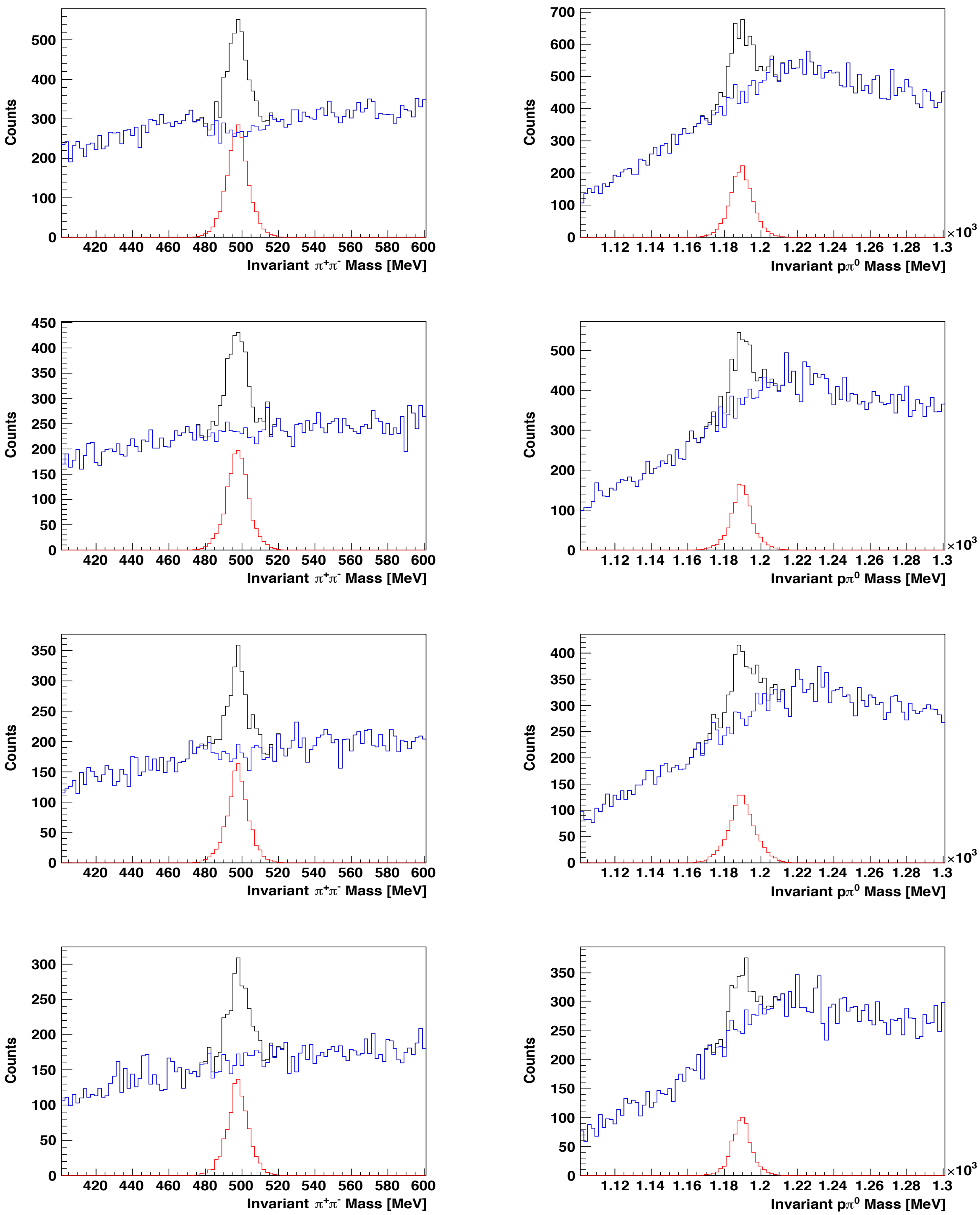

Figure 35: *Invariant* $\pi^+\pi^-$ *distributions (left column) and the corresponding* $p\pi^0$ *distributions (right column) for the reaction* $\gamma p \to K_S\,\Sigma^+$*. Shown are 100-MeV-wide energy bins starting at* $E_\gamma \in [2200, 2300]$ *MeV (top row),* $E_\gamma \in [2300, 2400]$ *MeV (second row), etc.*

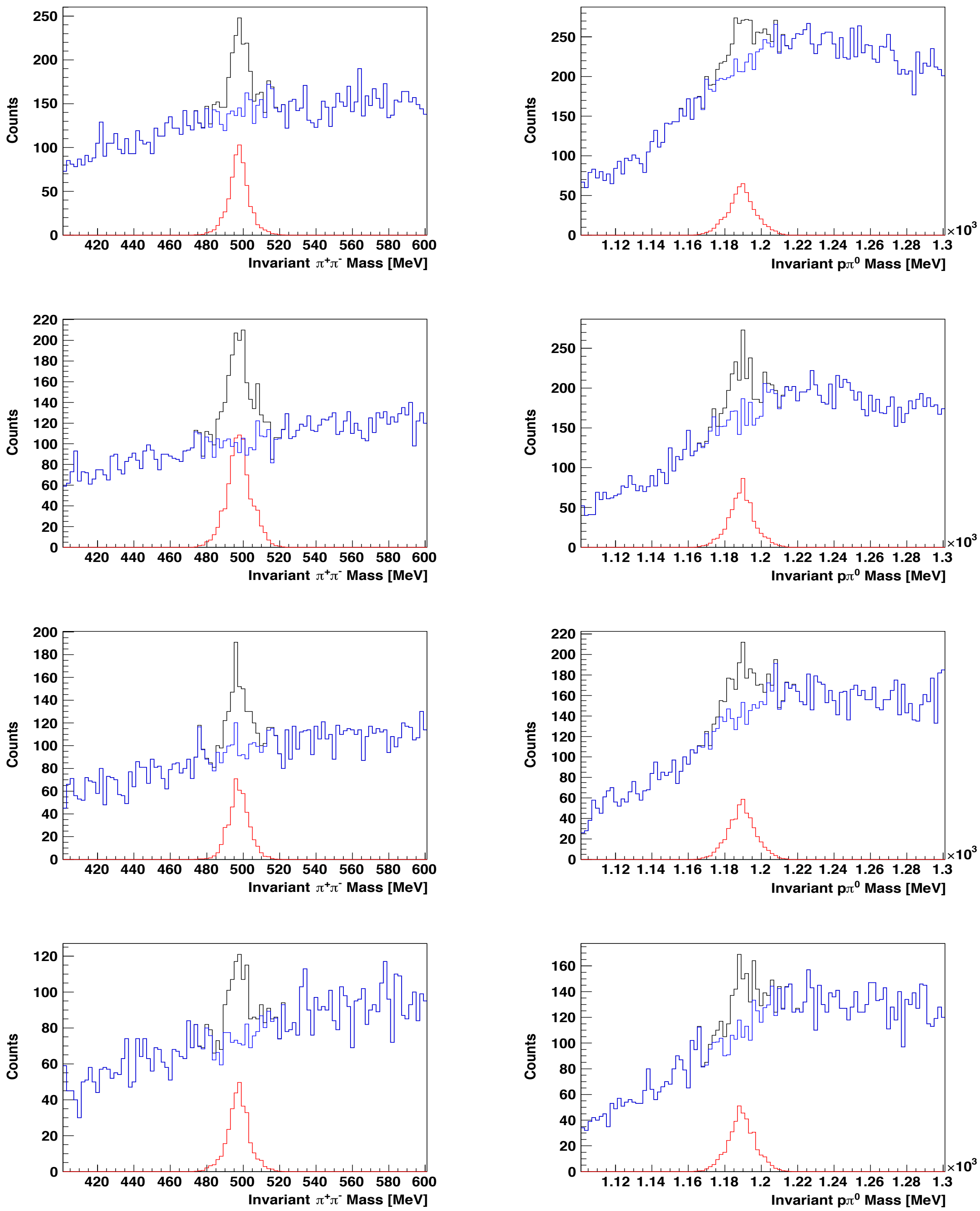

Figure 36: *Invariant* $\pi^+\pi^-$ *distributions (left column) and the corresponding* $p\pi^0$ *distributions (right column) for the reaction* $\gamma p \to K_S\,\Sigma^+$*. Shown are 100-MeV-wide energy bins starting at* $E_\gamma \in [2600, 2700]$ *MeV (top row),* $E_\gamma \in [2700, 2800]$ *MeV (second row), etc.*

4 General Physics Analysis

After all corrections and cuts were applied and signal-background separation was carried out, the extraction of cross sections (and some polarization observables) from the carefully selected events could commence. This chapter presents the methodology used in the extraction of these observables from the experimental data.

4.1 Kinematics and Observables

4.1.1 Binning and Angles in the $\gamma p \to p\,\omega$ Analysis

Summary: We have extracted differential cross sections, $\mathrm{d}\sigma/\mathrm{d}\Omega$ and $\mathrm{d}\sigma/\mathrm{d}t$, for the incident-photon energy range $1.5 < E_\gamma < 5.4$ GeV.

The kinematics of ω photoproduction off the proton could be completely described by two kinematic variables. We chose these variables to be the incident photon energy, E_γ (alternatively W), and the cosine of the polar angle of the ω meson in the center-of-mass frame, $\cos\Theta^{\omega}_{\text{c.m.}}$, where the z-axis was defined along the incoming photon beam (see Figure 37). Alternatively, we also used the Mandelstam variable t and a representation of the differential cross sections in $\mathrm{d}\sigma/\mathrm{d}t$. The data were binned in 50-MeV-wide E_γ bins and covered an energy range from 1500 - 5400 MeV. Note that CLAS had poor acceptance for three-track events in the very forward and backward directions in the center-of-mass frame.

4.1.2 Binning and Angles in the $\gamma p \to p\,\eta$ Analysis

Summary: We have extracted differential cross sections, $\mathrm{d}\sigma/\mathrm{d}\Omega$ and $\mathrm{d}\sigma/\mathrm{d}t$, for the incident-photon energy range $1.1 < E_\gamma < 5.4$ GeV.

The description of the reaction kinematics in $\gamma p \to p\,\eta$ and the kinematic variables used in this analysis were identical to those for the reaction $\gamma p \to p\,\omega$. In Figure 37, the ω can simply be replaced

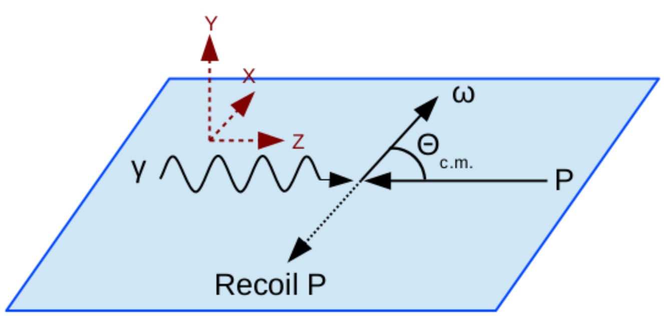

Figure 37: *A diagram describing the kinematics of the reaction $\gamma p \to p\,\omega$. The blue plane represents the center-of-mass production plane composed of the initial photon and the recoil proton. The angle $\Theta_{c.m.}$ denotes the angle between the initial proton and the ω meson in the center-of-mass system. The z-axis is chosen to be along the direction of the incoming photon beam. The y-axis is defined as $\hat{y} = \frac{\hat{p}_{rec}\times\hat{z}}{|\hat{p}_{rec}\times\hat{z}|}$, where $\hat{p}_{rec}$ is a unit vector along the momentum of the recoil proton. The x-axis then lies in the production plane.*

with the η. Both mesons were reconstructed from the $\pi^+\pi^-\pi^0$ system. For the presentation of the differential cross sections, the available statistics allowed us to use 50-MeV-wide E_γ bins in the incident-photon energy.

4.1.3 Binning and Angles in the $\gamma p \to K^0\,\Sigma^+$ Analysis

Summary: We have extracted differential cross sections $\mathrm{d}\sigma/\mathrm{d}\Omega$ for the incident-photon energy range $1.1 < E_\gamma < 3.0$ GeV and the polarization, P, of the Σ^+ hyperon.

The $K^0\,\Sigma^+$ final state is a two-body final state consisting of a meson (M) and a baryon (B), very similar to the previous two reactions (M = ω or η; B = p). For this reason, the kinematics is again represented by the diagram in Figure 37 when the recoil p is replaced with the Σ^+ and the ω is replaced with the K^0. For the cross sections, we have used 100-MeV-wide E_γ bins in the incident-photon energy and 0.2-wide angle bins in $\cos\Theta^{K_S}_{\mathrm{c.m.}}$.

Polarization Observables

The angular distribution of the decay nucleon is given by [13, 14]:

$$W(\Theta_N) \;=\; \frac{1}{2}\,(1\,+\,\alpha\,P\cos(\Theta_N))\,, \tag{18}$$

where the parameter P denotes the hyperon polarization and Θ_N is the decay angle of the nucleon measured with respect to the normal of the production plane of K^0_S and Σ^+ in the Σ^+ rest frame.

4.1.4 Binning and Angles in the $\gamma p \to p\,\pi^+\pi^-$ Analysis

Summary: We have extracted the beam-helicity asymmetry, $\mathbf{I}^{\odot}$.

The kinematics of $\gamma p \to p\,\pi^+\pi^-$ required a selection of five independent kinematic variables. For this analysis, $\cos\Theta^p_{\mathrm{c.m.}}$, a mass ($m_{p\pi^+}$, $m_{p\pi^-}$, or $m_{\pi^+\pi^-}$), the center-of-mass energy, W, as well as θ_{π^+} and ϕ_{π^+} were chosen. The latter two angles denoted the polar and azimuthal angles of the π^+ in the rest frame of the $\pi^+\pi^-$ system. A diagram showing the kinematics of the reaction can be seen in Figure 38. The blue plane represents the center-of-mass production plane composed of the initial photon and the recoil proton, whereas the red plane represents the decay plane formed by two of the final-state particles.

The angle ϕ^* shown in Figure 38 was a kinematic variable unique to a final state containing two pseudoscalar mesons. It described the orientation of the decay plane with respect to the production plane. It was also given by the azimuthal angle of one of the particles from the chosen pair in this pair's rest frame. In our analysis, we chose the π^+ meson (the corresponding azimuthal angle will be denoted as ϕ_{π^+} instead of ϕ^*). The angle ϕ_{π^+} was calculated via two boosts. The first being a boost along the beam axis into the overall center-of-mass frame. The second boost occured along the axis antiparallel to the recoiling proton and resulted in the two-π rest frame, wherein the two final-state pions departed back-to-back. Mathematically, ϕ_{π^+} was uniquely determined by the following expression:

$$\cos\phi_{\pi^+} \;=\; \frac{(\vec{p}\times\vec{a})\,\cdot\,(\vec{b}_2\times\vec{b}_1)}{|\vec{p}\times\vec{a}|\;|\vec{b}_2\times\vec{b}_1|}\,, \tag{19}$$

where $\vec{p}$, $\vec{a}$, $\vec{b}_1$, and $\vec{b}_2$ were the initial-state proton, the recoil proton, the π^+ and π^-, respectively.

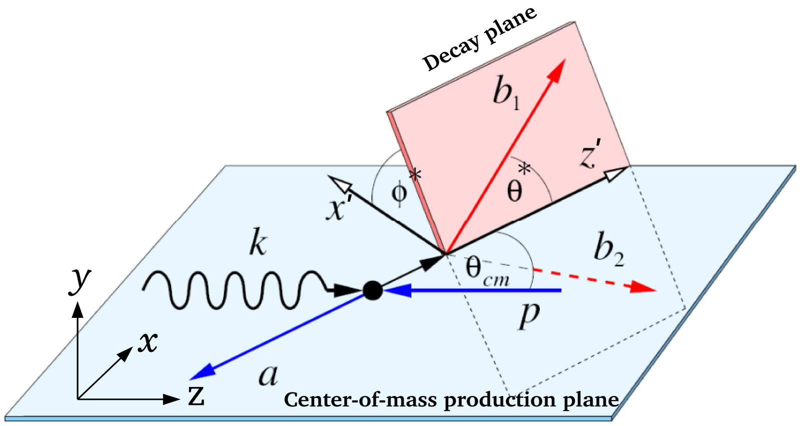

Figure 38: *A diagram describing the kinematics of the reaction $\gamma p \to p\,\pi^+\pi^-$. The blue plane represents the center-of-mass production plane composed of the initial photon and one of the final-state particles, whereas the red plane represents the decay plane formed by the other two final-state particles. a, b_1, and b_2 denote the three particles of the final state. The z-axis is chosen along the direction of the incoming photon beam. The y-axis is defined as $\hat{y} = \frac{\hat{p}_{rec}\times\hat{z}}{|\hat{p}_{rec}\times\hat{z}|}$, where $\hat{p}_{rec}$ is a unit vector along the momentum of one of the final-state particles. If the chosen particle is represented by particle a, then the y-axis will point in the direction as shown in the figure. Moreover, k is the momentum of the initial photon and the particle p denotes the polarized proton in the FROST target. If we assume that particle a is the recoiling proton, then b_1 and b_2 will be the two pions, π^+ and π^-. The angle $\Theta_{c.m.}$ denotes the angle between the initial proton and the particle a in the center-of-mass system. Finally, ϕ^* and θ^* indicate the azimuthal and polar angles of the particle b_1 in the rest frame of b_1 and b_2. In our analysis, we chose π^+ as b_1. Hence, we will use the notations ϕ_{π^+} (θ_{π^+}) instead of ϕ^* (θ^*) in our results.*

The CLAS-g12 data were initially binned for the experimental analysis in two of the five independent kinematic variables [5]. These binning variables were the center-of-mass energy, W, and the azimuthal angle, ϕ_{π^+}. The choice of ϕ_{π^+} was important since the behavior of the polarization observables with respect to this variable has been predicted as either *even* or *odd* [15] and thus, served as a good check for our results. To compare the beam-helicity asymmetry, $\mathbf{I}^{\odot}$, with the results from the CLAS-g1c analysis [16], the center-of-mass energy, W, was divided into 50-MeV wide bins. This resulted in a total of 20 bins in the center-of-mass energy, covering an energy range from 1.225 GeV to 2.225 GeV. For the azimuthal angle, ϕ_{π^+}, 20 bins were used, covering a range from $0 \le \phi_{\pi^+} \le 2\pi$. This represented an improvement over the previous CLAS analysis which used only 11 bins in the same angular range. Thus, we were able to show structures in the observable more clearly. This binning choice resulted in a total of 400 bin combinations per final-state topology.

[5] It is important to note that the binning scheme presented here was chosen only for our experimental analysis and the presentation of the data. A different scheme or even combinations of different kinematic variables will likely be used for the interpretation of the data in a partial wave analysis.

Polarization Observables in $\gamma\, p \to p\, \pi^+ \pi^-$

For $\gamma p \to p\,\pi\pi$, without measuring the polarization of the recoiling nucleon, the general cross section, σ, was given by [15]:

$$\begin{aligned} \sigma \;=\; \sigma_0 \, \{ \, (\, 1 \, + \, \vec{\Lambda}_i \cdot \vec{\mathbf{P}} \,) \\ + \; \delta_{\odot} \, (\mathbf{I}^{\odot} \, + \, \vec{\Lambda}_i \cdot \vec{\mathbf{P}}^{\,\odot} \,) \\ + \; \delta_{l} \, [\, \sin 2\beta \, (\, \mathbf{I}^{\mathbf{s}} \, + \, \vec{\Lambda}_i \cdot \vec{\mathbf{P}}^{\,\mathbf{s}} \,) \, + \, \cos 2\beta \, (\, \mathbf{I}^{\mathbf{c}} \, + \, \vec{\Lambda}_i \cdot \vec{\mathbf{P}}^{\,\mathbf{c}} \,) \,] \, \} \, , \end{aligned} \tag{20}$$

where σ_0 was the unpolarized cross section. $\vec{\Lambda}_i$ denoted the polarization of the initial nucleon and $\delta_{\odot}$ was the degree of circular polarization of the incident-photon beam, while δ_l was the degree of linear polarization. The angle β denoted the angle of inclination between the linearly-polarized photon beam relative to the x-axis in the center-of-mass production plane. It was defined as positive if the x-axis was rotated counter-clockwise from the beam polarization.

Equation 20 contains 15 polarization observables. The beam asymmetries, $\mathbf{I}^{\odot}$, $\mathbf{I}^{\mathbf{s}}$, and $\mathbf{I}^{\mathbf{c}}$ are observables which arise from beam polarization. The observables $\vec{\mathbf{P}}$ (with components $\mathbf{P_x}$, $\mathbf{P_y}$, $\mathbf{P_z}$) describe the target asymmetries which arise if only the target nucleon is polarized, and $\vec{\mathbf{P}}^{\odot}$ as well as $\vec{\mathbf{P}}^{\,s,\,c}$ represent the double-polarization observables.

The reaction rate for $\gamma p \to p\,\pi\pi$, in the case of a circularly-polarized beam incident on an unpolarized target (CLAS-g12 data), reduced to:

$$\sigma \;=\; \sigma_0 \, \{ \, 1 \, + \, \delta_{\odot} \, \mathbf{I}^{\odot} \, \} \, , \tag{21}$$

where $\delta_{\odot}$ was again the degree of circular polarization of the incident-photon beam.

4.2 Extraction of Cross Sections

The differential cross sections for all reactions were determined according to

$$\frac{\mathrm{d}\sigma}{\mathrm{d}\Omega} \;=\; \frac{N_{\,\mathrm{reaction}}}{A_{\,\mathrm{reaction}}} \, \frac{1}{N_{\gamma} \, \rho_{\,\mathrm{target}}} \, \frac{1}{\Delta\Omega} \, \frac{1}{BR} \, , \tag{22}$$

where

$\rho_{\,\mathrm{target}}$:	target area density
$N_{\,\mathrm{reaction}}$:	number of reconstructed data events in an (E_γ, $\cos\theta_{\mathrm{c.m.}}$) bin
N_γ :	number of photons in an E_γ bin (photon flux)
$A_{\,\mathrm{reaction}}$:	acceptance in an (E_γ, $\cos\theta_{\mathrm{c.m.}}$) bin
$\Delta\Omega$:	solid-angle interval $\Delta\Omega = 2\pi \, \Delta\cos(\theta_{\mathrm{c.m.}})$
BR :	decay branching fraction.

Target Cross Sectional Area

The target area density, i.e. the number of atoms in the target material per cross-sectional area (orthogonal to the photon beam), is given by

$$\rho_{\,\text{target}} \;=\; 2\,\frac{\rho(\text{H}_2)\,N_A\,L}{M_{\,\text{mol}}\,(\text{H}_2)}\,, \tag{23}$$

where $\rho(\text{H}_2) = 0.0711 \pm 1.75\,\cdot\,10^{-5}$ g/cm^3 [4] is the density and $M_{\,\text{mol}} = 2.01588$ g/mol the molar mass of liquid H_2. $N_A = 6.022 \cdot 10^{23}$ mol^{-1} is the Avogadro number and $L = 40.0$ cm the length of the target cell. The factor of two accounts for the molecular composition of hydrogen (H_2).
We have used a value of $\rho_{\,\text{target}} = 16.992\,\cdot\,10^{-7}\mu\text{b}^{-1}$ for all cross sections.

Solid-Angle Interval

An object's solid angle in steradians is equal to the area of the segment of a unit sphere, centered at the angle's vertex, that the object covers. A solid angle in steradians equals the area of a segment of a unit sphere in the same way a planar angle in radians equals the length of an arc of a unit circle. The solid angle of a sphere measured from any point in its interior is 4π sr. In spherical coordinates:

$$\Omega \;=\; \iint_S \sin\theta\,\mathrm{d}\theta\,\mathrm{d}\phi \;=\; 2\cdot 2\pi \;=\; 4\pi\,, \tag{24}$$

where 2π originates from integrating over $\mathrm{d}\phi$ and the factor of 2 from integrating over $\sin\theta\,\mathrm{d}\theta$. Since the differential cross sections are integrated over $\phi_{\,\text{lab}}$ but are binned in $\cos\theta_{\text{c.m.}}$, we used $\Delta\Omega = 2\pi\,\Delta\!\cos\,(\theta_{\text{c.m.}})$ in Equation 22 and $\Delta\!\cos\,(\theta_{\text{c.m.}}) = 2\;/\;$(# of angle bins):

- $\Delta\Omega \;=\; 2\pi\,\cdot\,2\,/\,20 \;=\; 0.6283$ (for η, ω production).
- $\Delta\Omega \;=\; 2\pi\,\cdot\,2\,/\,10 \;=\; 1.2567$ (for $K^0\,\Sigma^+$ production).

Branching Fractions

We have used the following values [5]:

$p\,\omega$: Fraction $\Gamma_i\,/\,\Gamma = (89.2 \pm 0.7)\,\%$ ($\omega\,\rightarrow\,\pi^+\pi^-\pi^0$), i.e. $BR\,=\,0.892$.

$p\,\eta$: Fraction $\Gamma_i\,/\,\Gamma = (22.92 \pm 0.28)\,\%$ ($\eta\,\rightarrow\,\pi^+\pi^-\pi^0$), i.e. $BR\,=\,0.2292$.

$K^0\,\Sigma^+$: Fraction $\Gamma_i\,/\,\Gamma = (69.20 \pm 0.05)\,\%$ ($K_S\,\rightarrow\,\pi^+\pi^-$) as well as
$\Gamma_i\,/\,\Gamma = (51.57 \pm 0.30)\,\%$ ($\Sigma^+\,\rightarrow p\,\pi^0$), i.e. $BR\,=\,0.5\,\cdot\,0.5157\,\cdot\,0.6920\,=\,0.1784$.

The factor of 0.5 for $K^0\,\Sigma^+$ accounts for the mixture of K^0 being $50\,\%$ K_S and $50\,\%$ K_L.

Photon Flux

For the absolute normalization, we have used the standard CLAS GFLUX package which was originally developed by James Ball and Eugene Pasyuk []. A detailed description on how to use GFLUX for the CLAS-g12 experiment can be found in Ref. [4]. Table 17 gives the actual numbers we have used for all three cross sections: $\gamma p \rightarrow p\,\omega$, $\gamma p \rightarrow p\,\eta$, $\gamma p \rightarrow K_S\,\Sigma^+$.

Absolute Normalziation: NGRF Correction

CEBAF delivers electrons in bunches separated by 2 ns. Increasing the current in the accelerator increases the number of electrons in each bunch. Most of the g12 data were recorded at high curents of 60 - 65 nA, which correspond to a photon flux of about $5 \times 10^8 \, \gamma$ per second. The high current of the g12 experiment led to some ambiguity in selecting the correct photon for some events. About 14.26 % of all events had more than one incident photon that passed the *coincidence-time* cut or $|\Delta \, t_{\mathrm{TGPB}}| < 1$ ns (Section **??**).

We applied a cut of 14.26 % events which have more than one photon candidate within *coincidence time* cut. Since the Monte carlo events do not simulate the photon, we then correct the photon flux by 85.74 % or multiply the signal yield by 1.17.

E_γ [GeV]	Photon Flux	E_γ [GeV]	Photon Flux	E_γ [GeV]	Photon Flux
		2.50 - 2.55	302735185984.0	4.00 - 4.05	140606283698.0
		2.55 - 2.60	259964248500.0	4.05 - 4.10	149223684420.0
1.10 - 1.15	4337260656.3	2.60 - 2.65	254886921499.0	4.10 - 4.15	140423638221.0
1.15 - 1.20	337833236168.0	2.65 - 2.70	259744931434.0	4.15 - 4.20	167418318127.0
1.20 - 1.25	574495330532.0	2.70 - 2.75	224963728409.0	4.20 - 4.25	152175155236.0
1.25 - 1.30	496274905472.0	2.75 - 2.80	203753682420.0	4.25 - 4.30	160068141472.0
1.30 - 1.35	485238697908.0	2.80 - 2.85	242060106771.0	4.30 - 4.35	128465044374.0
1.35 - 1.40	349080941294.0	2.85 - 2.90	238390370808.0	4.35 - 4.40	90453090800.2
1.40 - 1.45	508526554976.0	2.90 - 2.95	231067058790.0	4.40 - 4.45	64699027048.5
1.45 - 1.50	497502848514.0	2.95 - 3.00	201595160599.0	4.45 - 4.50	158368725065.0
1.50 - 1.55	460473338930.0	3.00 - 3.05	233214036559.0	4.50 - 4.55	158892370026.0
1.55 - 1.60	399150479194.0	3.05 - 3.10	184728636406.0	4.55 - 4.60	136955763789.0
1.60 - 1.65	446872653860.0	3.10 - 3.15	213765127885.0	4.60 - 4.65	137198213594.0
1.65 - 1.70	395792605738.0	3.15 - 3.20	164173778322.0	4.65 - 4.70	139594283568.0
1.70 - 1.75	415054272952.0	3.20 - 3.25	199344803385.0	4.70 - 4.75	142168709686.0
1.75 - 1.80	408411797706.0	3.25 - 3.30	207673397085.0	4.75 - 4.80	102093637851.0
1.80 - 1.85	397650894046.0	3.30 - 3.35	178704643413.0	4.80 - 4.85	123160541637.0
1.85 - 1.90	345708998882.0	3.35 - 3.40	196705358312.0	4.85 - 4.90	147419199730.0
1.90 - 1.95	365121651368.0	3.40 - 3.45	191004264574.0	4.90 - 4.95	155283230557.0
1.95 - 2.00	304992117538.0	3.45 - 3.50	179980234595.0	4.95 - 5.00	120930458861.0
2.00 - 2.05	336131767024.0	3.50 - 3.55	77594303520.0	5.00 - 5.05	116822823306.0
2.05 - 2.10	347415226190.0	3.55 - 3.60	284139117094.0	5.05 - 5.10	150662097632.0
2.10 - 2.15	291012042438.0	3.60 - 3.65	186509696181.0	5.10 - 5.15	139170116274.0
2.15 - 2.20	329423974509.0	3.65 - 3.70	155345103910.0	5.15 - 5.20	129656508095.0
2.20 - 2.25	349551671915.0	3.70 - 3.75	159517908396.0	5.20 - 5.25	137811011294.0
2.25 - 2.30	260462654486.0	3.75 - 3.80	160555585107.0	5.25 - 5.30	116376757558.0
2.30 - 2.35	306607804116.0	3.80 - 3.85	170460273002.0	5.30 - 5.35	135718523976.0
2.35 - 2.40	289476321935.0	3.85 - 3.90	162365775438.0	5.35 - 5.40	125968316090.0
2.40 - 2.45	256426694871.0	3.90 - 3.95	164569658388.0	5.40 - 5.45	134541705938.0
2.45 - 2.50	241361136501.0	3.95 - 4.00	173623146606.0	5.40 - 5.45	134541705938.0

Table 17: Total g12 photon flux for 50-MeV-wide energy bins for the run range 56521 - 56664.

4.3 Extraction of the Hyperon Polarization in $\gamma p \to K^0 \Sigma^+$

4.4 Extraction of the Beam-Helicity Asymmetry in $\gamma p \to p \pi^+ \pi^-$

Data with Azimuthal Symmetry in the Lab Frame

Data with an unpolarized- or a circularly-polarized beam in combination with an unpolarized- or a longitudinally-polarized target are isotropic in the lab azimuthal angle since the polarization(s) lie along the z-axis in the lab frame. Hence, the angular distribution in the lab frame of any final-state particle will be flat after an acceptance correction. In such cases, the asymmetry in any kinematic bin between the number of events with orthogonal polarization settings is just a number (instead of a function of the lab azimuthal angle). The polarization observables are then easily extracted from these measured asymmetries.

In the case of the beam-helicity asymmetry, $\mathbf{I}^{\odot}$, the data consist of two subsets based on opposite beam helicity, denoted by $\rightarrow$ and $\leftarrow$, where $\rightarrow$ ($\leftarrow$) denotes that the helicity is parallel (antiparallel) to the beam axis. Since the beam helicity flips at a large rate, the flux, Φ, and the acceptance, ϵ, are the same for both subsets. For the same reason, the degree of beam polarization for the two helicity states can be considered the same and is denoted by $\delta_{\odot}$. Then, in any kinematic bin, the number of $\rightarrow$ events and $\leftarrow$ events can be related to $\mathbf{I}^{\odot}$ using Equation 21. The numbers $N_{\rightarrow}$ and $N_{\leftarrow}$ are given by:

$$\begin{aligned} N_{\rightarrow} &= F\, C\, \epsilon\, \sigma_0\, (\, 1 \,+\, \delta_{\odot}\, \mathrm{I}^{\odot}\,)\,, \\ N_{\leftarrow} &= F\, C\, \epsilon\, \sigma_0\, (\, 1 \,-\, \delta_{\odot}\, \mathrm{I}^{\odot}\,)\,, \end{aligned} \tag{25}$$

where $\delta_{\odot}$ denotes the degree of circular-beam polarization. The asymmetry, A, between the two numbers in a kinematic bin is given by:

$$A \,=\, \frac{N_{\rightarrow} \,-\, N_{\leftarrow}}{N_{\rightarrow} \,+\, N_{\leftarrow}} \,=\, \delta_{\odot}\, \mathrm{I}^{\odot}\,. \tag{26}$$

Hence, the beam-helicity observable can be extracted from the asymmetry:

$$\mathrm{I}^{\odot} \,=\, \frac{A}{\delta_{\odot}}\,. \tag{27}$$

If each event is assigned a weight, w_i (a Q value, for instance), then the effective number of signal events for the two beam-helicity states will be given by:

$$N'_{\rightarrow} \,=\, \sum_{i=1}^{N^{\rightarrow}} w_i\,, \qquad N'_{\leftarrow} \,=\, \sum_{i=1}^{N^{\leftarrow}} w_i\,. \tag{28}$$

The asymmetry is then formed from these effective counts:

$$A \,=\, \frac{N'_{\rightarrow} \,-\, N'_{\leftarrow}}{N'_{\rightarrow} \,+\, N'_{\leftarrow}}\,, \tag{29}$$

and $\mathbf{I}^{\odot}$ is obtained using Equation 27.

5 Systematic Errors

5.1 Contribution from the Q-Factor Method

Consider a *simple* counting experiment, for example in g12 where circularly-polarized photons were incident on unpolarized protons. It has been shown earlier in Equation **??** that:

$$\mathbf{I}^{\odot} \;=\; \frac{1}{\bar{\delta}_{\odot}} \left(\frac{N_{\rightarrow} \,-\, N_{\leftarrow}}{N_{\rightarrow} \,+\, N_{\leftarrow}} \right) \;=\; \frac{A}{\bar{\delta}_{\odot}} \;,$$

where $N_{\rightarrow}$ and $N_{\leftarrow}$ were the total number of events with positive and negative beam helicities in any chosen kinematic bin, respectively. The uncertainty in the Q value of each event only affected the counts, and not the average degree of beam polarization. From reference [17], we know that the net contribution of the individual Q-value errors to the total error, σ_N, is given by:

$$\sigma_N^2 \;=\; \sum_i^N \sum_j^N \left(\sigma_{Q_i}\, \rho_{ij}\, \sigma_{Q_j} \right) , \tag{30}$$

where σ_{Q_i} is the error in the Q value of the i^{th} event, N is the total number of events and ρ_{ij} is the correlation between the i^{th} and the j^{th} event (which is equal to the ratio of the number of common nearest neighbors between the two events to the total number of nearest neighbors). Depending on the analysis, it is often more convenient to assume that all events are 100 % correlated and to over-estimate the errors than to calculate the actual correlations (ρ_{ij}) since it can be very time consuming. In our g12 analysis, we chose to find the actual correlations because we found that σ_N was significantly over- (under-)estimated when 100 % (0 %) correlation between events was assumed. For example, in one particular kinematic bin, it was observed that σ_N/N was 44 % when the events were assumed to be 100 % correlated, 3.6 % when the events were assumed to be completely uncorrelated, but 13.4 % when the actual correlations were determined.

From standard error propagation, it was clear that if $\mathbf{I}^{\odot}$ is rewritten as $\mathbf{I}^{\odot} \,=\, f(N_{\rightarrow}, N_{\leftarrow})$ then:

$$\begin{aligned} \sigma_{\mathbf{I}^{\odot}} \;&=\; \sqrt{ \left(\frac{\partial f}{\partial N_{\rightarrow}} \right)^2 \sigma_{N_{\rightarrow}}^2 \,+\, \left(\frac{\partial f}{\partial N_{\leftarrow}} \right)^2 \sigma_{N_{\leftarrow}}^2 } \\ &=\; \frac{2}{\bar{\delta}_{\odot}(N_{\rightarrow} \,+\, N_{\leftarrow})^2} \sqrt{ N_{\leftarrow}^2\, \sigma_{N_{\rightarrow}}^2 \,+\, N_{\rightarrow}^2\, \sigma_{N_{\leftarrow}}^2 } \;\; . \end{aligned} \tag{31}$$

If $\sigma_{N_{\rightarrow}} \,=\, \sigma_{N_{\leftarrow}} \,=\, \sigma_N$, the above equation simplified to:

$$\sigma_{\mathbf{I}^{\odot}} \;=\; \frac{2\, \sigma_N}{\bar{\delta}_{\odot}\, (N_{\rightarrow} \,+\, N_{\leftarrow})} \sqrt{ \frac{N_{\rightarrow}^2 \,+\, N_{\leftarrow}^2}{(N_{\rightarrow} \,+\, N_{\leftarrow})^2} } \;\; . \tag{32}$$

Therefore, $\sigma_{N_{\rightarrow}}$ and $\sigma_{N_{\leftarrow}}$ could be found by using Equation 30 and substituting them into Equation 31 then yielded $\sigma_{\mathbf{I}^{\odot}}$. Similarly, one could follow the method outlined above to analytically find the contribution of the Q-factor method to the total systematic uncertainty in any other observable associated with a simple counting experiment (cross section measurements, for instance).

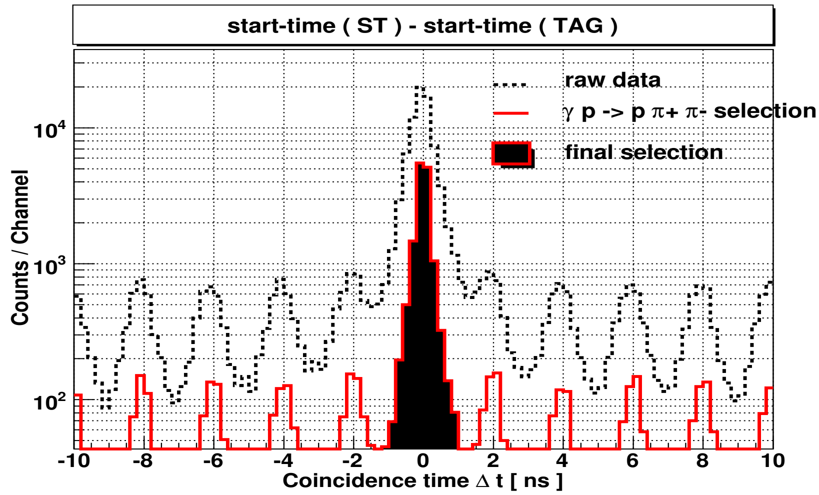

Figure 39: *Coincidence-time distributions of tagged photons for the raw data (dotted histogram) and after applying all* $\gamma p \to p\,\pi^+\pi^-$ *selection cuts (solid histogram). Events of the center bins filled in black indicate the candidates of the final selection. The fraction of remaining accidental photons in the central bucket was at most* 2.5 %.

5.2 Contribution from the Beam Polarization

The beam-helicity asymmetry (in a simple counting experiment) was inversely proportional to the average degree of beam polarization. This relation has been shown for the observable for the observable $\mathbf{I}^{\odot}$ in the $\pi^+\pi^-$ reaction (see Equation **??**). Hence, from error propagation it was clear that any error in the determination of the average beam polarization led to the same percentage error in the polarization observable.

5.3 Contribution from the Beam-Charge Asymmetry

Section 3.11.3 discussed the beam-charge asymmetry in detail. Since they were small ($<$ 0.003 in FROST-g9a and $<$ 0.2 % in FROST-g9b), their effect on the observables was considered negligible.

5.4 Contribution from the Accidental Photons

In Section 3.3.1 we explained how initial photons were selected. Even after following the full selection procedure, some accidental photons remained. The fraction could be estimated from a comparison in the yields between the central peak with the neighboring beam buckets in the coincidence-time distribution. For example, the fraction was at most 2.5 % in g12 (see Figure 39). These accidentals led to an over-estimation in the photon flux by the same factor in all data sets. Therefore, in counting experiments, the accidentals did not affect the polarization observables since the factor canceled out in the asymmetry of counts.

6 Final Results

A Beam Charge Asymmetry

Table **??** in Section 3.11.3 shows the observed beam-charge asymmetry in the g9a data sets. The yields for the positive and negative helicity states, $Y^{\pm}$, in the reaction $\gamma p \to p\,\pi^+\pi^-$ were given by:

$$Y^{\pm} \;=\; \alpha^{\pm}\,N\,, \tag{33}$$

where N was the total number of events in a particular g9a data set and the parameters $\alpha^{\pm}$ were defined in Equation 14. We could then relate the event yields to the beam-helicity asymmetry:

$$\begin{aligned}
Y^{+} \;&=\; \alpha^{+}\,(N^{\Rightarrow}_{\rightarrow} \,+\, C\,N^{\Leftarrow}_{\rightarrow}) \,\sim\, \alpha^{+}\,\Phi\left(1\,+\,\frac{\bar{\Lambda}^{\Rightarrow}}{\bar{\Lambda}^{\Leftarrow}}\right)(1\,+\,\bar{\delta}_{\odot}\,\mathbf{I}^{\odot})\,,\\
Y^{-} \;&=\; \alpha^{-}\,(N^{\Rightarrow}_{\leftarrow} \,+\, C\,N^{\Leftarrow}_{\leftarrow}) \,\sim\, \alpha^{-}\,\Phi\left(1\,+\,\frac{\bar{\Lambda}^{\Rightarrow}}{\bar{\Lambda}^{\Leftarrow}}\right)(1\,-\,\bar{\delta}_{\odot}\,\mathbf{I}^{\odot})\,,
\end{aligned} \tag{34}$$

where $\Phi = \Phi^{\Rightarrow}$ denoted the flux of the first data set, $\bar{\delta}_{\odot}$ the degree of (circular) beam polarization and the normalization factor C included the different degrees of target polarization, $\bar{\Lambda}^{\Leftarrow}$ and $\bar{\Lambda}^{\Rightarrow}$, and photon fluxes, $\Phi^{\Leftarrow}$ and $\Phi^{\Rightarrow}$:

$$C \;=\; \frac{\bar{\Lambda}^{\Rightarrow}\,\Phi^{\Rightarrow}}{\bar{\Lambda}^{\Leftarrow}\,\Phi^{\Leftarrow}}\;. \tag{35}$$

The (beam) asymmetry could then be calculated by using the *corrected* number of events for helicity plus and minus (taking into account the beam-charge asymmetry):

$$\begin{aligned}
A^{\mathrm{beam}} \;&=\; \frac{Y^{+}\,-\,Y^{-}}{Y^{+}\,+\,Y^{-}}\\
&=\; \frac{\alpha^{+}\left(N^{\Rightarrow}_{\rightarrow}\,+\,C\,N^{\Leftarrow}_{\rightarrow}\right)\,-\,\alpha^{-}\left(N^{\Rightarrow}_{\leftarrow}\,+\,C\,N^{\Leftarrow}_{\leftarrow}\right)}{\alpha^{+}\left(N^{\Rightarrow}_{\rightarrow}\,+\,C\,N^{\Leftarrow}_{\rightarrow}\right)\,+\,\alpha^{-}\left(N^{\Rightarrow}_{\leftarrow}\,+\,C\,N^{\Leftarrow}_{\leftarrow}\right)}\\
&=\; \frac{\alpha^{+}\,(1\,+\,\bar{\delta}_{\odot}\,\mathbf{I}^{\odot})\,-\,\alpha^{-}\,(1\,-\,\bar{\delta}_{\odot}\,\mathbf{I}^{\odot})}{\alpha^{+}\,(1\,+\,\bar{\delta}_{\odot}\,\mathbf{I}^{\odot})\,+\,\alpha^{-}\,(1\,-\,\bar{\delta}_{\odot}\,\mathbf{I}^{\odot})}\\
&=\; \frac{(\alpha^{+}\,-\,\alpha^{-})\,+\,(\alpha^{+}\,+\,\alpha^{-})\,\bar{\delta}_{\odot}\,\mathbf{I}^{\odot}}{(\alpha^{+}\,+\,\alpha^{-})\,+\,(\alpha^{+}\,-\,\alpha^{-})\,\bar{\delta}_{\odot}\,\mathbf{I}^{\odot}}\;.
\end{aligned} \tag{36}$$

The polarization observable $\mathbf{I}^{\odot}$ was finally given by (in terms of the (beam) asymmetry):

$$\begin{aligned}
\mathbf{I}^{\odot} \;&=\; \frac{1}{\bar{\delta}_{\odot}}\,\frac{A^{\mathrm{beam}}\,(\alpha^{+}\,+\,\alpha^{-})\,-\,(\alpha^{+}\,-\,\alpha^{-})}{(\alpha^{+}\,+\,\alpha^{-})\,-\,A^{\mathrm{beam}}\,(\alpha^{+}\,-\,\alpha^{-})}\\
&=\; \frac{1}{\bar{\delta}_{\odot}}\left(\frac{A^{\mathrm{beam}}\,-\,\bar{a}_c}{1\,-\,A^{\mathrm{beam}}\,\bar{a}_c}\right),
\end{aligned} \tag{37}$$

where $\bar{a}_c = |\alpha^{+} - \alpha^{-}|$ was the beam-charge asymmetry defined in Section 3.11.3.

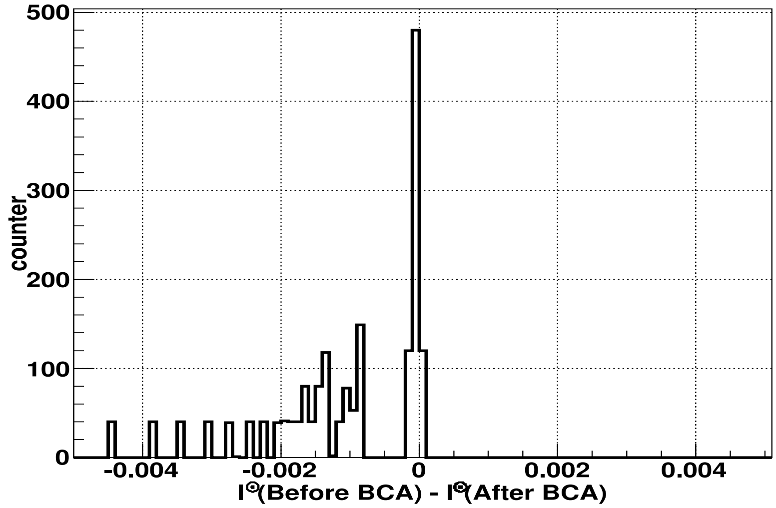

Figure 40: *Comparison between the polarization observable* $\mathbf{I}^{\odot}$ *before and after applying the correction for beam-charge asymmetry.*

We compared the polarization observable $\mathbf{I}^{\odot}$ without considering corrections for the beam-charge asymmetry to the results of Equation 37 using values for $\bar{a}_c$ from Table **??**. Figure 40 shows the difference. We concluded that the electron beam-charge asymmetry could be neglected in this analysis.

References

[1] B. A. Mecking *et al.* [CLAS Collaboration], "The CEBAF Large Acceptance Spectrometer (CLAS)," Nucl. Instrum. Meth. A **503**, 513 (2003).

[2] D. I. Sober *et al.*, "The bremsstrahlung tagged photon beam in Hall B at JLab," Nucl. Instrum. Meth. A **440**, 263 (2000).

[3] E. Pasyuk, "Energy loss corrections for charged particles in CLAS," CLAS Note 2007-016 (2007).

[4] Z. Akbar *et al.*, "g12 Analysis Procedures, Statistics and Systematics," CLAS Note 2017-002 (2017).

[5] C. Patrignani *et al.* [Particle Data Group], "Review of Particle Physics," Chin. Phys. C **40**, no. 10, 100001 (2016).

[6] M. Williams, C. A. Meyer, "Kinematic Fitting in CLAS," CLAS Note 2003-017 (2003).

[7] S. Stepanyan *et al.*, "Energy calibration of the JLab bremsstrahlung tagging system," Nucl. Instrum. Meth. A **572**, 654 (2007) [physics/0608302 [physics.ins-det]].

[8] M. Dugger, C. Hanretty, "Correction to the incident photon energy for g8b data," CLAS Note 2009-030 (2009).

[9] H. Olsen and L. C. Maximon, "Photon and Electron Polarization in High-Energy Bremsstrahlung and Pair Production with Screening," Phys. Rev. **114**, 887 (1959).

[10] Polarization of circularly polarized photon beam in g9b, `https://clasweb.jlab.org/rungroups/g9/wiki/index.php/Circular_Beam_Polarization`.

[11] W. Verkerke, D. Kirkby, "RooFit Users Manual v2.91," Document version 2.91-33, October 14th (2008).

[12] M. Williams, "Measurement of Differential Cross Sections and Spin Density Matrix Elements along with a Partial Wave Analysis for $\gamma p \to p\omega$ using CLAS at Jefferson Lab," Ph. D. thesis, Carnegie Mellon University (2007).

[13] T. D. Lee *et al.*, "Possible Detection of Parity Nonconservation in Hyperon Decay," Phys. Rev. **106**, 1367 (1957).

[14] R. Gatto, "Relations between the Hyperon Polarizations in Associated Production," Phys. Rev. **109**, no. 2, 610 (1958).

[15] W. Roberts and T. Oed, "Polarization observables for two-pion production off the nucleon," Phys. Rev. C **71**, 055201 (2005) [nucl-th/0410012].

[16] S. Strauch *et al.* [CLAS Collaboration], "Beam-helicity asymmetries in double-charged-pion photoproduction on the proton," Phys. Rev. Lett. **95**, 162003 (2005) [hep-ex/0508002].

[17] M. Williams, M. Bellis and C. A. Meyer, "Separating Signals from Non-Interfering Backgrounds using Probabilistic Event Weightings," arXiv:0804.3382 [physics.data-an].